UAB

Universitat Autònoma de Barcelona

Nanoscale interpretation of performances in organic solar cells and field effect transistors.

Ana Pérez Rodríguez

Tesi Doctoral

Departament de Física, Facultat de Ciències

Programa de Doctorat en Ciència de Materials

Universitat Autònoma de Barcelona

Supervisores: Dr. Esher barrena i Prof. Carmen Ocal

Tutora: Prof. Gemma Garcia

Departament of Nanostructured Materials for Optoelectronics and
Energy Harvesting

Institut de Ciència de Materials de Barcelona (ICMAB-CSIC)

Març 2018

Nanoscale interpretation of performances in organic solar cells and field effect transistors.

Ana Pérez Rodríguez

Departament de Física, Facultat de Ciències

Programa de Doctorat en Ciència de Materials

Universitat Autònoma de Barcelona

Esther Barrena   Carmen Ocal   Gemma Garcia
Directora   Directora   Tutora

Bellaterra, 13/03/2018

"It's a magical world, Hobbes, ol' buddy. . . let's go exploring!"

Bill Watterson

Abstract

Two of the main challenges in organic electronic devices are the semi-conducting layer morphology and the interface properties. Particularly, the interfaces formed by the semiconducting organic layer and the metallic electrodes strongly influences the performance of the devices. Thus, a strong effort has been devoted to improve these interfaces by different approaches such as self assembled monolayers (SAMs), layer of metalic oxides or contact doping. Concerning the morphology, it has been proven that it plays a fundamental role in exciton dissociation, charge collection and recombination in organic solar cells (OSC), as well as in the transport properties in organic field effect transistors (OFETs).

In this work we make use of atomic force microscopy (AFM) and, in a lesser extent, of other surface characterization techniques for the study of surfaces and interfaces that conform organic electronic devices. In particular, we focus on the use of friction force microscopy (FFM), conductive atomic force microscopy (C-AFM) and Kelvin probe force microscopy (KPFM) operating modes on OSC and OFETs devices with the goal of correlating the nanoscale characterization with the macroscopic performance of the devices.

This thesis is organized in the following way: the motivations of this work are presented in Chapter 1. In Chapter 2 a brief theoretical introduction on organic semiconductors and the concept of self assembly and nanostructuration is given, while in Chapter 3 the techniques

employed during this thesis as well as the used methodologies are described.

The results are presented in the Chapters 4, 5, 6 and 7. In Chapter 4 we study in detail the physical origin behind Transverse Shear Microscopy (TSM). By combining experimental data with simulations, we prove that the TSM signal has a dissipative origin and we use the technique to obtain the crystalline orientation of tip-induced grown PTCDI-C8 islands

In Chapter 5 we focus on the effect of hole transport layers (HTLs) for both organic and perovskites solar cells. For bulk-heterojunction solar cells (BHJ) we prove that the use of phosphonic acid self assembled monolayers (SAMs) changes the workfunction of the ITO cathode in a favourable way, but also induces a charge accumulation density at the interface with detrimental effects for the cell performance. In perovskite solar cells, despite using newly synthesized HTL with more favourable HOMO position, the energy level alignment at the interface with the TiO$_2$ results less favourable leading to worse photovoltaic device properties.

Chapter 6 is devoted to the solvent vapor annealing (SVA) effect on the crystallinity and vertical phase separation on oligothiophene bulk-heterojunction solar cells. We prove that, upon SVA, the oligomer domains present better crystallinity while the fullerene domains increase in size, enhancing the photovoltaic performance of the devices.

In Chapter 7, a nanoscale characterization by means of FFM was correlated with the device performance for C8-BTBT:PS OFETs, providing with a picture at the nanoscale of the organic films vertical phase separation. By means of KPFM, maps of the surface potential of the OFETs were obtained, allowing us to extract contact resistance and charge mobility values for different electrodes, concluding that the contact resistance is the critical factor limiting the devices performance.

Finally, in Chapter 8, the main conclusions of this thesis will be collected.

Resumen

Dos de los principales retos a superar en el campo de la electrónica orgánica son el control la morfología de la capa semiconductora y las propiedades de las interfases. En particular, las interfases formadas por la capa orgánica semiconductora y los electrodos metálicos influyen fuertemente en el comportamiento de los dispositivos. Hasta el momento se ha dedicado un gran esfuerzo a la mejora de estas interfases siguiendo para ello diferentes estrategias como son el uso de monocapas autoensambladas (self assembled monolayers, SAMs), capas de óxidos metálicos o mediante el dopaje de los contactos. Con respecto a la morfología, se ha probado que ésta juega un papel fundamental en la disociación de los excitones, en la extracción de la carga y en la recombinación en células solares orgánicas (organic solar cells, OSCs), así como en las propiedades de trasporte en transistores orgánicos de efecto campo (organic field-effect transistors, OFETs).

En este trabajo se utiliza principalmente el microscopio de fuerza atómica (atomic force microscope, AFM) y, en menor medida, otras técnicas de caracterización de superficies, y en la investigación de interfases que forman parte de dispositivos de electrónica orgánica. En particular, se ha empleado el microscopio de fricción atómica (friction force microscope, FFM), el microscopio de conducción de fuerza atómica (conductive atomic force microscope, C-AFM) y el microscopio de Kelvin de fuerza atómica (Kelvin probe force microscope, KPFM) en dispositivos OSC y OFETs, con el objetivo de correlacionar la caracterización a escala nanométrica con el rendimiento macroscópico de los dispositivos.

Este documento está organizado de la siguiente forma. Las motivaciones del trabajo se presentan en el Capítulo 1. En el Capítulo 2 se incluye una breve introducción teórica a los semiconductores orgánicos y a los conceptos de autoensamblado y nanoestructuración, mientras que las técnicas y metodologías empleadas en la tesis se describen en el Capítulo 3. Los resultados se presentan en los capítulos 4, 5, 6 y 7.

En el Capítulo 4 se detalla el fundamento físico del Transverse Shear Microscopy (TSM) que se emplea como técnica para obtener la orientación cristalina de islas de PTCDI-C8 crecidas por acción de la punta del microscopio. La combinación de datos experimentales con resultados de simulaciones numéricas nos ha permitido probar que la señal de TSM tiene naturaleza disipativa.

El Capítulo 5 se centra en el efecto de las capas transportadoras de huecos (HTLs) y su impacto en el rendimiento de células solares fabricados con materiales orgánicos y con perovskitas. Respecto a las células solares, hemos demostrado que el uso de SAMs de ácidos fosfónicos cambia favorablemente la función de trabajo del cátodo de ITO, pero también induce una acumulación de carga en la interfase con efectos negativos en el rendimiento del dispositivo. En las células solares de perovskitas, a pesar de utilizar un material recientemente sintetizado como HTL con una posición del HOMO más favorable, el alineamiento energético en la interfase con el TiO_2 resulta menos favorable, dando lugar a peores propiedades de las células solares.

El Capítulo 6 está dedicado al efecto del solvent vapor annealing (SVA) en la cristalinidad y la separación vertical de fase en células solares orgánicas de oligotiofenos. Hemos comprobado que, al aplicar el método SVA, los dominios del oligómero muestran mejor cristalinidad, mientras que los dominios del fullereno aumentan en tamaño, mejorando las propiedades fotovoltaicas de los dispositivos.

En el Capítulo 7 hemos realizado una caracterización a escala nanométrica de OFETs fabricados con C8-BTBT:PS mediante FFM de OFETs fabricados con C8-BTBT:PS, que ha permitido resolver la separación vertical de fase del PS y el C8-BTBT. Mediante KPFM, se obtuvieron mapas del potencial de superficie de los OFETs, a partir de los que se han obtenido valores de la resistencia de contacto y de la movilidad de carga para diferentes electrodos y concluyendo que la resistencia de contacto es un factor crítico que limita el rendimiento de estos dispositivos.

Las principales conclusiones de la tesis se incluyen en el Capítulo 8.

Contents

Motivation

Since the 1960s, the field of molecular electronics has drawn growing attention as an alternative to the traditional silicon-based devices. One of the main reasons for this development is the novel potential applications to a broad range of fields, such as medicine or biomedical research. Moreover, the lower manufacturing cost of organic-based electronic devices compared to inorganic-based devices, as well as the potential use of less resources and the capability of synthesizing the materials rather than mining them from earth, make the organic electronics field promising in terms of sustainability. Organic light-emiting diodes (OLEDs) have currently been commercialized, while organic photovoltaic cells (OPVs) and organic field effect transistors (OFETs) have already shown important advances and promising features.

However, there are still some challenges that must be overcome for achieving the high performances and become a strong alternative to Si-based technologies. One of the main obstacles concerns the optimization of the different interfaces in molecular electronic devices. These interfaces can be organic/electrode and organic/organic and strongly affect both the performance and lifetime of the devices. Therefore, a fundamental understanding of the mechanisms occurring at these interfaces is of fundamental importance for device optimization.

Particularly, in OPV, the interface between donor and acceptor material is critical for efficient charge separation, and determines the main cell parameters. Whereas there has been a major effort in designing and synthesizing novel donor and acceptor materials with tailored energy gap and molecular levels, the optimization of the donor/acceptor

structure and the interface properties between electrodes and the active layer are still a matter of trial-and-error and requires a deeper knowledge that guide the efforts. Similarly, in OFETs, the interface between the source/drain metal electrodes and the organic semiconductor plays a fundamental role in the charge carrier injection and extraction processes. In addition, the gate insulator/organic semiconductor interface importantly affects the formation of the accumulation channel. In spite large progress in the field, severe limiting factors of the performance and the stability of OFETs (contact resistance, hysteresis problems, threshold voltate shifts, low mobility values...) remain poorly understood at the nanoscale level.

The general goal of this thesis is the investigation of different interface-related problems in OPVs and OFETs at the nanoscale by employing advanced scanning probe microscopy techniques. This study allows us to correlate the structural and electrical properties at the nanoscale with the device macroscopic performance, and therefore to gain a deeper understanding of the mechanisms at the nanoscale that importantly affect the efficiency of the devices.

Specifically, for OPVs, two main issues are adressed for which AFM has been used individually or combined with X-ray diffraction methods:

- Role and effect of the hole transport layer (HTL) situated between the active layer and the electrode in organic and perovskite solar cells.

- Influence of the active layer morphology in bulk-heterojunction solar cells based on two isomers of a donor molecule upon solvent vapour annealing.

A large part of the thesis is further related with different questions related with OFETs. In OFETs, the crystalline quality of the organic layer determines the conductivity along the channel and therefore the carrier mobility. A systematic study is presented in order to gain

insight in the physical phenomena behind the use of Transverse Shear Microscopy (TSM) to map the orientation of crystalline domains in an organic film using as a case of example PTCDI-C8. By employing this and other SPM techniques, the following issues related to OFETs are addressed:

- Vertical phase separation in thin film OFETs consisting of a blend of an amorphous polymer and a organic semiconductor and its impact in the electrical performance of the device.

- Impact of the contact resistance in the charge transport for different electrodes.

- Study of the inter domain resistance and its dependence with the gate voltage.

- Charge trapping effecs and their impact in the current-voltage characteristics of the devices.

Introduction

2

Contents

2.1 Surface engineering: self assembly and nanostructuration.

Molecular self-assembly is the autonomous and spontaneous organization of molecular entities (building blocks) into patterns or structures [1]. In the context of organic materials, it refers to the phenomenon in which a system of organic molecules gets together forming an ordered aggregate either from solution or gas [2]. This aggregation occurs through interactions such as hydrogen bonds, van der Waals interacions, π-π bonds, etc [1, 3]. During this work, two different self assembly systems are studied: self assembled monolayers (SAMs), formed by the molecular chemisoption on the surface, and thin organic films, in which molecules physisorb on the surface.

Self assembled monolayers.   Self assembled monolayers (SAMs) are ordered molecular layers in which the molecules are chemically bonded to the surface through their head group [3, 4]. They are

very widely used, as they easily produce densely packed and oriented films just by immersion of the substrate in the molecular solution or from gas phase. The structure of a SAM is schematized in Figure 2.1, where the molecules are divided in three parts. The headgroup
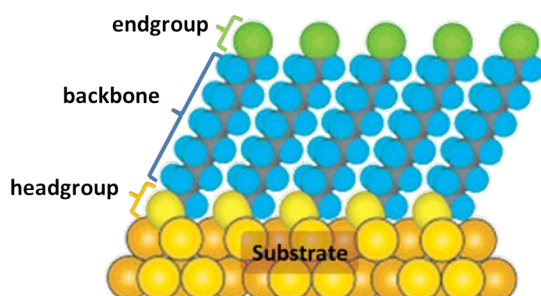
Fig. 2.1: Schematic of a SAM [5].

is the part interacting with the substrate. Bonding occurs through chemisorption and is essential to the formation process of the SAM. It plays a role in the strength of the interaction, therefore affecting the SAM stability and the ordering. The backbone acts as a physical barrier between the substrate and the external environment importantly affecting the optical and electrical properties. It also determines the monolayer thickness. The endgroup is the part of the molecule in contact with the external environment. It strongly influences the surface properties of the film; hydrophobicity, frictional properties, electrostatic potential, chemical reactivity. . .

Chapter 5 is devoted to the study of phosphonic acids self assembled monolayers on indium tin oxide (ITO) substrates.

Organic thin films   The organic thin films presented in this thesis are formed by small molecules acting as building blocks. These molecules present a wide range of applications such as organic light-emitting diodes (OLEDs) [6], organic field-effect transistors [7, 8], organic solar cells [9], sensors [10], etc. The most common preparation methods are solution or vapor phase processing. In this thesis, the thin film growth has been done by organic molecular beam evaporation

(OMBE) and bar-assisted meniscus shearing technique (BAMS). This will be detailed in Chapter 3. In the following section, the organic semiconductors theory will be introduced.

2.2 Organic semiconductors

Organic semiconductors are known from the beginning of the 20th [11, 12], but it wasn´t until the decade of the 70s, that the successful synthesis and doping of conjugated polymers made the first applications on organic electronics possible [13]. Moreover, the successful fabrication of an efficient photovoltaic organic solar cell [14] and of organic thin film transistors [15] focused the interest once again on the non-doped conjugated polymers and oligomers [16].

Organic semiconductors main components are carbon and hydrogen, and can consist additionally of oxygen, nitrogen, sulfur or fluorine. There are two major classes of organic semiconductors: **polymers** and **small molecules** (which are light-weight molecular materials). Both of them form conjugated systems, which are responsible for most of the optical and electronic properties. Conjugation is originated from the sp^2 hybridation of the carbon atoms of the rings, which is a result of the combination of the 2s and 2p orbitals. However, the sp^2 hybridization leaves the $2p_z$ orbitals pointing out of the plane of the sp^2. The overlap of p_z orbitals through π bonds leads to the π molecular orbitals formation, as can be seen in Figure 2.2 (a) exemplified in the benzene molecule (C_6H_6). The 2s, $2p_x$ and $2p_y$ orbitals lead to the formation of two σ bondings with the neighbouring C atoms, forming the molecular backbone. The formed π bonds are significantly weaker than the σ ones and are delocalized across all the aligned C atoms, supporting the charges mobility. Particularly, in benzene, the bonding π orbitals form the highest occupied molecular orbital (HOMO) and the antibonding π^* orbitals conform the lowest unoccupied molecular orbital (LUMO), as is schematized in Figure 2.2(b). The energy gap between the HOMO and LUMO levels is defined as the optical gap E_g
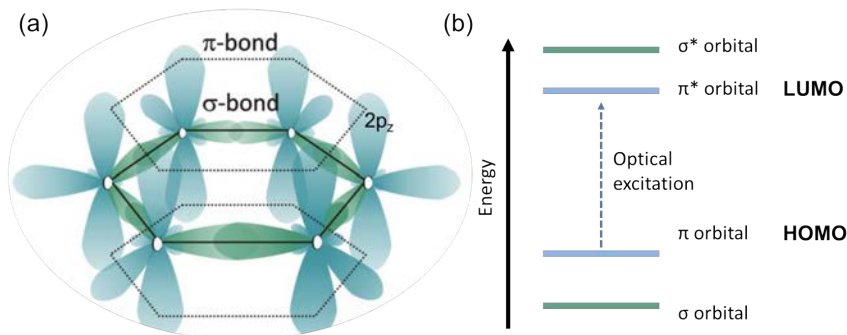
Fig. 2.2: Schematic of the sp^2 hybridization: (a) Formation of σ and π bonds in benzene and (b) energy level diagram of molecular orbitals in benzene [17].

and is typically between 1.5 and 3eV, allowing the light absorption and emission within the visible optical range. Therefore, for both polymers and small molecules, the electronics properties are determined by the π bonds.

One of the most important properties in organic semiconductors is the charge transport, which is described by the carrier mobility, and, in the most relevant types of organic devices, the device efficiency is directly related to it. The organic electronic devices are mostly divided in OLEDS, organic field-effect transistors (OFETs) and organic solar cells (OSCs). This thesis has been mainly focused in OFETs and OSCs, in which the carriers mobility has a different impact; while in OFETs high carrier mobility is essential for achieving high switching speeds, in OSCs, the mobility of both types of carriers must be balanced in order to guarantee charge separation and charge transport towards the electrodes. During the next section, the theory of OFETs and OSCs will be detailed.

2.3 Organic semiconductor devices

During this thesis, both organic solar cells and organic field effect transistors have been studied. In the next section, the working principles and theory of both types of devices will be detailed.

2.3.1 Organic solar cells

Organic solar cells (OSCs) based on organic semiconductors have been widely studied due to their potential for low-cost solar energy conversion [18]. Since Tang et al. introduced a donor-acceptor bilayer planar heterojunction in 1979 achieving an efficiency of 1% [14], conversion efficiencies have increased up to 13.2% , reported by Heliatek R&D in 2016 for a multi-junction cell. In the following, the working principles of organic solar cells will be briefly explained.

Working principles

Organic solar cells
In 1959, Jallman et al. introduced the first organic cell consisting of one layer of the organic semiconductor anthracene sandwiched between two metal electrodes [19]. In actual organic solar cells, the photactive layer consists of two semiconducting organic materials, one functioning as an electron donor (D) and another one acting as electron acceptor (A). This donor/acceptor heterojunction concept was developed in 1986 by Tang et al in the form of a bilayer of the two materials. In 1995, Yu et al. developed the bulk heterojunction cell, in which the two materials are intermixed as schematized in Figure 2.3(a) [20]. Upon absorption of light, an exited state is created in the donor material, which is formed by an electron and a hole culombically bound together [17]. This excited state is called **exciton** and the electric field needed for the separation into free charges is provided by the energy offset of the molecular orbitals of D and
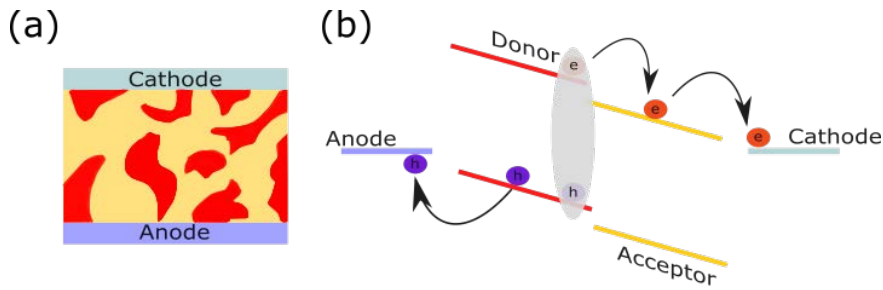
Fig. 2.3: Schematic cross section of a bulk heterojunction solar cell (a) and energy levels scheme illustrating the process of absorption, exciton generation and dissociation and charge diffusion towards the electrodes.

A. Therefore, the difference between the energy levels favours the transference of the electrons to the acceptor's LUMO and of the holes to the donor material´s HOMO. This transference takes place in the D/A interface. After the exciton dissociation into free charges, the charges are driven to the contacts, as is schematized in Figure 2.3(b) [21].

Solar cell parameters

Once the charges arrive to the electrodes, they are collected and a current I is measured. Figure 2.4 illustrates the current-voltage characteristics of a solar cell under illumination. The key parameters of solar cells are the efficiency η, the open circuit voltage V_{OC}, the sort circuit current I_{SC} and the fill factor FF. When there is no voltage applied in the cell we have the situation represented in Figure 2.4 (a), where the collected current comes from the built-in electric field resulting from the difference in the metals electrodes work function. Under this electric field, the separated carriers drift towards the electrodes: electrons move to the lower work function material and the holes to the opposite. The collected current is called I_{SC}, and it is defined as the current flowing through the solar cell in absence of external bias. If a external bias is applied and swept to positive values, we get to the open circuit conditions in Figure 2.4 (b), also known as
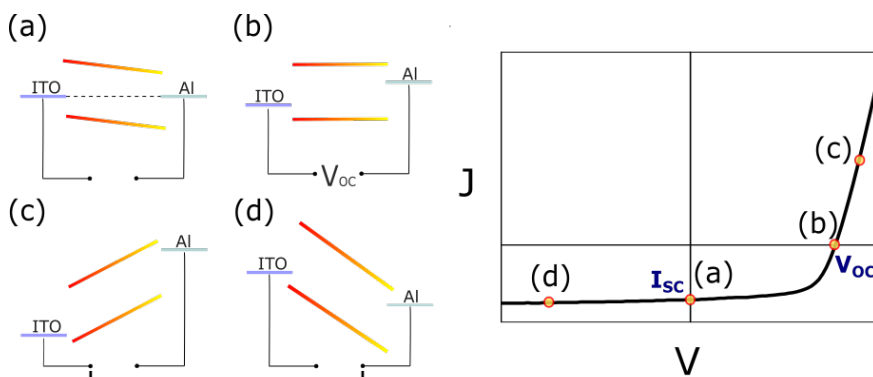
Fig. 2.4: Schematic picture of organic diode device function (left) and current-voltage characteristics of a solar cell (right) in which the following situations are marked: (a) closed circuit condition, (b) flat band or open circuit condition, (c) forward bias larger than V_{OC} and (d) reversed bias.

"flat band condition". This bias is defined as the voltage at which no current flows through the solar cell under illumination: as there is no driving force, the current is zero. In this situation, V_{OC} corresponds to the difference between the metals work function and compensates the built-in field. V_{OC} is determined too by the energy values of the acceptor LUMO and the donor HOMO as well [22]. If the bias is increased to more positive values, the device reaches the situation in Figure 2.4(c) where contacts efficiently inject charges into the device. If they radiatively recombine, the device acts as a LED. If a reverse bias is applied, as shown in Figure 2.4(d), the photogenerated carriers drift under strong electric fields and the device acts as a photodetector. Another important cell parameters are the fill factor and the power conversion efficiency. The fill factor FF gives information about the curve shape, as it is the relation between the maximum generated power and the product of V_{OC} and I_{SC}:

$$FF = \frac{P_{max}}{V_{OC}I_{SC}} \tag{2.1}$$

The power conversion efficiency is the ratio between the maximum power P_{max} and the input light power P_L, as shown in the following equation:

$$\eta = \frac{P_{max}}{P_L} = \frac{V_{OC}I_{SC}}{P_L}FF \tag{2.2}$$

As can be seen in equation 2.2, for achieving a maximum eficiency in solar cells, V_{OC}, I_{SC} and the fill factor must be optimized. Typically, and from now on in this thesis, instead of the current I, the current density per area unit (J) is used.

Contact engineering in organic solar cells

Bulk heterojunction organic solar cells efficiency has been increasing in the last years reaching up to 13.2%. These improvements are related to an enhance of the processing conditions [23, 24] and the use of novel acceptor[25, 26], donor[27, 28] and interface materials at both electrodes [29]. One of main functions of the interface materials is adjusting the energy barrier height between the active layer and the electrodes, as an ideal interface would present good Ohmic contacts with low resistance. Moreover, the material should be able to select between charges, in order to prevent carriers from reaching undesired electrodes. It should as well show a good stability, avoiding chemical or physical reaction between the active layer and the electrode, such as oxidation. As a result, the selected interface plays an essential role determining the polarity of the device [29, 30]. During this thesis, we will focus on the role of the interface materials for energy level modification. In the following, the basis of the energy level alignment at the organic/electrode interface will be explained.

Integer Charge Transfer Model
In order to describe the energy levels behaviour at the interface between an organic semiconductor and a metallic electrode, the Integer Charge-Transfer (ICT) model must be introduced [31]. E_{ICT+} and E_{ICT-} are defined as the energy required to take away one electron from the last occupied molecule/polymer orbital producing a fully relaxed state and the energy gained when one electron is added in the first vacant state producing a fully relaxed state, respectively. Unlike the HOMO and LUMO, these energies are the relevant ones in order to determine the energy-level alignment at this type of interfaces,

due to existence of self-localized states for π-conjugated molecules. Moreover, the Coulombian effect of electron-electron repulsion is responsible from shifting these integer charge-transfer states away from the HOMO and LUMO.

Taking into account this energy level picture, the different situations of energy level alignment at the electrode/organic can be described. All the situations are represented in Figure 2.5:

(a) $\Phi_{SUB} > E_{ICT+}$: the workfunction of the substrate is larger than the energy of E_{ICT+}. When the organic material is in contact with the substrate, electrons will flow from the E_{ICT+} to the substrate. This charge transfer will make the interface molecules become positive charged and therefore the substrate negatively charged, creating a dipole at the interface that shifts the vacuum level until the system reaches equilibrium $\Phi_{ORG/SUB} = E_{ICT+}$. This results in a pinning of the metal Fermi level to the E_{ICT+} of the semiconductor and to an interfacial dipole Δ which is the difference between the substrate work function and the E_{ICT+} energy.

(b) $E_{ICT-} < \Phi_{SUB} < E_{ICT+}$: the workfunction of the substrate is larger than E_{ICT-} but smaller than E_{ICT+}. When the two materials are brought in contact, electrons will not flow neither from the semiconductor to the substrate nor vice versa, as the energy cost is too big to cause a spontaneous electron transfer across the organic/substrate interface. Therefore, in equilibrium, the vacuum levels align and there is no offset.

(c) $\Phi_{SUB} < E_{ICT-}$: the substrate workfunction is smaller than the E_{ICT-} energy. When both materials are brought in contact, electrons will flow from the substrate to the organic material. Upon this flow, the organic molecules at the interface become negatively charged and the substrate becomes positively charged until the equilibrium is reached leading of a pinning between

the metal Fermi level and the E_{ICT-} energy level. As a result, an interfacial dipole Δ is formed, which is the difference between the substrate work function and the E_{ICT-} energy.
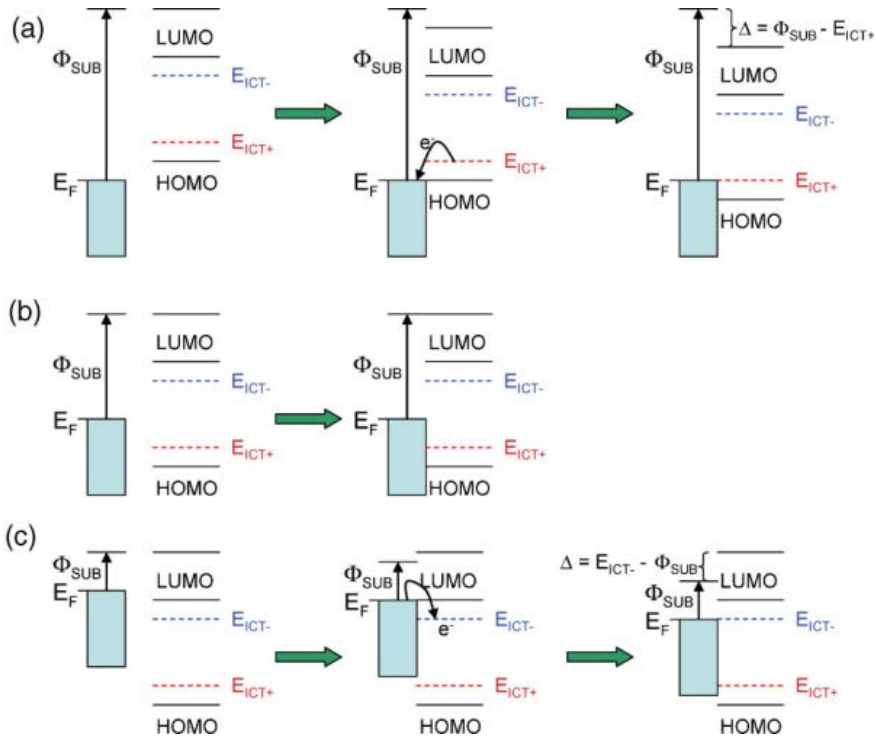

Fig. 2.5: Schematic illustration of the possible situations when a metallic substrate and an organic semiconductor get in touch according to the ICT model and their evolution. In (a) the workfunction of the substrate is larger than the energy of E_{ICT+} resulting in a pinning of the metal Fermi level to the E_{ICT+} of the semiconductor and to an interfacial dipole Δ. In (b) the workfunction of the substrate is larger than E_{ICT-} but smaller than E_{ICT+} and the vacuum levels align. In (c) the substrate workfunction is smaller than the E_{ICT-} energy, resulting in a pinning between the metal Fermi level and the E_{ICT-} energy level, leading to the formation of an interfacial dipole Δ. Image adapted from ref [31].

The ICT model is valid for weak molecule-substrate interaction. The energy level at the organic/electrode interface is of fundamental importance in order to optimize the device performance. The two energetic situations at the electrodes would be the ones depicted in Figure 2.5 (a) and (c). In order to achieve that, different strategies

have been developed for the interfacial layers at both electrodes, which will be adress in the following.

Interfacial materials for organic solar cells

During this thesis, only conventional (non inverted) organic solar cells have been studied. Within this frame, it is necessary to differentiate the interlayers placed at the cathode (typically metals Al or Ag) and the ones placed at the anode (typically ITO or FTO). For the electron-transporting materials situated in the cathode, the most widely used materials have been binary metal oxides, such as ZnO, TiO_x, Nb_2O_5 or SnO_x, and recently developed ternary oxides, such as Al doped ZnO, Mg-doped ZnO and Cs-doped metal oxides [29, 32]. In the recent years, also polymers and small molecules [33], low work function metals [34], metal salts [35, 36], carbon-based materials [37, 38] and hybrid composites [39] have been employed.

In Chapter 5 we have focused in the hole transporting layer (HTL) situated in the anode. The main requirement is to have high work functions to match the HOMO level of the donor materials in order to facilitate hole-extraction. To the date, the most commonly used HTL is the conductive polymer poly(3,4-ethylenedioxythiophene) polystyrene sulfonate (PEDOT:PSS), whose work function ($\approx$5.1eV) matches well most of the donor polymers allowing to form good ohmic contact. Some other conductive polymers as poly[(4,4-bis(3-(2-ethyl-hexyl)dithieno [3,2-b:3-d] silole)-2,6-diyl- alt-(2,5-(3-(2-ethylhexyl) thiophen-2-yl) thiazolo [5,4-d]thiazole)] (PSEHTT):ICBA or solution processable polyaniline based polymers have been used [40]. Graphene oxides have been also employed as efficient hole transporting materials at a low cost and easy processability [37]. During this thesis we have focused on the use of self assembled monolayers as ITO modificators, with the aim of increasing its work function and enhancing the energy level matching at its interface.

As detailed in the previous section, SAMs have been proven to be effective interfacial modifiers modulating the surface properties of ITO,

such as work function, surface energy, and electron-transfer kinetics that might lead to an enhancement in the efficiency and/or operational range of organic electronic devices. The advantages over other electrode treatments are that the deposition, traditionally through immersion in a solution of the modifiers, is simple, and the diversity of tail terminal groups offers the possibility of choosing the functionalities needed for a given surface or application [41]. Phosphonic acid, silanes and amines have been widely used to tune the surface properties in both multilayer and bulk heterojunction OSCs and OLEDS [38, 42–46]. The use of dipolar SAMs to modify the work function of the ITO is a generally used strategy [46–49] to improve the OSC performance via an increase in the open-circuit voltage (V_{OC}). Chapter 5 will be devoted to the effect of ITO functionalization by means of Phosphonic acid SAMs on the performance of the OSC devices.

2.3.2 Organic field effect transistors

Integrated circuits basic units are the so−called field effect transistors (FETs). During this section, the basic working principles of organic film effect transistors (OFETs) will be introduced. In particular, the importance of the organic film morphology and contacts will be addressed

Working principles

The basic scheme of a OFET can be observed in Figure 2.6. OFETs have three electrodes known as gate, source and drain. The distance between the source and drain electrodes is called the *channel length* L while their lateral dimension is called *channel width* W. The gate electrode and the semiconductor thin film form a parallel plate capacitor, with the gate dielectric acting as the insulator material between them.
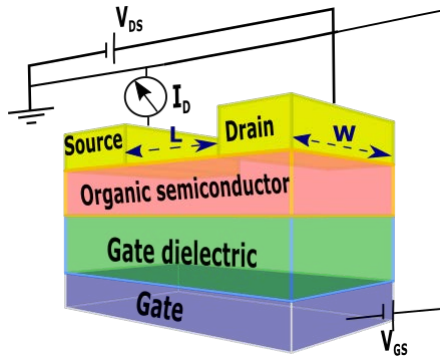
Fig. 2.6: Schematic 3D cross section of a top-contact, bottom-gate OFET.
,

Voltage is usually applied to the gate (V_G) and drain (V_D) electrodes, while the source electrode (V_S) is normally grounded. The applied voltage between source and gate electrodes is referred as (V_{GS}), while the potential between source and drain is referred as (V_{SD}). The source is the electron or hole injection source when either a positive or negative V_{GS} gate voltage is applied, respectively. The basic operating regimes are schematized in Figure 2.7. By applying
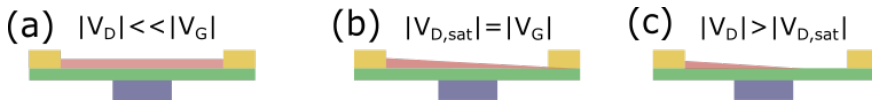

Fig. 2.7: Illustrations of the operating regimes of an ideal field-effect transistor for (a) linear regime, (b) start of the saturation regime and (c) saturation regime.

V_{GS}, an electric field is created, charging the capacitor. This results in an accumulation channel (pink in the scheme) formed by charges injected from the source electrode. For positive V_{GS} values, electrons will be accumulated, while for positive V_{GS} values, the accumulation channel will be formed by holes. The number of accumulated charges is directly related to V_{GS} and to the capacitance value of the dielectric (C_i). Under an applied V_{SD}, these charges are extracted through the drain, where the current I_{SD} is measured.

When no source-drain bias is applied the charge carrier concentration along the channel is uniform. When a small V_{SD} is applied (Figure

2.7 (a)), the accumulation channel forms a linear gradient between source along the channel length L. This working regime is called *linear* regime, and the drain current follows Ohm's law. When the V_{SD} bias is further increased it reaches the value $V_{SD}=V_{GS}$, at which the channel is "pinched off" as can be observed in Figure 2.7 (b). This implies that a depletion region is formed near to the drain electrode due to the rapid extraction of the charges. This marks the starting point of the *saturation* regime. A space-charge limited saturation current $I_{SD,sat}$ can flow across this narrow depletion zone. If the V_{SD} is further increased (Figure 2.7 (c)), the current will not change, as it leads to a spatial extension of the depletion region shortening the channel. The OFET keeps working under the saturation regime.

Current-voltage characteristics

In the first place, some definitions related to the OFETs functioning must be explained:

- **Field-effect mobility (μ):** Is the charge carrier mobility, which describes the ability to transport the electronic charge, found in a transistor. It can be extracted from the current-voltage characteristics either in saturation or linear regime.

- **Threshold voltage:** Upon an applied V_{GS} bias, not all the injected charges are mobile and will contribute to the OFET current, but will also be accumulated in traps. Because of these traps, an offset in the gate voltage appears and must be overcome in order to start forming the channel. This voltage is called threshold voltage bias (V_{TH}), being the effective gate voltage V_{GS}-V_{TH}. These traps are due to the presence of fixed charges in the dielectric, in the interface between the semiconductor and the dielectric, and defects in the semiconductor [8, 50].

- **On/off current ratio**: Ratio between the drain current, measured in the transfer curve, in the on-state and in the off-state.

- **Contact resistance**: The resistance at the source and drain contacts, known as *contact resistance*, limits the current flowing through the device. As part of this thesis has been devoted to enhance the contacts, this will be addressed in detail later.

As explained above, the outcome of the device is the electric current flowing between source and drain (I_{SD}). The drain current in the linear and saturation regimes can be quantified by taking into account the following assumptions:

1. Gradual channel approximation: it assumes that the variation of the electric field along the channel (along L) is much smaller than perpendicular to the channel

2. The mobility μ is constant within the channel.

With these assumptions, the following expressions can be deduced [50, 51]:

$$I_{D,linear} = \frac{\mu \cdot C_i \cdot W}{L} \left[(V_{GS} - V_{TH}) \cdot V_{SD} - \frac{1}{2} V_{SD}^2 \right]$$

$$\text{for} \quad |V_{GS} - V_{TH}| > |V_{SD}| \tag{2.3}$$

$$I_{D,saturation} = \frac{\mu \cdot C_i \cdot W}{L} (V_{GS} - V_{TH})^2$$

$$\text{for} \quad |V_{SD}| > |V_{GS} - V_{TH}| > 0 \tag{2.4}$$

We can measure two different current-voltage characteristics:

Output characteristic

The drain current is plotted over a range of V_{SD} values while V_{GS} is kept constant. These curves provide mainly qualitative information

about the device, rather than quantitative. However, the charge carrier mobility can be extracted using the V_{TH} obtained from the transfer curves. An example is shown in Figure 2.8 (a).

Transfer characteristic
The drain current is collected over a range of V_{GS} values, while V_{SD} is kept constant. An example can be observed in Figure 2.8 (b).
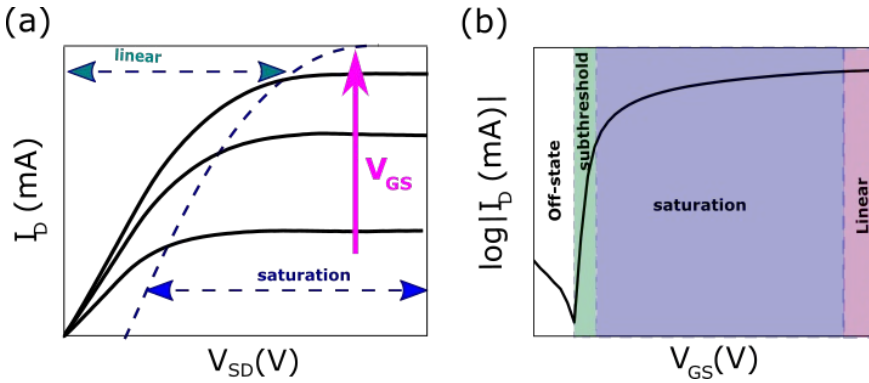

Fig. 2.8: Illustrations of the operating regimes on (a) output and (b) transfer current-voltage characteristics.

They are generally plotted in logarithmic scale and they allow to determine the on/off current ratio, the charge carriers mobility and the threshold voltage of the transistors. V_{TH} is estimated, as depicted in Figure 2.9, by the linear extrapolation of the drain current at its maximum slope point to the intersection with the V_{GS}.

Mobility determination

From the slope of the linear extrapolation depicted in Figure 2.9, the mobility in both saturation and linear regimes can be extracted:

$$\mu_{sat} = \frac{2L}{WC_i}\left(\frac{\partial\sqrt{|I_{SD}|}}{\partial V_{GS}}\right)^2 \text{ for for } |V_{SD}| > |V_{GS} - V_{TH}| \qquad (2.5)$$
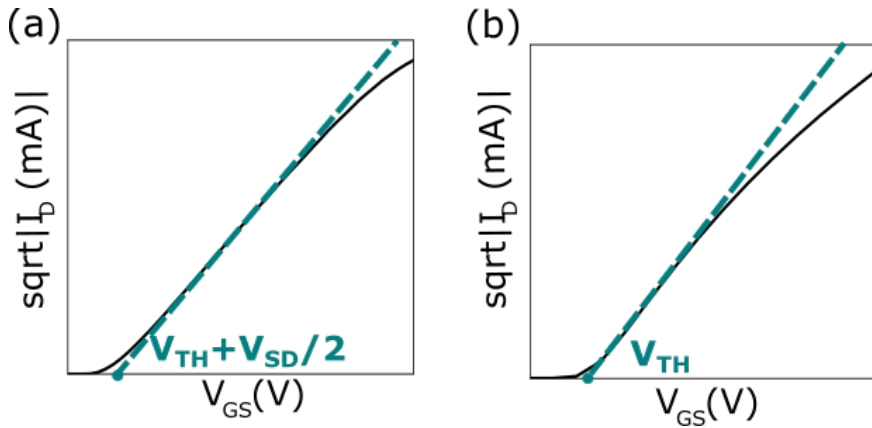
Fig. 2.9: Extrapolation method in the linear (a) and saturation (b) regime.

$$\mu_{linear} = \frac{L}{W C_i V_{SD}} \frac{\partial I_D}{\partial V_{GS}} \text{ for } |V_{GS} - V_{TH}| > |V_{SD}| \tag{2.6}$$
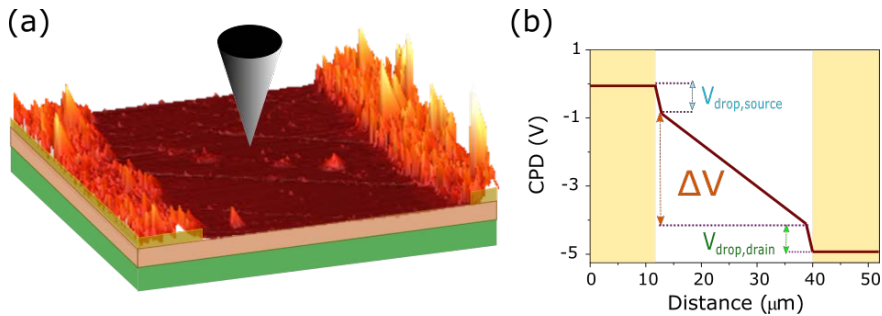

Fig. 2.10: Working scheme of a KPFM measurement on a OFET (a) and modelled potential profiles in linear regime with V_{SD}=-5V. The contacts are marked in yellow in the profile.

However, during this thesis, potential profiles obtained with KPFM like the one shown in Figure 2.10 (b) have been used to calculate the intrinsic field-effect mobility in the channel by excluding the contact resistance at the electrodes. This can be done by measuring the potential drop at the contact (V_{drop}), marked in Figure 2.10 (b). Therefore, based on equation 2.3, and neglecting the $\frac{1}{2}V_{SD}^2$ term for $|V_{GS} - V_{TH}| > |V_{SD}|$, the mobility can be extracted [50, 52]. In the case of the linear regime (for $V_{SD} \ll V_{GS}$), as the drain current is

directly proportional to V_{GS}, the mobility can be obtained with the variation of I_D respect to V_{GS} at a constant V_{SD}:

$$\mu_{linear,channel} = [\frac{I_D \cdot L}{W \cdot C_i}]\frac{1}{\Delta V \cdot (V_{GS} - V_{TH})} \qquad (2.7)$$

Where $\Delta V = V_{SD} - V_{drop,source} - V_{drop,drain}$. During this thesis, the KPFM technique, which will be explained in detail in Chapter 3, has been employed to evaluate the surface potential in working OFETs during the different working regimes [53–56]. The KPFM technique provides an insight into the OFETs functioning with a very high spatial resolution and allows us to plot the potential profiles along the channel of working and OFETs and extract V_{drop} at the source and drain electrodes as shown in Figure 2.10.

Contact resistance

While Si MOSFETs often show contact resistances of 0.1 Ωcm, OFETs tend to have contact resistances over to 100Ωcm, [56] which implies that the device performance is significantly limited by the charge injection at the electrodes. Due to the R_C, the estimated μ can be considerably smaller than the intrinsic mobility of the film ($\mu_{channel}$).

The energy level alignment between a metal and an organic semiconductor was described above. In case of vacuum-level alignment, the contact resistance R_C arises from the difference between the workfunctions of the metal and the E_{ICT+} or E_{ICT-} states of the organic semiconductor. However, if the interface between the two materials has a large number of surface states, Fermi level pinning can take place making the workfunction similar for both materials, and interfacial dipoles or the traps in the interface would contribute to R_C. Different methods are employed in order to extract the R_C values. the most common are the Y-function and transfer-length methods, both using the transfer characteristics [57]. However, other strategies as the

gated four point probe measurement, which employs two additional terminals that detect the local potential in the channel, as well as KPFM (Kelvin Probe Force Microscope) have been employed. During this thesis, we have used the potential maps obtained by KPFM to evaluate the contact resistance of the electrodes in bottom-gate top-electrode OFETs [53, 55]. In order to do that, the potential drop at an electrode is extracted from the surface potential images, as is shown in Figure 2.10 (b), and introduced in the following expression[54]:

$$R_C(\Omega \cdot cm) = W \cdot \frac{V_{drop}}{I_{SD}} \qquad (2.8)$$

Both contact resistances ($R_{C,source}$ and $R_{C,drain}$) can be calculated contributing to the contact resistance as $R_C = R_{C,source} + R_{C,drain}$. Excluding the contact resistance, the channel resistance can be estimated from the total device resistance using the following expression [54]:

$$R_{channel} = \frac{V_{SD}}{I_{SD}} - R_C \qquad (2.9)$$

2.3.3 Perovskites for solar cells

Perovskites are materials described by the formula ABX, where X is an anion and A and B are cations of different sizes (A being larger than B). The crystal structure of perovskites is shown in Figure 2.11. Mitzi
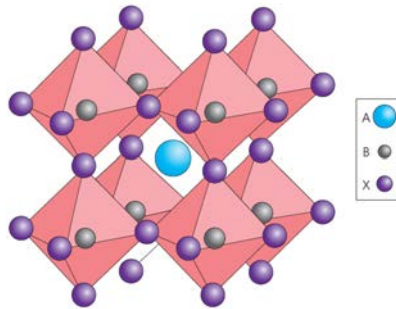

Fig. 2.11: Perovskite crystal structure.

and coworkers focused in the 1990s their research on the optoelec-

tronic properties of organicinorganic perovskites, more specifically on layered organometal perovskites [58]. Organic–inorganic halide perovskites solar cells have become a promising technology due to different attributes: strong solar absorption, low non-radiative carrier recombination rates, easy processability, long exciton diffusion lengths and high carrier mobility among others [59, 60]. Although the most efficient cells nowadays contain lead, which increases the toxicity during device fabrication, their fast development compared to OSCs or Dye Solar Cells has set perovskites solar cells in the lead of the new photovoltaic technology.

As a part of this thesis we have studied organic hole transport materials (HTM) used in solar cells with CsFAMAPbIBr as active layer. Devices fabricated with CsFAMAPbIBr have reached efficiencies up to 15.7% [61]. The role of these HTM layers will be explained in detail in Section 5.2.

Materials, instrumentation and sample preparation

3

Contents

3.1 Preparation of substrates and self-assembled monolayers

During this thesis, different substrates have been employed. The cleaning and preparation of these substrates is described in 3.1.1. As a main goal of this thesis is the surface treatment of electrodes employed in organic electronics, in section 3.1.2, the techniques for surface modification will be detailed.

3.1.1 Substrate preparation

The organic semiconductors films used in OFETs were prepared and characterized on SiO_2 or Al_2O_3 substrates. The thin films for characterization were grown in heavily p or n-doped silicon with a thin $\sim 2-3$nm native oxide layer, while the OFETs were prepared using commercial Si substrates with 200 nm of SiO_2. For this dielectric, the theoretical capacitance is of $17.3 \times 10^{-9} F \cdot cm^{-2}$.

Both types substrates were prepared in a similar way, by successive sonication cycles in acetone and ethanol of 15 minutes each. For films prepared by OMBD, the substrates were additionally annealed at a temperature of $\sim 300°C$ in ultra high vacuum (UHV) in order to desorb organic contaminants on the surface.

For the experiments in Chapter 5, indium tin oxide (ITO) substrates were prepared also by the successive sonication cycles explained above. Additionally, oxygen plasma cleaning was employed to clean and form activated oxygen species at the ITO surface afterwards [62].

3.1.2 SAMs and micro contact printing

Two phosphonic acids have been used: $3,3,4,4,5,5,$ $6,6,7,7,8,8,8-$ tridecafluoro octylphosphonic acid (FOPA) and 4-cyanophenyl phosphonic acid (CPPA), from Sigma Aldrich. The SAMs have been prepared by immersion in solutions in ethanol in the milimolar range. In order to obtain homogeneous solutions, additional heating (with temperatures below $80°C$) or sonication were employed.

SAMs were prepared either by dip coating (in order to obtain fully formed monolayers) or micro contact printing (μCP), which is a lithography technique that employs a stamp of polydimethylsiloxane (PDMS) [63, 64] to transfer the molecules to the surface forming an specific pattern in the range of μm [65]. The dip coating standard

procedure consisted on immersing the clean substrate right after the plasma treatment in a $1mM$ solution of the selected phosphonic acids during night. Afterwards, the samples were rinsed in pure ethanol and annealed in a hotplate at $130°$C for 1h [66]. The patterned samples were prepared by previously cleaning the ITO substrates by the standard procedure already described. Then, the stamp is inked by immersion in the molecular solution during 5 minutes, dried under nitrogen flow and placed on the clean substrate during 5 minutes. During this time, the molecules are transferred to the substrate, forming self assembled monolayers in the pattern presented by the stamp. After the transfer, the stamp is removed and the sample is placed in a hotplate for an annealing at $130°$C for 10 minutes. Then, the surface is rinsed with ethanol in order to remove the excess material. For the KPFM measurements described in (Chapter 5), a pattern of FOPA was first produced on the ITO surface by microcontact printing and then the sample was reimmersed in a second molecular solution of CPPA. Therefore, a patterned surface with two differenciated SAMs is obtained.

3.2 Thin film growth and device fabrication

3.2.1 Organic solar cells

Organic solar cells were fabricated following the following process:

1. **Anode**: Bare ITO substrates (patterned, commercially available) and SAM-modified ITO substrates were prepared as described in Section 3.1, and used as anodes in the BHJ solar cells. The reference devices were fabricated with commercially available poly (3,4-ethylenedioxythiophene):poly- (styrenesulfonate), PEDOT:PSS as interlayer between the bare ITO substrates and the active layer. The PEDOT:PSS layer was prepared by **spin**

coating of a 1:1 PEDOT:PSS water solution. Spin coating is a thin film fabrication technique in which an small amount of the coating material is placed in the centre of the substrate. Then, the substrate is spinned at high speed, leading to the spreading of the coating material by centrifugal force [67]. By tunning the angular speed, the applied solvent (which typically evaporates during the coating), and the solutions viscosity and concentration, the thin film thickness can be controlled. For PEDOT:PSS, the spin coating process was initiated with 3 seconds at 300rpm followed by 2 seconds at 4000rpm and a posterior annealing at 130°C for 10 minutes, leading to a 200nm film.

2. **Active layer preparation**: The active layer was formed by spin coating of a mixed solution of PBDTTT-CF and PC$_{71}$BM in chlorobenzene with 1:1.5 ratio (10 mg ml^{-1}:15 mg ml^{-1}) in two steps: first 120s at 200rpm, with a 500rpms^{-1} acceleration, with the goal of homogeneously spreading the coating. Then during 60 seconds, the angle speed was maintained at 4000rpm. Afterwards, the samples were annealed at 60°C for 10 minutes. 1,8-Diiodoctane was added to the mixed solution (3 % volume) in order to improve the film cristallinity [68].

3. **Cathode**: A 0.7 nm thick lithium fluoride (LiF) film was used as electron selective interlayer. LiF has been proved to enhance the efficiency of OSC and OLEDs by lowering the series resistance of the device by a factor of 3 or 4 [69, 70]. Both LiF and the 200nm thick cathode Al layer were thermally evaporated in vacuum over a mask (matching the ITO pattern) to define the cathode and anode terminals in the cell.

A picture of the final device, consisting on four different cells and a scheme of the device are shown in Figure 3.1.
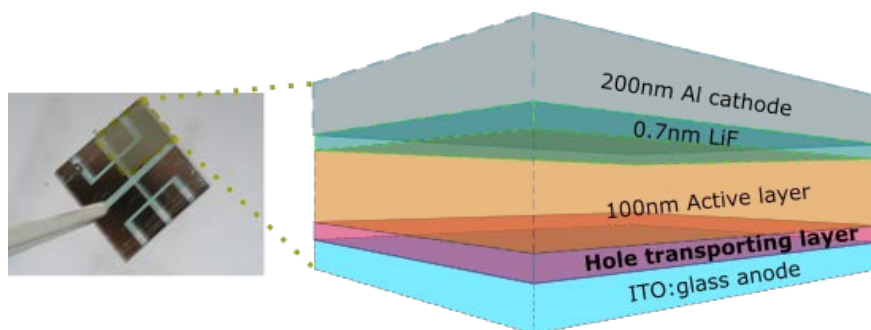
Fig. 3.1: Solar cell scheme and picture of the final device.

All the devices were fabricated during two different stays in the Licht-technisches Institut (KIT), located in Karlsruhe (Germany), in collaboration with Prof. Dr. Uli Lemmer's group.

3.2.2 OFETs

OFETs semiconducting layers were prepared by two different techniques: **Organic Molecular Beam Deposition** and **BAMs**.

Organic Molecular Beam Deposition

Organic Molecular Beam Deposition (OMBD) is a widely used technique for the deposition of low-molecular-weight organic molecules. During this thesis it has been used for preparing thin films with the studied small molecules. For the film formation, the material (typically in powder) is located in vacuum (10^{-6}-10^{-8} mbar) and heated until the temperature exceeds the sublimation temperature, moment at which the material evaporates and condenses on the cooler substrate surface. This leads to well ordered films formed in clean substrates with a perfect control of their thickness, growth rate and substrate temperature [71]. The equipment employed in this thesis was a home

made UHV chamber in which a quartz crystal micro balance (QCM) positioned close to the substrate was used to accurately control the film thickness, achieving sub monolayer coverages. Films were grown onto SiO_2/Si substrates with different oxide thicknesses treated as explained in Section 3.1.1.

BAMs

The solution processed OFETs were prepared by the so called bar-assisted meniscus shearing method (BAMS), developed by Del Pozo et al [72], and in collaboration with Inés Temiño and Marta Mas-Torrent.
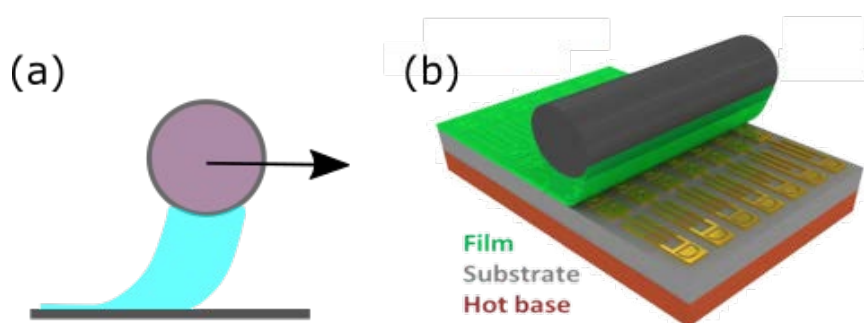

Fig. 3.2: (a)Illustration of how the bar is moved and the film is formed and (b)3D representation of the process [72].

A smooth cylindrical bar is placed 300μm above the clean SiO_2 substrates, which are maintained at 105°C. 20μL of the cosolution is placed between the bar and the substrate and, immediately after, the bar is moved at a speed of ≈ 1 cms^{-1} displacing the meniscus (Figure 3.2). Upon this displacement, the film if formed by convective self-assembly [73], leading to highly crystalline thin films.

Electrodes

All the devices were fabricated in top-contact bottom-gate configuration, as schematized in Figure 2.6. Source and drain Au electrodes were deposited on the organic thin films through a shadow mask from Ossila at a pressure below 10^{-6} mbar. The film thickness, of $\approx$ 50nm was monitored by a quartz crystal microbalance.

3.3 Instrumentation

3.3.1 Atomic force microscopy

The family of scanning probe microscopies (SPM) main characteristic is the use of a physical nanometric sized probe to measure the surface properties of materials, frequently mapping the surface. The feedback signal used for the probe is a certain interaction between probe and sample.

Working principles

In atomic force microscopy, developed by Binning, Quate and Gerber in 1986 [74], a force sensor called cantilever is used to measure the interaction forces acting between the probe and the surface. These forces cause the bending and torsion of the cantilever, which are sensed by an optical beam detection method (schematized in Figure 3.3).
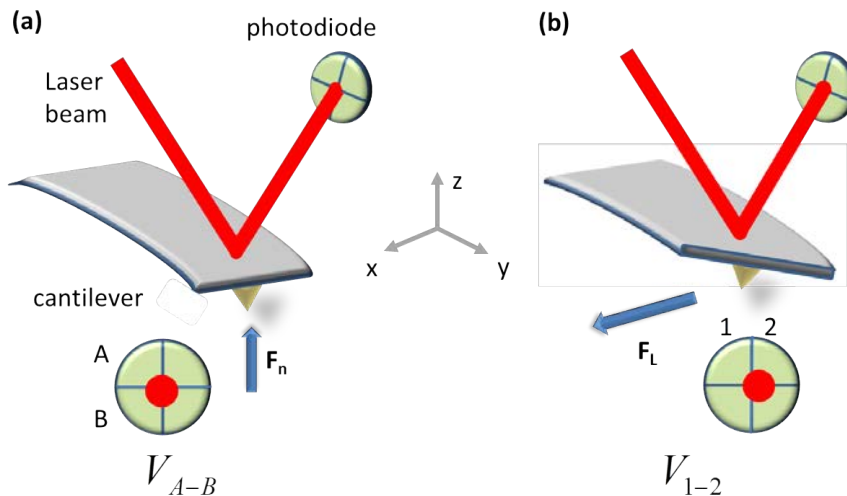
Fig. 3.3: Schematics of the optical detection method employed to sense the bending and torsion of the cantilever due to normal (a) and lateral (b) forces, respectively. Image courtesy of Luis Garzón.

This method consists on a laser beam focused on the back side of the cantilever and reflected into a 4 segmented position-sensitive photodiode. Segmenting the photodiode allows the detection of the deflection in two orthogonal directions, therefore enabling the separation and quantification of the bending and the torsion of the cantilever. When the tip experiences a force, the lever es deflected and the reflected spot on the photodiode is deviated: in the case of a normal force, the vertical deflection moves the spot up and down between the upper and lower halves of the photodiode (Figure 3.3(a)), while for a lateral force the torsion of the cantilever moves the spot between the right and left halves of the photodiode (Figure 3.3(b)). Therefore, the normal force is proportional to the signal difference V_{A-B} and the lateral force to the signal difference V_{1-2}.

The force sensor in AFM is a nanometre-sized tip attached to one of the cantilever ends. Typically, cantilevers are fabricated from silicon (Si) or silicon nitride (Si_3N_4) in triangular or rectangular geometries. Cantilever spring constants are in the range of 0.1 to 50 Nm^{-1} and the tip radius is about 2-100nm. Veeco Si tips with a spring constant

of 0.01-0.2 Nm^{-1} have been used for the contact mode experiments while Budgetsensors tips with a spring constant of 2.8 and 20 Nm^{-1} have been used for dynamic experiments. For conducting and electrostatic measurements, either B-doped diamond, Pt/Cr or Pt/Ir coated tips mounted on different spring constant cantilever have been used.

The forces acting between the probe and the sample have different origins and contributions and are explained in detailed in references [75, 76]. However, in the following, the main tip-sample interactions will be introduced.

Van der Vaals forces.   Relatively weak attractive forces that act on neutral atoms and molecules and that arise because of the electric polarization induced in each of the particles by the presence of other particles. When an atom with a finite dipole approaches another atom, its generated electric field will polarize the nearby atom. As a consequence, an attractive interaction between these two atoms will appear in the range between $\approx$ 0.2 and 10 nm [75].

Short range forces.   These forces are caused by the wave functions overlapping and the repulsion of the ion cores. They can be either attractive or repulsive and act in the range of $\approx$ 0.2Å-1nm.

Friction forces.   When the tip is sliding through the sample, it experiences a frictional force in the direction opposite to the movement. In the SPM setup, friction leads to the torsion of the cantilever as shown in Figure 3.3(b), so the dissipation energy can be imaged, providing sometimes with more information than the topographic images [77]. As Friction Force Microscopy (FFM) has been an essential tool during this thesis, as well as an object of study itself, its principles will be explained in detail in Section 3.3.1.

Electrostatic forces.   These forces obey Coulombs's law and act in a long range. Considering the tip-sample distance as a capacitor, V_{bias}

the applied potential difference between tip and sample and V_{CPD} the contact potential difference due to the difference between the tip and sample work functions, the resulting force is:

$$F_{el} = -\frac{1}{2} \cdot \frac{\partial C}{\partial z} \cdot (V_{bias} - V_{CPD})^2 \qquad (3.1)$$

where z is the tip-sample distance and C the capacitance of the system. Kelvin Probe Force Microscopy (KPFM) uses this interaction to measure the contact potential difference (CPD) between the tip and the sample with nanometric resolution. It will be explained in further detail in the following section.

AFM modes

There are two principal modes in atomic force microscopy: the **contact** and the **dynamic modes**. In contact mode, the tip is placed in direct contact with the sample, while in the dynamic mode typically the cantilever is oscillated to its resonance frequency at a given distance to the surface. Therefore, in the contact mode, the tip-sample interactions are sensed with the vertical deflection of the tip and in the dynamic mode, the interactions induce variations in the phase, frequency and amplitude of the initial tip oscillation. In the following, both modes will be described.

Contact mode

In this mode, the tip is maintained in direct contact with the sample during the measurement and the deflection of the cantilever upon tip-sample forces is monitored. When scanning, this deflection can be kept constant at a certain set point through a feedback loop that controls the z movement from the piezo. The z movement required to maintain the normal deflection of the cantilever in each point of the scanned area generates a topographic image. It is of great interest to get into detail of the typical measurement of recording the cantilever deflection as the sample is approached to and retracted from the tip,

in the so-called *Force Versus Distance* curve [78]. An example of this curve is depicted in Figure 3.4.
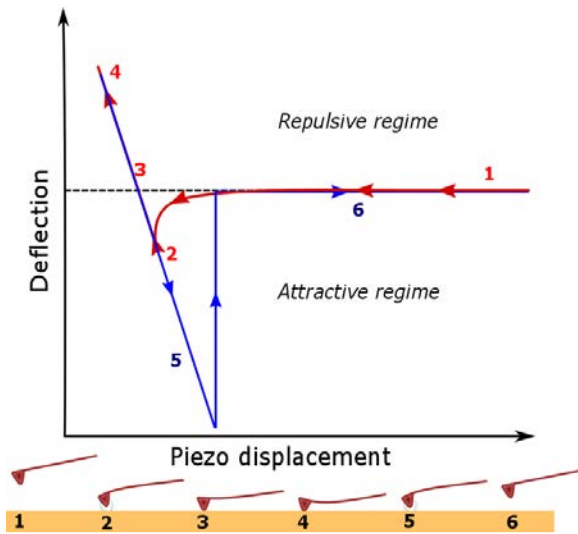

Fig. 3.4: Force versus distance curve acquired during an approach-retract cycle of the sample towards the tip. The cantilever deflection is measured as a function of the piezo displacement. The different regions correspond to the different deflection moment schematized in the bottom picture.

When the tip approaches the surface, the cantilever deflection does not change ((1) in Figure 3.4) until an attractive interaction (van der Vaals, electrostatic or capillary forces) causes a change in the cantilever deflection (2). The tip keeps approaching until these attractive forces are stronger than the restoring force from the cantilever spring, moment in which the tip suddenly jumps into contact with the surface (snap-in point). After this point, two things can happen: either the sample is deformed by the tip, which penetrates in the surface or, due to the repulsive short range forces, the cantilever deflects away from the surface linearly with the scanner movement (3)-(4). When the full extension of the piezo is achieved, the scanner begins to retract (blue line) and the cantilever deflection retraces the same curve as the tip moves away from the sample until a snap-out moment is achieved, indicating that the tip is no longer in contact. However, both curves are not exactly the same when measuring in air due to the presence

of water, which leads to capillarity adhesion forces which cause the bending of the cantilever to the surface (5). This causes an hysteresis in the curve, as the snap-out point is not observed in the same position as the snap-in, meaning that an extra piezo displacement is needed in order to detach the tip from the surface. The value of the force in the snap-out point is denoted as the adhesion or pull-off force. These curves are the result of the photodiode response V_{A-B} versus the vertical movement of the piezoelectric tube. The V_{A-B} signal must be converted into force. For that purpose, the photodiode is calibrated so the measured signals (in Volts) can be directly translated to deflection of the cantilever (in nm) and by introducing the cantilever force constant (in Nm^{-1}) the applied load (in nN) can be obtained:

$$F_N = k_Z \cdot S_v \cdot V_{A-B} \tag{3.2}$$

The cantilever force constant k_Z is provided by the manufacturer and S_v is the $nm^{-1}V$ calibration factor of the cantilever, which is extracted from the slope in the (5) region in the Force-distance curve.

Depending on the force set point, two different regimes can be distinguished whether the cantilever points away or towards the surface, denoted as attractive and attractive regimes. During this thesis, the contact mode measurements have been mainly performed in the attractive regime, as close as possible to the pull-off force, in order to avoid sample damage. In this mode, surface topography images as well as lateral deflection maps or conductivity can be obtained. In further sections, the AFM techniques to obtain friction and conductivity maps will be described.

Dynamic mode

When an oscillating tip approaches a surface, the tip-surface interactions would induce frequency, amplitude and phase variations in the oscillation. In the dynamic AFM modes, the behaviour of the vibrating cantilever is monitored when the tip approaches the sample surface. The cantilever is mechanically oscillated by electrically exciting a

piezo actuator placed in the cantilever holder, resulting in a exciting force:

$$F_{ext} = F_{ext} \cdot \sin(\omega \cdot t) \qquad (3.3)$$

This force leads to the case of a forced harmonic oscillator. When approaching the surface, the tip-sample interactions induce a shift in the resonant frequency of the cantilever. This shift is proportional to the force gradient of the tip-sample interaction and is responsible of a displacement of both the amplitude and phase responses. A more in detail description and discussion on dynamic AFM modes can be found in literature [76, 79, 80].

There are two main operation modes in dynamic-AFM: amplitude modulation (AM-AFM), and frequency modulation (FM-FM) and the main difference is the monitoring of the amplitude or the frequency shift, respectively. In AM-AFM, the cantilever is excited at a fixed frequency while the oscillation amplitude is monitored: in presence of a damping force, resulting from the interaction with the sample, the amplitude of the oscillation will decrease. The feedback loop maintains the amplitude constant by adjusting the z position of the tip and therefore a topography image (amplitude map) of the scanned surface is obtain. Simultaneously to the topography maps, the phase shift between the excitation driving force (F_{ext}) and the cantilever oscillation is recorded. Differently, in FM-AFM, the changes in the cantilever's resonant frequency are monitored. During the measurement, the tip-sample position is adjusted in order to maintain a constant frequency shift ($\Delta\omega$) with a feedback loop. By recording the z piezo displacement, a map at constant $\Delta\omega$ is built. Along this thesis, dynamic-AFM measurements have been performed with a combined mode: as in AM-AFM, the amplitude of the oscillation is the physical magnitude for the topography feedback, but a phase locked loop (PLL) is used to maintain the phase constant (which at resonance is $\phi=90°$) by varying the frequency of the external driving force F_{ext}, keeping the system in resonance, as illustrated in Figure 3.5.
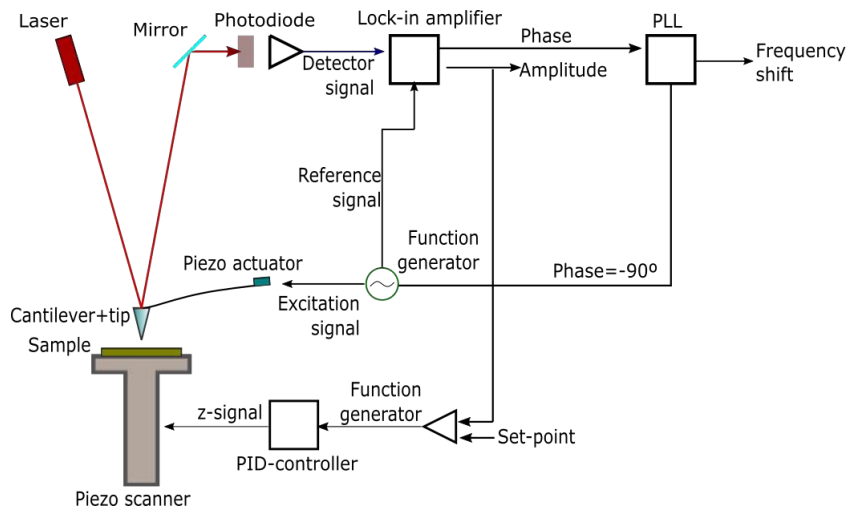
Fig. 3.5: AFM setup scheme

The physical quantities used to monitor the tip dynamics are in this case the oscillation amplitude and phase shift. Therefore, topographic and excitation maps, which provide contrast in heterogeneous samples, are obtained. During all the measurements presented in this thesis, the oscillation of the tip has been maintained in the attractive regime, in order to minimize de tip-sample contact, which is particularly suitable for the Kelvin probe microscopy technique, described in the next section.

AFM techniques

As introduced in the previous Section, AFM is sensitive to different physical and chemical interactions between the tip and the sample, making possible the development of a wide variety of derived techniques. In the following, the techniques used along this thesis will be presented.

Friction force microscopy

In Friction force microscopy (FFM), the force opposite to the relative

tip-sample motion, also known as friction force, can be measured [77, 81].
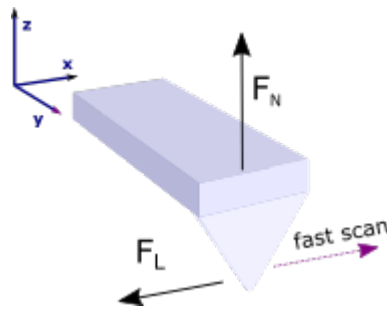

Fig. 3.6: Scheme of the AFM tip-cantilever. The tip moves with a constant speed in the fast scan direction with a controlled load in the z axis (F_N). The generated force on the tip-sample contact opposites de tip (F_L)

However, FFM does not directly measure the lateral force but the torsion of the cantilever. Therefore, in order to obtain quantitative friction values, a conversion from cantilever torsion to lateral force is necessary. For that, the torsion spring constant of the cantilever must be determined, as well as the conversion factor of the voltage difference in the photodiode. The last one can be determined by scanning a known wedge shaped structure [82], but the torsion spring value is not simple to obtain and its estimation has a very large error. During this thesis, relative studies (rather than absolute) of friction were performed and the photodiode output (in volts) is given as lateral forces. In FFM, the fast scanning direction is perpendicular to the long axis of the cantilever as shown in 3.6 so, when it senses the frictional forces, the motion of the tip induces a torsion of the cantilever. Since lateral force caused by friction always opposes the tip motion, the sense of this twist reverses when the scan direction is inverted. In this thesis, the two scan directions (when the relative motion of the tip is from left to right or vice versa) are called forward and backwards respectively (Figure 3.7). These two directions would produce a clockwise (positive V_{1-2}) or a counter clockwise (negative V_{1-2}) turn in the cantilever, which results in a positive or negative magnitude of the lateral force F_{LF}. When the tip encounters a region with different

frictional behaviour (dark parts in the image), the magnitude of the torsion changes. The torsion dependence on the scan direction gives rise to a friction loop as shown in Figure 3.7. The area enclosed in the loop is equal to the dissipated energy of the cycle.
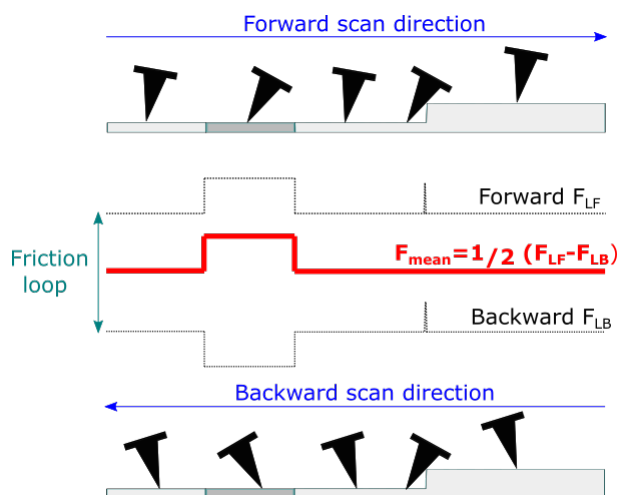

Fig. 3.7: Friction loop formed by the trace and retrace lateral signals along the same scanned line. The upper and lower pictures represent the torsion movement of the tip as it encounters areas of different frictional properties or topographic changes. Dashed lines are the corresponding lateral force profiles and the solid red line is the friction force obtained from equation 3.4.

When scanning heterogeneous sample, the tip experiences different twists depending on the tip-surface interaction. Therefore, the FFM technique can be sensitive to the chemical termination, packing, molecular order or hydrophobicity of the surface and conforms a powerful tool to distinguish materials that do not show any features in the topography images. In Chapter 5, this capability will be used to distinguish between two different species in mixed self-assembled monolayers. The magnitude of the sliding frictional force can be extracted from the height of the loop with the following relationship:

$$F_{FFM} = \frac{1}{2} \mid F_{LF} - F_{LB} \mid \qquad (3.4)$$

However, not only friction can contribute to the lateral forces, but also the local topography variations. This is exemplified in the signal response when encountering a step in Figure 3.7. By applying equation 3.4, we exclude this non-dissipative contribution. This technique provides with Friction maps, that contain information of the chemical, structural or molecular orientation of the sample [83–85], which can be correlated with the topographic signal. The origin of friction on an atomic level lays in the interacion between atoms. The underlying mechanism of friction is the so called *stick-slip* phenomenon and has been discussed several times in different experimental and theoretical works [86–88]. The theory behind this model is supported by the Tomlinson model, which analitically describes the tip-sample contact with a periodic interaction potential (Figure 3.8(a)). The motion equation if the tip in this one dimensional interaction potential can be described by:

$$m_x\ddot{x} = k_x \cdot x_M - \frac{\partial V_{int}(x)}{\partial x} - \gamma\dot{x} \qquad (3.5)$$

Where m is the effective mass of the system, x_M is the equilibrium position of the spring and γ is the damping constant that describes other mechanisms of energy dissipation such as phonons or electric excitations. The periodic potential can be described as:

$$U_{int} = U_0 \cos\frac{2\pi x}{a} \qquad (3.6)$$

where a is the unit cell and U_0 is the corrugation energy amplitude. In Figure 3.8(b) is represented the combined action of the parabolic potential of the tip and the periodical surface potential. In the initial position, the tip is found in a potential minimum. When the tip moves, an elastic energy must be overcome due to the static friction developed between tip and sample. This means that when the tip is pushed laterally, it will remain at that minimum until the restoring force of the cantilever is larger than the energy barrier, causing the tip to slip to the nearest local equilibrium position. There, the lever relaxes, releasing energy and the motion is stopped as the equilibrium is reached again.
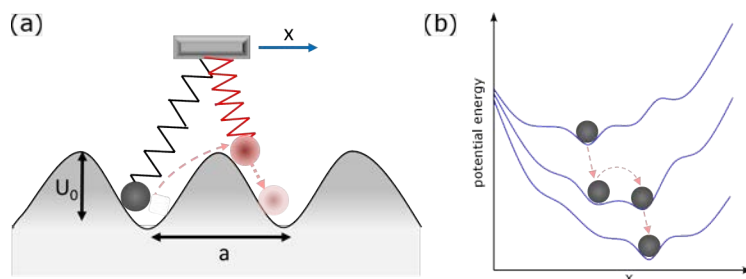
Fig. 3.8: (a)Cartoon of the stick-slip behaviour, in which the path of of a point like tip interacting with a one-dimensional periodic atomic surface potential is described. (b) Total potential diagram of the Prandtl-Tomlison model during the tip movement. Adapted from reference [86].

The stick-slip phenomena can be observed when performing high resolution lateral force images in periodic atomic or molecular lattices. The resultant lattice-resolved images can carry very useful information and, through this thesis, they have been used to structurally characterize crystalline materials, to distinguish coexisting domains of the same molecular crystal, to identify specific materials in heterogeneous films or to determine the crystalline molecular orientation.

Transverse Shear Microscopy

In the previously explained FFM technique, the scanning direction is oriented perpendicular to the cantilever axis. Last et al. first reported a variation in contrast between different domains in a β -(ET)$_2$I$_2$ monolayer when varying the scanning direction from 90° (perpendicular) and 0° (parallel) [89]. Further studies have been performed using this method, the so called transverse shear microscopy (TSM). Putambekar et al. performed these measurements in pentacene layers grown on SiO$_2$, concluding that the orientation of the domains of the surface with respect to the scanning direction was responsible for this visible contrast between different grains [90]. The TSM technique was a main object of study during this thesis and in Chapter 4 will be explained in detail.

Conductive scanning force microscopy

Conductive atomic force microscope (C-AFM) is based in the use of a conductive tip for scanning the surface, which allows measuring with nanometric resolution the current flowing between tip and sample upon an applied voltage. In this AFM technique, the conductive tip
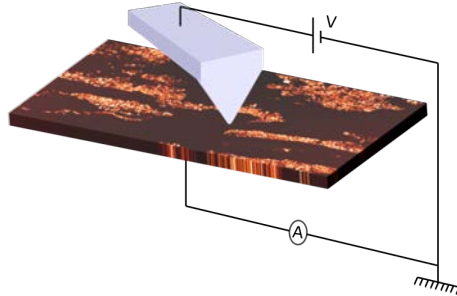

Fig. 3.9: Scheme of the C-AFM experimental setup.

is placed in contact with the sample surface forming an electrical contact. Upon an applied voltage difference between tip and sample, a current flow can be measured as a function of the position. Simultaneously, topography is also mapped so that both magnitudes can be directly correlated [91]. An scheme of the technique is depicted in Figure 3.9. During this thesis, two different experimental setups have been used. The equipment used for most of the measurements was purchased from *Nanotec Electronica* [92]. In the C-AFM mode, the bias is applied to the tip and the current is collected through the sample, as depicted in the sketch in Figure 3.9. When a positive bias (V_{tip}>0) is applied to the tip, the current flows from the sample to the tip and, in the obtained current maps, the brightest parts correspond to higher current values. In Chapter 5, some of the C-AFM current maps were obtained during my two short stays in LTI (Karlsruhe) using a Bruker Dimension ICON AFM [93]. In this set up, the voltage bias is applied to the sample, while the current is collected through the tip. With this configuration, when a negative bias is applied to the sample (in an equivalent situation to V_{tip}>0 in the *Nanotec* instrument), the electrons flow from the sample to the tip and, in the current maps, the bright parts correspond to more conductive parts. During these measurements, some parameters become critical, such

as the tip-sample contact area, the environment humidity or the tip coating conditions. Therefore, during this thesis, in order to follow a reliable procedure, only curves taken in the same tip conditions have been compared.

Kelvin probe force microscopy

The macroscopic Kelvin probe method is based on the parallel-plate capacitor concept formed by the sample and a oscillating metallic probe [94]. It was first developed by lord Kelvin [95], who measured the contact potential difference (CPD) between zinc and copper by nullifying the field between the two plates capacitor formed by the two materials.

This method offers a direct measure of the work function (ϕ) of a material. The work function is defined as the needed energy to remove one electron, originally in the Fermi level (E_F) and place it at rest in a point in the free space above the vacuum state (E_{vac}).

When we consider two metallic materials with different work functions (for example, the AFM tip and the sample), the energy level scheme is as depicted in Figure 3.10 (a). When the two materials are electrically connected, electrons flow from the material with the lowest work function (the sample, in Figure 3.10 diagram) to the material with the highest work function until their Fermi level align. Due to this charge movement, a contact potential difference and electrostatic force develops (Figure 3.10 (b)) between tip and sample. By applying an external bias between the probe and the sample, this electrostatic force can be nullified, as depicted in Figure 3.10 (c). The bias value at which this force is nullified and therefore, the vacuum levels are flattened, is defined as V_{CPD}. The contact potential difference (CPD) between the two materials is defined as:

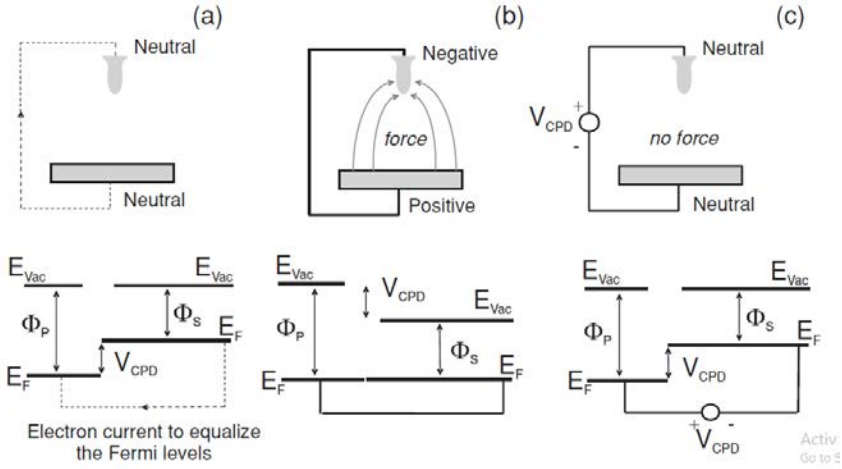$$CPD = \frac{\phi_{sample} - \phi_{tip}}{q} = \frac{\Delta\phi}{q} \qquad (3.7)$$

Fig. 3.10: Energy level diagrams of the basic measurement set-up of contact potential difference (CPD) in which probe and sample form a capacitor with work functions ϕ_p and ϕ_s respectively. In (a), the metals are isolated. When electrically connected (b), the Fermi levels (E_F) align generating a potential drop in their vacuum levels. When V_{CPD} is applied. the vacuum levels are flattened. (c) Adapted from reference [96].

Where ϕ_{probe} and ϕ_{sample} are the work functions of the tip and the sample,respectively and q is the elementary charge.

If we consider that the tip and the sample are forming a plane capacitor, the electrostatic force between both is described by equation 3.1. In KPFM, in order to separate other forces contribution (mainly van der Waals and chemical forces), an ac bias V_{AC} with a frequency ω is applied to the KPFM tip, keeping the sample grounded. Therefore, equation 3.1 becomes:

$$F_{el} = -\frac{1}{2}\frac{\partial C}{\partial z}[(V_{DC} - V_{CPD}) + V_{AC}\sin(\omega t)]^2 \qquad (3.8)$$

Where V_{DC} is an applied bias to the tip. Developing equation 3.8, we find that the electrostatic force can be separated in three terms:

$$F_{el} = F_{DC} + F_{\omega} + F_{2\omega} \qquad (3.9)$$

where;

$$F_{DC} = -\frac{1}{2}\frac{\partial C}{\partial z}[(V_{DC} - V_{CPD})^2 + V_{AC}^2] \qquad (3.10)$$

$$F_{\omega} = -\frac{\partial C}{\partial z}(V_{DC} - V_{CPD})V_{AC}\sin(\omega t) \qquad (3.11)$$

$$F_{2\omega} = \frac{1}{4}\frac{\partial C}{\partial z}V_{AC}^2\cos(2\omega t) \qquad (3.12)$$

As a result of the F_ω and $F_{2\omega}$ components, the amplitude has an harmonic response at at ω and 2ω frequencies, being F_ω used to measure the V_{CPD}. $F_{2\omega}$ is frequently use for capacitance microscopy [97] and F_{DC} contributes to a static deflection of the cantilever. The KPFM technique is based on nullifying the term F_ω by applying a variable dc voltage to the tip V_{DC} which equals to V_{CPD}. In each scanning position, V_{DC} is adjusted to the local CPD value providing a V_{CPD} map, also called surface potential map. This method is known as amplitude mode Kelvin probe force microscopy (AM-KPFM). An alternative operating mode, based on monitoring the electrostatic response in the frequency shift (Δ f) at a certain ω is named FM-KPFM and described by the following equation:

$$\Delta f(\omega) \propto \frac{\partial F_\omega}{\partial z} = \frac{\partial^2 C}{\partial^2 z}(V_{DC} - V_{CPD})V_{AC}\sin(\omega t) \qquad (3.13)$$

In FM-KPFM, ∂F_ω is used as a physical magnitude in the feedback loop instead of F_ω. By this method, the contribution of the cantilever an the tip cone to the electrostatic force is avoided, thus enhancing the lateral resolution and improving the signal to noise ratio [98]. During this thesis, FM-KPFM has been employed in the so called a single-pass mode. So, besides the amplitude and PLL feedbacks (explained in section 3.3.1), a third feedback keeps $\frac{\delta(F_\omega)}{\delta z} = 0$ providing the surface potential map. In certain measurements, in combination to the single pass FM-KPFM, the so called lift mode or retrace has been employed, reproducing in a second pass the topography by lifting the tip a known amount. This was used to assure that the KPFM was performed in non-contact conditions. Most of the measurements were made by lifting the tip a vertical distance of 10-20 nm.

Instead of taking surface potential images, the CPD can be measured at a particular point. The electrostatic force between a tip and the sample was given by equation 3.1. When a bias V_{DC} is applied to the tip, the tip-sample potential difference results $V = V_{tip} - V_{CPD}$ and the electrostatic force (F_{el}) as a function of the applied bias will be a parabola centred in V_{CPD}. Therefore, by sweeping the bias while measuring the normal deflection (F_N), a CPD value can be extracted. In the KPFM set-up employed during the thesis, not only the normal force but also the frequency or the phase shift can be employed and quantitative values can be obtained from both mapping the surface by adjusting V_{DC} or by performing Δf versus V_{DC} curves. In the latter, the frequency or phase shift of the oscillating probe is proportional to the force gradient, so it will present the following dependence:

$$\Delta f \propto \frac{\partial^2 C}{\partial^2 z}(V_{DC} - V_{CPD})^2 \qquad (3.14)$$

Figure 3.11 shows an example of these measurements. A patterned SAM surface was prepared with a fluorinated phosphonic acid that only covers $3\mu m$ squares. Figure 3.11 (a) shows the CPD map, revealing areas with a $\sim$ 0.8 V contrast. Phase shift versus voltage curves performed on top of the different areas are shown in (b). As expected, the CPD values calculated from the maximum of the curves are separated by a ΔCPD amount of $\sim$ 0.8 V. This example illustrates the typical measurement procedure followed during this thesis, as all the CPD maps have been cross-checked with the value obtained from parabolae taken in several locations through all the experiments. Moreover, to avoid the undesired effect of tip changes, measurements on a grounded metal, whose work function is well known, were taken before and after the measurements to assure reproducibility.

The main equipment used during this thesis has been a commercial AFM from Nanotec Electrónica. Some experiments performed in the LTI were done with a Bruker Dimension ICON AFM system. The sofware used for data acquisition and image processing is the freeware WsXM [99].
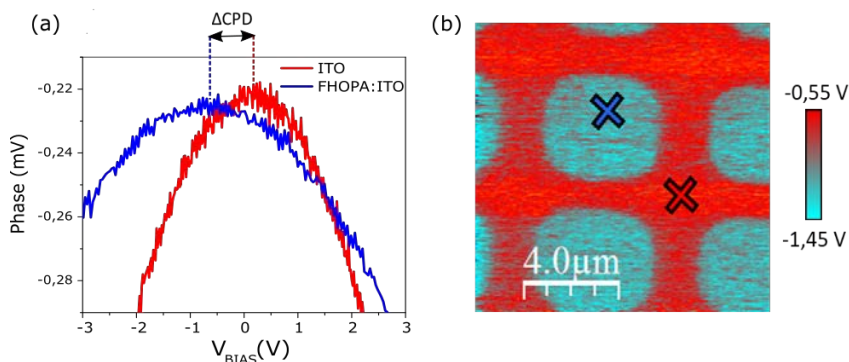
Fig. 3.11: KPFM map of an indium tin oxide (ITO) substrate treated by micro contact printing to obtain a patterned self assembled monolayer of FHOPA (a) and Phase-bias parabolae taken in each one of the two materials. (b) The contrast shown in the image corresponds to the CPD difference observed in the curves.

3.3.2 X-ray diffraction

During this thesis, X-ray diffraction has been use to obtain structural information of different organic systems. In order to obtain both in plane and out of plane information, different measurements can be made. In Figure 3.12, the scheme for **specular x-ray reflectivity** in a multilayer and **grazing incidence wide-angle x–ray diffraction** (GIWAXS) are displayed. The specular diffraction typical set up is shown in Figure 3.12 (a). The incident x-ray (k_i) hits in the sample at a small angle, α_i, and are detected (k_f) at $\alpha_i = \alpha_f$. In this configuration, the momentum transfer $q = k_f - k_i$ is perpendicular to the surface (in the so called *z-direction*) and is given by the Bragg's law:

$$q_z = \frac{4\pi}{\lambda} \sin \alpha_i \qquad (3.15)$$

where λ is the wavelength of the incoming x-rays. The direction of reflected vector will depend on the crystallographic planes of the sample, and therefore the diffraction pattern will be influenced by the
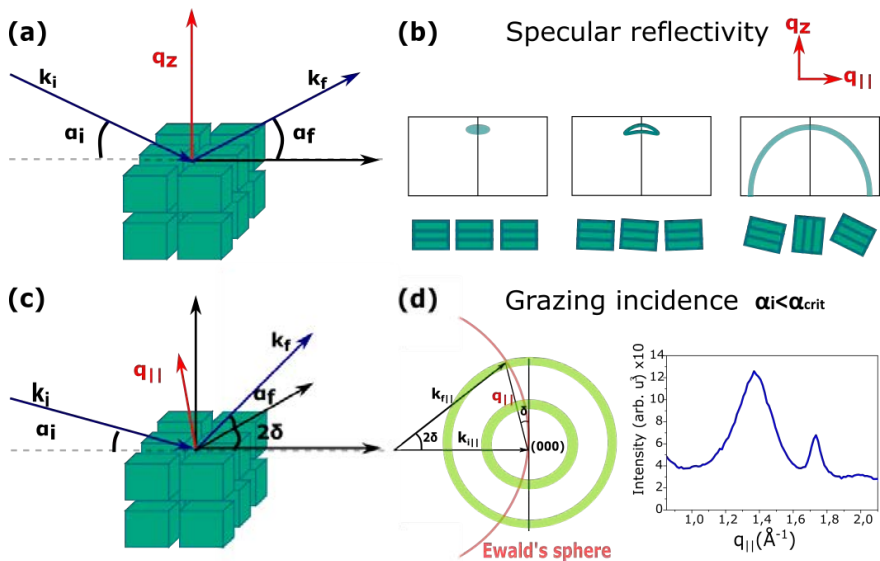
Fig. 3.12: Scheme (a)(c) and representative results (b)(d) of Specular (up) and grazing incidence x-ray refraction (down) measurements.

orientation of the diffracting crystals. The typical results are displayed in Figure 3.12 (b). As can be observed, when most of the crystals present an out-of-plane (perpendicular to the plane) orientation, the diffraction pattern consists in a spot. As the out-of-plane orientation is no longer the preferred one, the spot becomes broader including all the present orientations in the film. In a film with isotropic crystal orientation, diffraction will result in a uniform ring in the detector. In order to obtain intensity in this spots, the sample must be rotated so the Bragg condition is fulfilled.

In grazing incidence x-ray diffraction, the angle α_i of the incoming x-ray beam is set to be smaller than α_{crit}, which is the angle at which total external reflection takes place. In this condition, one can extract the in-plane structural information of a film. The momentum transfer, which has almost no specular component, i.e. $q_z \simeq 0$, is determined by the component $q_{\parallel}$ in the plane, as schematized in Figure 3.12 (c). The $\delta-$scan in reciprocal space for a film with randomly oriented domains is schematized in Figure 3.12 (d). The $\delta-$scan scans along the Ewald sphere (a geometrical construction formed by k_f and k_i)

at α_{crit}, and intersects the rings of the randomly oriented crystalline domains. Therefore, two dimensional crystallographic information is obtained. At the right, a typical $\delta-$scan is shown for a film with randomly oriented crystalline domains.

For the results presented in Chapter 5, Grazing-Incidence Wide-Angle X-ray Scattering (GIWAXS) measurements were done at the Angstromquelle Karlsruhe (ANKA), Germany, with 12 keV photon energy at the beamline MPI. The 2D frames were taken with a X-ray area detector (Mar-CCD) and the in plane scans were obtained with a point detector varying the incident angle from 0.10° (below the critical angle) to 0.14° (above the critical angle).

3.3.3 Device characterization

Organic Solar Cells

For the results presented in Section 5.1, current-voltage measurements were carried out in Nitrogen environment in a spectrally monitored solar simulator (Oriel 300 W, 1000 W m^2, ASTM AM 1.5G), calibrated by a KG5 filtered silicon reference cell (91150$-$KG5, Newport) using a Keithley 238 source meter. The whole measuring station was placed inside a glovebox. The intensity of the solar simulator was regulated using various optic filters.

The measurements presented in Section 6 were carried out with a WACOM 2-lamp solar simulator (class AAA, AM1.5G) and a Keithley 2400 current source measure unit. Short circuit current densities were verified by quantum efficiency measurements performed using equipment from Optosolar

Organic Thin Film Field Effect Transistors

The current versus voltage characteristics were measured in a Süss probe station under ambient conditions using a Keithley 2612AB. For obtaining the output, a voltage was applied to the gate while the value of the drain-source voltage was swept in forward and reverse directions while recording the drain current, I_{SD}. This measurement was repeated for several gate voltage values, typically from -40V up to 40V in the studied OFETs. To measure the transfer characteristics, a constant voltage is applied to the drain and I_{SD} was measured at each point while sweeping gate voltage in forward and reverse. Same gate and drain voltages were applied during KPFM measurements.

Physical origin of TSM

4

Contents

This chapter is adapted from the publications [100, 101].

4.1 Motivation: FFM and TSM

The importance of the crystalline structure is well known in organic electronics [102–104]. For example, single crystal organic devices show much better properties than thin films due to the absence of structural defects like grain boundaries. In particular, in organic thin film transistors, the charge transport takes place within the first few layers in contact with the gate dielectric. Thus, its crystalline quality has a strong impact in the devices performance [56, 103, 105–112].

Furthermore, the type of molecular packing strongly influences the charge transport, for example leading to a carrier mobility anisotropy [113]. For polycrystalline films it has been shown that the boundary effects in slip-stacked materials, due to grain defects, can dominate the charge transport through the film. Therefore, understanding the formation, distribution and role of the grain boundaries and the

molecular packing at a molecular scale can provide with important guidelines for designing high performance devices.

As detailed in section 3.3.1, FFM is a powerful experimental tool capable to provide spatially-resolved structural information. In some systems, the surface structure of the of the crystaline materials is reflected in friction anisotropy that lead to contrasts in the lateral force images that do not appear in topographical images taken by AFM. An example is depicted in Figure 4.1, in which a film of N,N−dioctyl−3,4:9,10-perylene tetracarboxylicdiimide (PTCDI-C8) film grown by OMBD. Perylene diimide (PTCDI) derivatives are considered to belong to the most promising and versatile materials to fabricate n-channel OFETs [113–117]. When evaporated onto SiO_2, PTCDI-C8 molecules self-assemble in a nearly perfect layer-by-layer fashion, forming a smooth layered film. Each layer ($\approx$ 2nm thick, consistant with previous reports [118, 119]), presents a slipped cofacial packing driven by the stacking between molecules, as depicted in the scheme and profile in Figure 4.1 (a) and (b) [120, 121]. Although in the topographical images (c) no contrasts are found within the same island, a close inspection of the Lateral Force image in (d) reveals faint variations in some islands. This contrast heterogeneity within the same island indicates a friction anisotropy caused by the different azimuthal orientation of the crystalline domains.

As briefly explained in section 3.3.1, TSM is an unconventional FFM mode in which the cantilever is oriented perpendicularly to the scanning direction. Interestingly, in the organic film presented in Figure 4.1 (as well as in a wide range of organic crystals), when scanning in TSM mode, much more remarkable and varied contrast appear in the lateral force map (Figure 4.1 (e)) which do not appear when measured in FFM mode (Figure 4.1 (d)).

While the physical phenomena responsible for FFM (dissipative forces) is clear, the physical origin of the TSM contrast remains controversial. Kalihari et al. attributed the TSM contrast to the shear force caused by
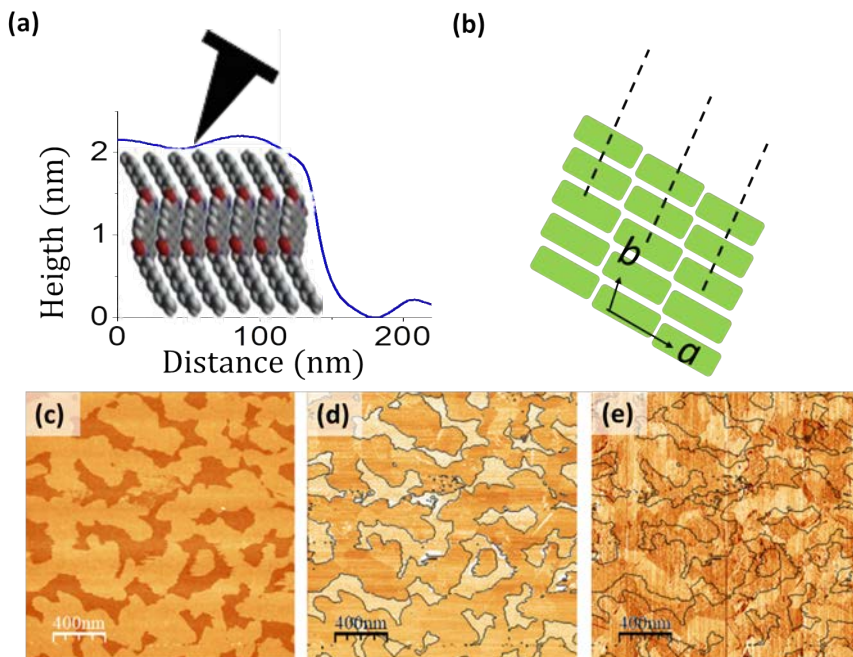
Fig. 4.1: (a) Height profile of a PTCDI-C8 thin film. (b) In-plane top view scheme. Topographical (c), FFM (d) and TSM (e) images of a PTCDI-C8 (top) crystalline film.

elastic deformation and ultimately related to the in-plane anisotropy of the elastic tensor [122]. A different explanation was given by Campione et al. who proposed friction anisotropy, caused by the corrugation of the crystal surface, as the direct cause of the TSM signal [123, 124]. Whereas atomic-scale studies based on FFM have been crucial for advancing the understanding of friction [77, 86–88], there are no atomic-scale studies which can provide insight into the physical aspects of the tip–sample responsible of the TSM signal. Motivated by that, we performed an experimental and theoretical investigation of TSM at a molecular scale using the organic semiconductor PTCDI-C8.

4.2 Angular dependence of the TSM and FFM signal

In FFM, the trace scan always induces a clockwise twist of the cantilever (a positive signal in the photodetector in the torsion axis) when scanning in the forward direction and a counter-clockwise twist when scanning in the backward direction, as depicted in Figure 4.2. Therefore, the measured frictional force (proportional to forward minus backward scans, as explained in Section 3.3.1) is always positive.
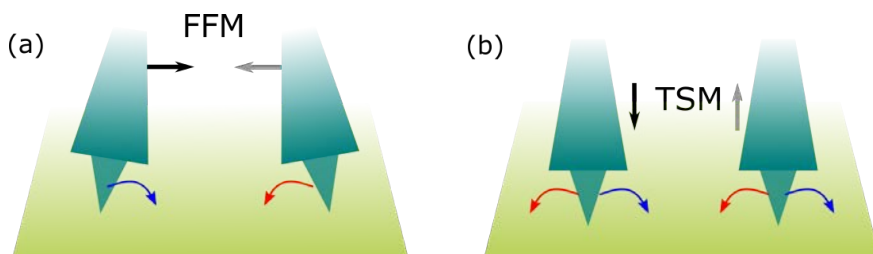
Fig. 4.2: Schematic of the sliding geometry (scan direction and torsion) in the FFM and TSM modes.

Differently, in TSM, the forward scan can result in either clockwise or counter-clockwise (Figure 4.2).
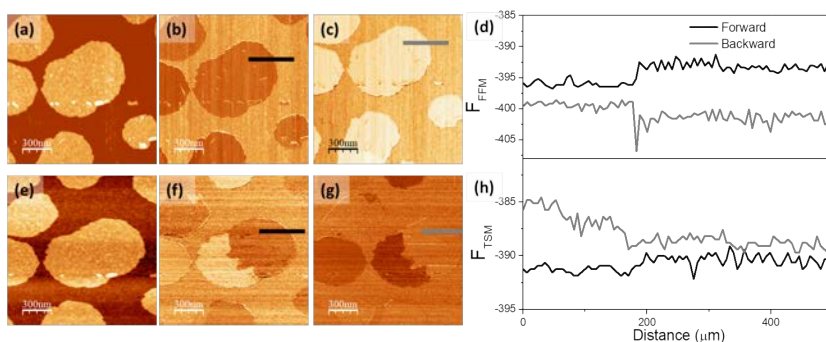
Fig. 4.3: Topographical (a) and(e), lateral force in the forward (b) and (f) and backward (c) and (g) images of the same area measured in FFM (up) and TSM (down) modes of a PTCDI-C8 submonolayer. Profiles traced along the marked lines correspondant to (d) FFM and (h) TSM.

This is manifested in the profiles shown in Figure 4.3. As the TSM signal can be either positive or negative, depending on the relative orientation between the scan vector and the surface crystallographic directions, the forward and backward signals can overlap or surpass each other, as depicts the profile (h) in Figure 4.3. Therefore, the dark/bright (negative/positive) colour observed in the TSM lateral force images in Figures 4.1 and 4.3 reflects the counter clockwise/clockwise torsion experienced by the tip.

The dependence of the TSM contrast with the surface crystallography details can be explored by measuring the torsion response along different crystallographic directions. Kalihari et al. demonstrated the dependence of the TSM signal with the surface orientation by rotating a pentacene crystal while maintaining the scan direction unchanged [125]. In this work, a submonolayer of PTCDI-C8 was used as benchmark, because the formed islands show a rich variety of contrasts when scanned in the TSM mode. As shown in Figure 4.3, when images of the same area are scanned in FFM and TSM, significant differences are observed. In the FFM image (Figure 4.3(b) and (c)), the PTCDI-C8 islands are distinguished from the surrounding substrate by a dark colour in the lateral force due to the lower frictional force sensed by the tip on them as compared to the substrate. A close inspection reveals only a slight contrast between some crystalline domains. Differently, in the TSM image (Figure 4.3(f) and (g)) a high contrast is observed making visible domain boundaries not observed in FFM. In the case of the FFM response, it is clear that the faint variations in some islands indicates friction anisotropy caused by the different azimuthal orientation of crystalline domains, otherwise expected to exist for the growth of an anisotropic two-dimensional (2D) lattice as that of PTCDI-C8 on an isotropic surface such as SiO_2. However, the strong contrast in the TSM signal is not completely explained.

When molecular resolution images are taken, rows corresponding to the packing motif of PTCDI-C8 molecules with different orientations

are observed. This is illustrated in Figure 4.4 (c), in which molecular resolution of three differently oriented domains coexsting side by side is achieved, and allows us to correlate the different contrasts visible in large scale TSM images (Figure 4.4 (b)) with the different azimuthal orientation of the domains with respect to the scanning direction. Therefore, this method can be employed for revealing the azimutal orientation of crystalline domains in organic thin films [122, 126]. So, by combining larger scale images with molecular
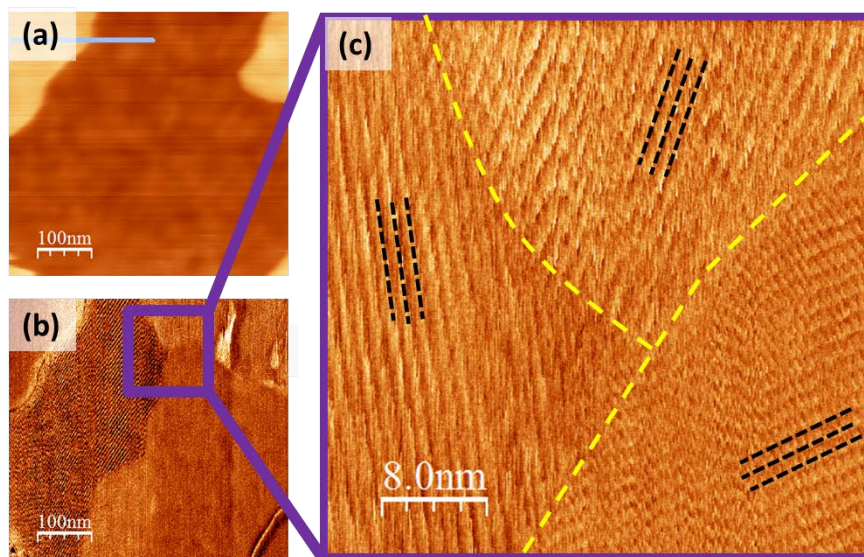
Fig. 4.4: (a) Topographical, (b) lateral force image obtained in TSM mode and (c) high magnification image of the marked area in a PTCDI-C8 film. The molecular orientation for each domain is indicated by dashed black lines(e).

resolution images, the structure in each domain can be deciphered. The periodicity found in the molecular-scale images is of ≈ 1 nm, corresponding to the distance between rows in the 2D unit cell of PTCDI-C8 molecules, an additional periodicity of ≈ 0.5 nm can also be appreciated along the rows that corresponds to the b parameter of the surface lattice [120] schematized in Figure 4.1. In order to determine the azimuthal orientation of the molecular domains, ϕ is defined as the angle defined by the molecular rows (b$-$axis) and the +x$-$axis (perpendicular to the scanning direction). Figure 4.5 shows molecular scale images illustrating the torsion signal measured in the

TSM mode for three crystalline domains exhibiting different azimuthal orientation. Though the line profiles corresponding to domains (a)
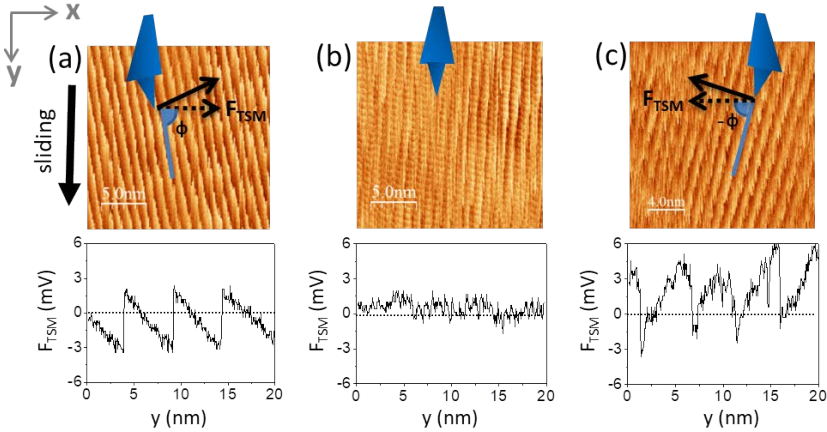
Fig. 4.5: Top: 30 nm sized molecular-scale TSM images (forward) in three domains: $\phi \approx 70°$ (a), $\phi \approx 90°$ (b) and $\phi \approx 70°$ (c). In (b) the intra-row periodicity is appreciated. Bottom: Corresponding profiles along the sliding direction (y-axis). In each case the saw-tooth modulation corresponds to the distance between rows along the y-axis.

and (c) show a remarkable saw-tooth behaviour characteristic of the tip stick-slip motion, for the domain in (b), where the rows are oriented parallel to the sliding direction, a very faint lateral force signal is obtained. It must be noted that for this domain the intra-row periodicity (≈ 0.5 nm) is observed. For (a) and (d), in which the molecular rows form angle of $\phi \approx 70°$ and $\phi \approx 70°$ respectively, a remarkable saw$-$tooth behaviour is present in the lateral force profiles. The opposite sign of the lateral force for these two domains is a direct consequence of the sense of the cantilever torsion when encountering the rows. As explained in section 3.3.1, the stick-slip behaviour occurring in atomic-scale FFM imaging is identified as the underlying dissipative mechanism of atomic-scale friction.

4.3 Two dimensional model

In order to model the tip interaction when sliding in a two dimensional surface like the PTCDI-C8 crystal, we employ the Prandtl-Tomlinson model in two dimensions developed by Dr. Enrico Gnecco.

If we apply the Prandtl-Tomlinson model at zero temperature and quasi-static conditions for the simple case of a surface consisting on parallel grooves, the interaction potential can be described as:

$$U_{int}(x, y) = -\eta \cos x \tag{4.1}$$

where $\eta = 4\pi^2 U_0/ka^2$ defines the strength of the energy corrugation $2U_0$ with respect to the spring energy (k is the spring constant and a is the channel periodicity). In equilibrium conditions $\nabla U_{tot} = 0$, we get:

$$\frac{y}{x + \eta \sin x} = \frac{\nu_y}{\nu_x} \equiv \tan \phi \tag{4.2}$$

The corresponding spring force is:

$$F_x = \nu_x t - x = \eta \sin x \tag{4.3}$$

$$F_y = \nu_y t - y = 0 \tag{4.4}$$

The equilibrium position moves forwards when the pulling spring is elongated along the direction of the movement until it reaches the critical position x_c, defined by:

$$\partial^2 U/\partial x^2 = 1 + \eta \cos x_c = 0 \Rightarrow x_c = \arccos(-1/\eta) \tag{4.5}$$

We can obtain the spring force in this static position (F$_{stat}$), in which the equilibrium becomes unstable by introducing x_c in equation 4.3:

$$F_{stat} = \eta \sin x_c = \eta \sqrt{1 - \cos^2 x_c} = \sqrt{\eta^2 - 1} \tag{4.6}$$

F$_{stat}$ is defined in the x direction. When it is projected along the scan direction, we obtain:

$$F_{FFM}^{slip} = \sqrt{\eta^2 - 1} \cos \varphi \qquad (4.7)$$

Which corresponds to the peak value in the FFM signal. The corresponding projection in the perpendicular direction (which defines the TSM signal recorded by the photodiode) at x_c:

$$F_{TSM}^{slip} = \sqrt{\eta^2 - 1} \sin \varphi \qquad (4.8)$$

The angle φ is related to the angle ϕ in Figure 4.5 by $\phi = 90° - \varphi$ for FFM and $\phi = \varphi$ for TSM. Therefore, these forces would depend on the angle between the scan direction and the rows orientation as:

$$F_{FFM} \propto |\sin \phi| \qquad (4.9)$$

and

$$F_{TSM} \propto -\sin \phi \qquad (4.10)$$

where $-90° \leq \phi \leq 90°$. In the large scale images, we can obtain the sign and magnitude of the TSM and FFM signals for each domain distinguishable in the TSM signal. This value is calculated by substracting the value measured in the forward and backward images given by equation 3.4. In order to remove any possible extrinsic effects, each signal value was normalized with respect to that of the isotropic surrounding SiO$_2$ substrate. The PTCDI-C8 submonolayer presents a large anisotropy in the TSM signal images and, as depicted in Figure 4.6, we are able to determine the direction of the molecular rows for each domain.
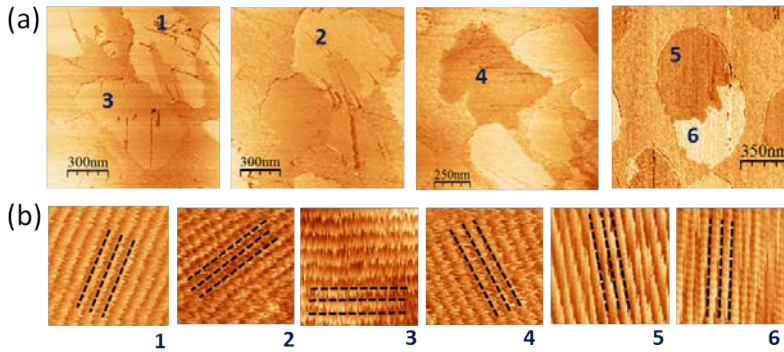
Fig. 4.6: (a) Large scale FFM images and (b) 10 nm molecular resolution images obtained in the areas labelled in (a). The angle ϕ between molecular rows and the x-axis is easily determined from the stick-slip images in (b) for each case.

Thus, we are able to correlate the value of the normalized FFM and TSM signals in each domain with its molecular orientation. This normalized FFM and TSM signal is calculated as explained in Section 3.3.1 using equation 3.4. In Figure 4.7, the experimental data for TSM and FFM in differently oriented domains is plotted. First, it must be noted that for TSM, a good agreement is observed with the predicted sinusoidal behaviour (black dashed line corresponds to equation 4.10), indicating that the corrugation perpendicular to the molecular rows has a dominant effect on the tip trajectory and the resulting cantilever torsion when scanning in TSM mode.

However, there is a strong disagreement between the experimental FFM data and their expected angular dependence. In particular, when $\phi = 0°$ the FFM should vanish (equation 4.9), which is not observed experimentally. This discrepancy stems from the fact that the proposed model does not account for the molecular perodicity along the rows (corresponding to the projection of the b PTCDI-C8 lattice parameter along the x axis). This corrugation, however, is observed in the FFM image for this particular orientation (Figure 4.7, right) and is at the origin of the stick-slip. Therefore, it seems of importance to replace the $1-$dimensional model used so far with another more realistic
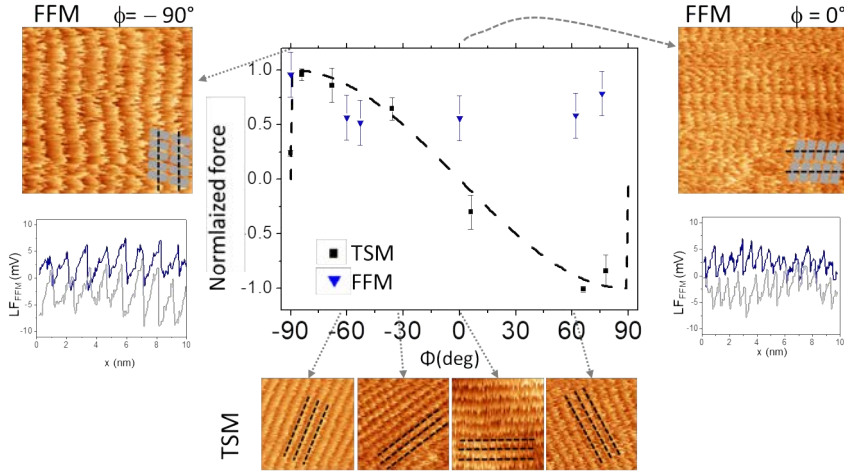
Fig. 4.7: Normalized experimental FFM and TSM signals for domains with diverse azimuthal orientation. Bottom: representative TSM images. FFM molecular scale images (and profiles) for two domains oriented parallel (right) and perpendicular (left) to the molecular rows.

which takes into account both a and b parameters as well as the symmetry of the PTCDI-C8 lattice. In order to do that, we replace equation 4.1 by a 2D interaction potential (equation 4.1) resembling the symmetry of the surface:

$$U_{int} = U_0 \cos \frac{2\pi x}{a_x} + U_1 \cos[\frac{2\pi}{b}(y - \frac{a_y}{a_x}x)] \qquad (4.11)$$

where $a_x = a\cos(90° - \gamma) = 0.83$ nm, $a_y = a\sin(90° - \gamma) = $ -0.349 nm and $b = 0.498$ nm. In this interaction potential, the first term corresponds to the potential corrugation perpendicular to the molecular rows, with amplitude of U_0 and periodicity equal to the distance between the rows (projection of a along the x-axis marked in Figure 4.5). The second term, with amplitude U_1 accounts for the smaller corrugation along the rows. Thus, this bidimensional potential provides the 2D oblique lattice unit depicted in Figure 4.8(a) reproducing the experimental one. The 2D potential described in equation 4.11 is shown in Figure 4.8, giving some examples of domains in which the tip slides along the crystallographic directions of the PTCDI-C8 surface lattice. The dynamics of a tip interacting with the 2D potential de-
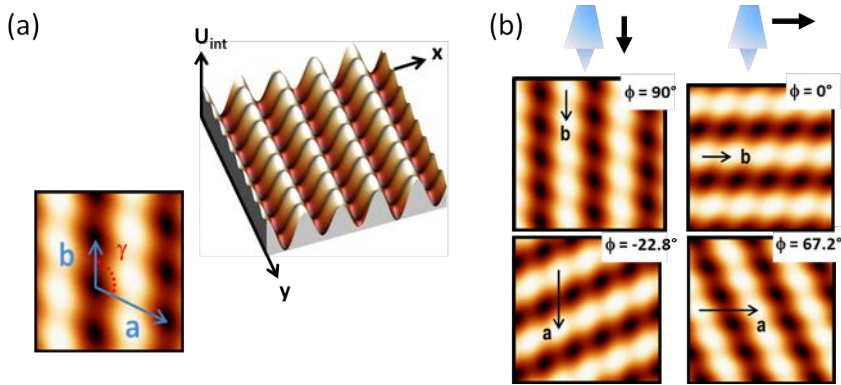
Fig. 4.8: (a) 2D and 3D views of the interaction potential (U_{int}) corresponding to equation 4.11 reproducing the symmetry of the PTCDI-C8 surface lattice ($\gamma = 112.8°$). (b) Domain orientations for which the principal crystallographic directions the molecular 2D lattice are parallel to the sliding direction in TSM (left) and FFM (right).

scribed in equation 4.11 have been computed by solving the Langevin equation [127] at 300K [128]. For the corrugation amplitude defined by the molecular rows, we have used the experimental results of the stick-slip profiles when scanning parallel and perpendicular to the molecular rows, as the ones shown in Figure 4.7.

Thus, a value of $U_0 = 0.25eV$, in the range of typical surface potentials, was chosen, while for the corrugation amplitude along the molecular rows the relationship $\frac{U_1}{U_0} = 0.2$ was applied. The result of the simulation is shown in Figure 4.9, where the angular dependence of the FFM and TSM signals is plotted. It is clear that the minor corrugation along the rows (introduced in the second term in equation 4.11), and the fact that the lattice vectors a and b are not perpendicular to each other results in some important anisotropy effects which are also observed in the measurements. For example, the TSM signal is zero at $\phi \approx -20°$, instead of at $\phi = 0°$, due to the alignment of the sliding direction with the a-axis (Figure 4.8 (b), left). On the other hand, the maximum FFM signal is reached when the top crosses the molecular rows along the a-axis ($\phi \approx 70°$), whereas the minimum is reached at $\phi \approx 0°$ when the sliding direction follows the molecular rows (Figure 4.8 (b), right). The simulated TSM and FFM images in
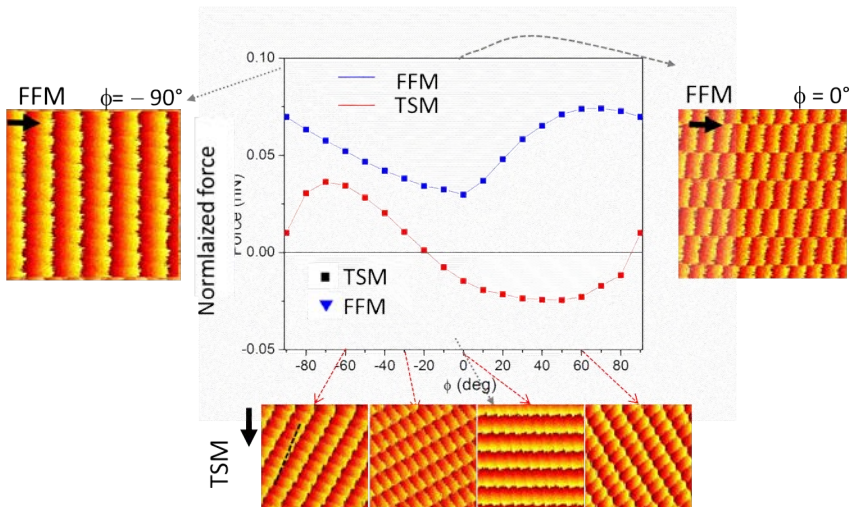
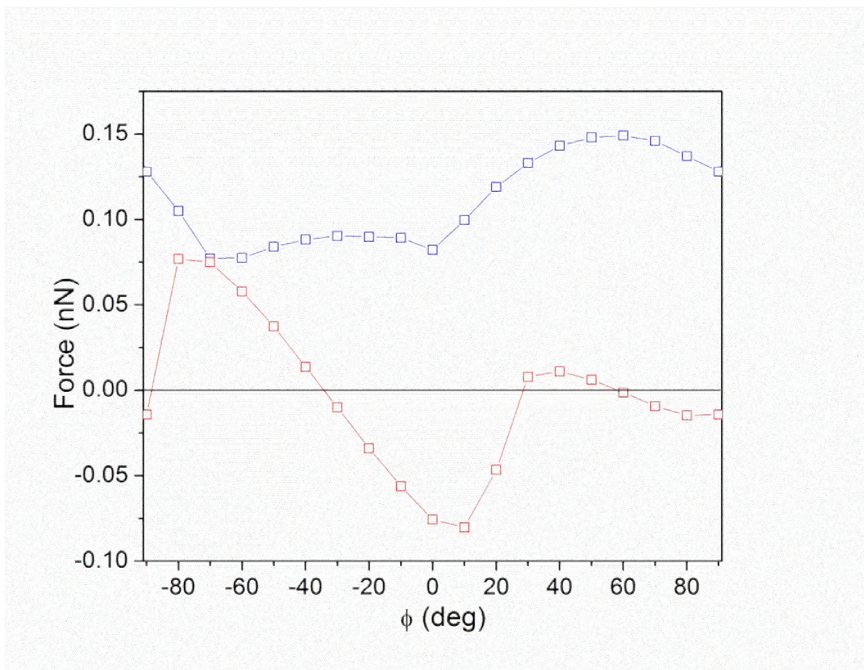**Fig. 4.9:** (a) Simulated FFM images corresponding to $\phi = 90°$ and $\phi = 0°$. (b) Angular dependence of the FFM signal (blue line) and of the TSM signal (red line) as estimated by solving the Langevin equation at T = 300 K with the interaction potential defined by equation 4.11 with $\frac{U_1}{U_0} = 0.2$. Simulated TSM images for specific angles are shown at the bottom.

Figure 4.9 reproduce the experimental images of Figure 4.7. It must be noted that when $\phi \approx 0°$, the frictional force remains finite, as in the experimental observations shown in Figure 4.7. In the simulated TSM lateral force, when $\phi = 90°$ the tip slides along the channels keeping a small constant (positive or negative) tilt in the y direction. In this case, the single molecules can be hardly identified in the minor corrugation appearing along the rows. Such corrugation becomes much more visible as ϕ is varied. Since the main crystallographic directions of the surface lattice are not perpendicular, the TSM images with the opposite sign ϕ are not specular.

At this point it is clear that the crystallographic aspects of the molecular surface are the direct cause of the FFM and TSM signals. However, the manifestation of anisotropy as clear contrasts in the FFM and TSM signal images will largely depend on the magnitude of the corrugation and on the temperature, as well as on the material itself.

In Figure 4.10 are shown three examples of other molecular crystals in which the molecules stand up in a nearly vertical configuration. While in DIP and C8-BTBT, the TSM signal shows no contrast within the islands, the azimuthal orientation of domains is distinguished for p-6P. It is also worth to stress the role played by the finite temperature (T).
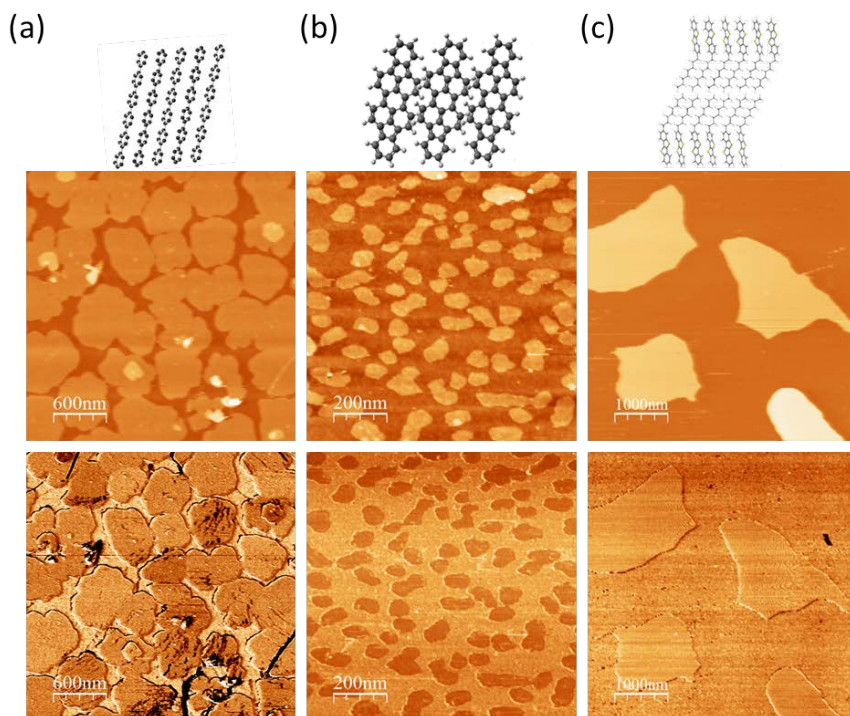
Fig. 4.10: Topography (first row) and TSM (second row) images of (a) para-sexiphenyl (p-6P), (b) diindenoperylene (DIP) and (C2,7-octyl[1]benzothieno[3,2–b][1]benzothiophene (C8-BTBT) submonolayers. Top: Side view of the crystalline structures.

In Figure 4.11, it can be observed how running the simulations at T = 0 changes dramatically the angle-dependence of the TSM and FFM signals due to metastable locations in the tip trajectory. As can be observed, this case is different from T = 300 K, when thermally activated slip stimulates the motion of the tip in the directions corresponding to lower energy barriers [129].

Fig. 4.11: Angular dependence of the FFM signal (blue line) and of the TSM signal (red line) as estimated by solving the equation of motion of the tip without thermal noise.

4.4 Load dependence of lateral forces

So far, all the measurements shown were performed at the minimum practicable load (explained in detail in Section 3.3.1), in the attractive regime, as close as possible to the pull-off force. The load-dependence of FFM and TSM signals was investigated for a particular PTCDI-C8 domain with an orientation of the molecular rows of $\phi \approx 45°$ with respect to the scan directions. The range of applied loads was chosen to assure the elastic regime of the contact, avoiding plastic deformation or damage of the molecular films. Figure 4.12 shows FFM and TSM signals as a function of the load. A linear load dependence is found in both cases, but the clearly lower slope for the TSM signal deserves attention. As illustrated in the profiles in Figure 4.12 (b), where the stick-slip behavior of the lateral force measured in FFM and TSM at two different loads are shown, the effect of the load is

also visible at the molecular scale. Whereas at the lowest practical load, the forward and backward paths nearly overlap for both signals, the area enclosed in the hysteresis loop of FFM importantly increases with the applied load, which is related to a larger energy dissipation. This is accompanied by an increase of the amplitude of the stick-slip response.

Differently to FFM, the effect of the load in the TSM profiles is notably lessened. Though both signals behave following a similar linear law, their different growth rate can be explained by the simulations. In order to do this, the effect of an increasing load is modeled through a constant variation of U_0, as schematized in Figure 4.12 (c). This is based on the linear relation between the corrugation of the surface potential and the maximum value of the stick-slip [130] and experimentally supported by the direct dependence of the lateral force with load. In Figure 4.12(d) are plotted the values for FFM and TSM signal as a function of U_0 (taking account for the increasing normal force) for $\phi = 45°$. It is observed that for this orientation of the PTCDI-C8 domain, the FFM signal is approximately three times larger than the absolute value of TSM. The proportion between the signals is maintained upon increasing U_0 as a consequence of increasing the normal load. Therefore, as in the experimental data, the simulated effect of the load is found to be similar for both TSM and FFM signals. This result points out that FFM and TSM are both components of the lateral force accompanying the stick-slip 2D motion of the tip at a molecular level. This refutes the physical interpretation attributing the TSM signal to elastic deformation of the surface [126] and indicates that the interaction potential at the contact interface represents the major physical properties accounting for the settlement of anisotropic frictional forces [123].
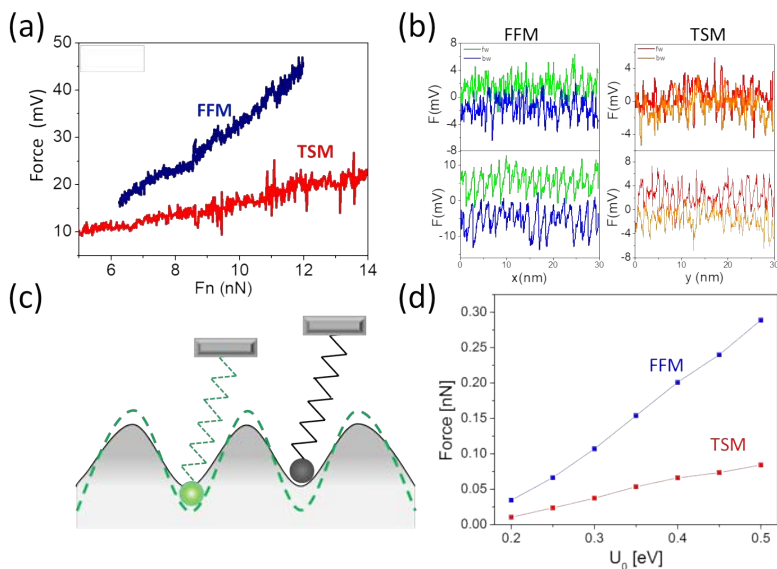
Fig. 4.12: (a) Load dependence of the lateral force signal (absolute value) for a domain oriented $\phi \approx 45°$. (b) Another data set showing FFM and TSM saw-tooth profiles measured at two different loads. Forward data are green or red in the corresponding profiles.(c) Scheme showing the increase of the corrugation height of the potential with increasing normal load. (d) Simulated load dependence of the FFM and TSM signals for a molecular domain oriented $\phi \approx 45°$.

4.5 Tip-induced 3D growth characterization.

AFM techniques have constituted a powerful approach for structuring surfaces at the nanometer scale. Among others, AFM and scanning probe litography (SPL) methods have been developed in the last decades including nanomanipulation [131], dip-pen nanolithography (DPN) [132], scratching [118, 133], nanografting [134], pressure induced restructuring [135, 136], electropeeling [137] or bias assisted electrostatic lithography [138], local oxidation [139], or local resistive state manipulation [140]. During this thesis, AFM was used to locally induce the crystalline growth of pentacene and PTCDI-C8 layers. As demonstrated along this chapter, PTCDI-C8 provides a large frictional

anisotropy surface structure that allows to investigate the crystallinity of the organic layers by FFM and TSM. This section was adapted from reference [101].

When scanning thin films of different organic molecules, a interesting phenomena was observed: without changing the tip load, part of the film was damaged in some areas while in others new molecular islands were formed upon successive scanning. An example of this is shown in Figure 4.13. 2,7− diocty [1] benzothieno [3,2−b] ben-zothiophene (C8−BTBT) is a small molecule widely used in organic electronics whose thin film reported structure consists of a layered herringbone packing with the lamellar planes parallel to the surface. The interplanar distance is reported to be 2.9 nm [141, 142].
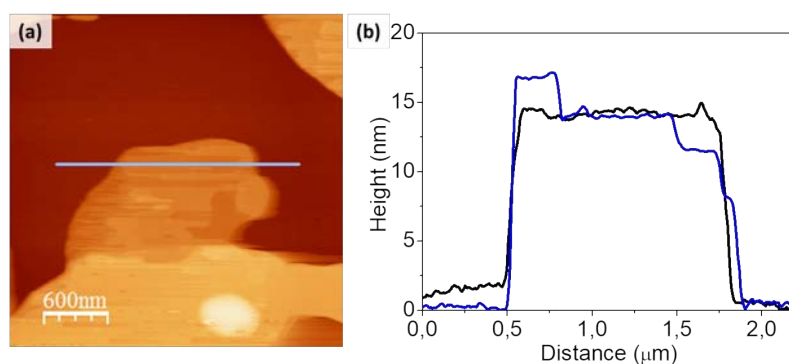
Fig. 4.13: (a) AFM topographic image of a C8-BTBT island after to the nanostructuration experiment obtained at the pull off force.(b) Profiles taken in the same spot as the marked in (a) for a first forward pass(black) and a third backward pass(blue).

Figure 4.13 (a) shows the topographic image as well as the profiles along the marked line in (b) taken in consecutive images with the same measurement conditions on a C8−BTBT film composed by 5 molecular layers. The measurements were made in the attractive regime. The molecules are removed upon measuring leading to an obvious change in the topmost layer. In the profiles in Figure 4.13 (b) we can observe how the molecular island, initially composed of

5 molecular layers (black profile), gets damaged in the right corner, leaving the 4th layer uncovered while a 6th layer starts growing in the left of the island (blue profile) demonstrating that, without changing the load, molecules are collected, dragged and reassembled forming a new layer level although not in a controlled nor previsible way, leading to a change of the surface in every scanned frame.

Similar experiments were performed in PTCDI-C8, due to its large frictional anisotropy which has allowed us to identify the azimuthal orientation of the molecular domains. In this work, the initial surface consisted in a three monolayers thick thin film deposited with OMBD with no bare substrate exposed at the surface. All the experiments, as the one presented on C8-BTBT, were made in the attractive regime because a slight load increase was observed to lead to an irreversibly damage of the molecular packing. For PTCDI-C8, the consecutive scanning also resulted in the nucleation and growth of new molecular layers on top of the initial surface film. This is exemplified in Figure 4.14 with representative frames illustrating the growth of islands up to the 6th layer.

As a reference for the morphological evolution, the same surface defect has been marked by arrows in all the images. Note that no bare SiO_2 exists and the lower level in the images corresponds to the second molecular layer. It seems that the growth process takes place by re-deposition of molecules close to the location from where they were removed. Thus, for instance, in Figure 4.14(b) molecules removed from the third layer and, therefore, leaving uncovered small areas of the second one (darker), are dragged by the tip and deposited at the top of the fourth layer. The subsequent growth of islands (5th and 6th levels) proceeded during the course of the experiment. As above mentioned, PTCDI-C8 films were considerably vulnerable under the sweeping effect of the tip and some of the formed islands with smallest size eventually vanished. This is the case of some tiny islands of the 6th level which are seen in Figure 4.14(d) but no longer appears in Figure 4.14(f). However, differently than in the C8-BTBT islands,
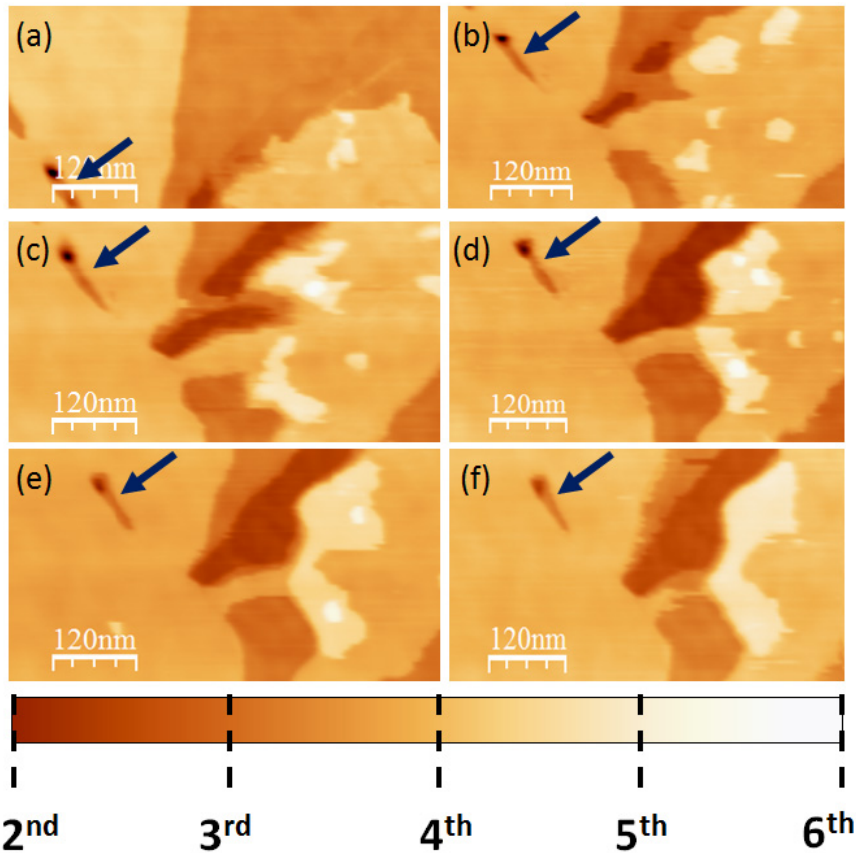
Fig. 4.14: Selected topographic images of a PTCDI-C8 tip-induced growth. (a-f) correspond to frames number 1, 4, 5, 8, 11 and 12 of a total of 12. The fragmented colour scale at the bottom indicates the height of each molecular layer ($\approx$2nm). Dark arrows indicate the same defect in all the images.

the tip induced grown islands mostly tend to remain upon further measurements.

Our observations imply molecular loading from the edges of inferior levels and incorporation at the terrace of nearby surfaces of the higher levels with no evidences of the opposite effect. The vicinity range of the process is illustrated in Figure 4.15 where two topographic AFM images before (a) and after (b) tip-induced modification are displayed. In this particular case, the formation of the 4th molecular layer occurs at expenses of the 3rd layer. This is reflected by an increase of the area of the pre-existing hole and an enlargement of
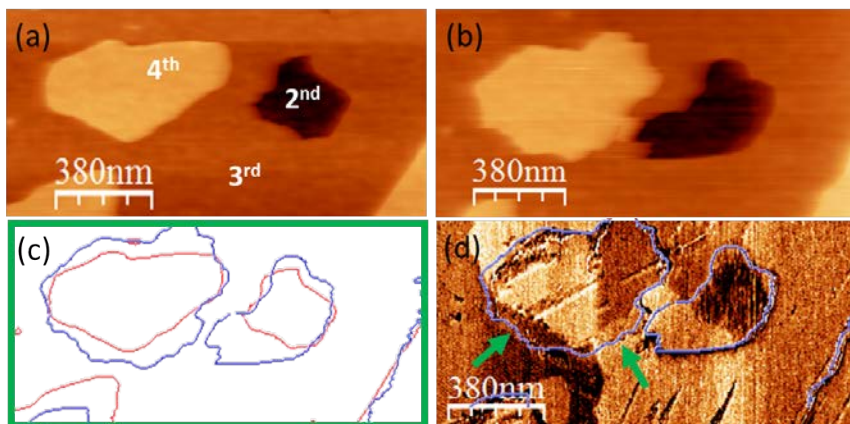
Fig. 4.15: Topographic images of the same area before (a) and after (b) modification of the PTCDI-C8 film. (c) Relief contour plot corresponding to (a) in red and (b) in blue. (d) The TSM image corresponding to the topography in (b).

the island size. To highlight these changes in topography, the relief contour outline for both images are merged in Figure 4.15 (c) (red and blue for (a) and (b), respectively). The friction anisotropy of PTCDI-C8 reflected in the TSM images allows inferring information on the crystallinity of the molecular layers and, particularly, whether the incorporated molecules adopt or not the azimuthal packing of the pre-existing island. The TSM image corresponding to the final stage of growth is shown in Figure 4.15 (d). As commented before, the TSM image reveals the domain boundaries between molecular domains with different azimuthal orientation. Comparison with the corresponding topographic contour superimposed to the TSM signal helps further interpretation. Note that a new region of the second layer has been uncovered after the modification revealing a grain boundary. In the PTCDI-C8 assembled at the border of the 4th level island marked by green arrows, the TSM signal replicates the signal of the underlying layer. Therefore, we can conclude that the molecules dragged and delivered by the tip on the surface reassemble in registry with the same molecular orientation of the layer underneath rather than following the molecular orientation of the island at which they laterally attach.

4.6 Conclusions

In the first part of this chapter, taking as benchmark sub-monolayer deposits of PTCDI-C8, we demonstrate that the lateral forces measured at a molecular scale in TSM mode arise, as in FFM, from the stick-slip response of the tip elastically driven over the periodic atomic surface potential. This result gives evidence of a dissipative origin of the TSM signal and provides understanding of the anisotropy of the observed contrast in relation with the surface structure symmetry. Lattice-resolved images acquired on top of differently oriented PTCDI-C8 molecular domains provide the azimuthal information without the need for sample rotation. By means of realistic simulations, we have shown how the Prandtl–Tomlinson model consistently explains the experimental FFM and TSM data at a molecular-scale. Furthermore, the occurrence and magnitude or the absence of TSM anisotropy observed for different molecular systems and/or domains can be simply explained.

The TSM has proven its capability to catch interesting structural features which are not revealed by conventional FFM alone. This has been applied to the study of ultrathin crystalline films grown by tip-assisted manipulation. By consecutively scanning the same area we are able to form higher crystalline layers in both C8-BTBT and PTCDI-C8 thin films. Taking advantage of the rich variety of contrasts that PTCDI-C8 films present when scanned by TSM, we have characterized the new areas crystalline orientation. Those new crystalline areas show similar TSM contrast and therefore are oriented in registry with respect to the underlying one. This result implies that the formed PTCDI-C8 assemblies replicate the in-plane orientation of the underlying film regardless of the orientation of the molecules in pre-existing islands to whose edges they are incorporated. As a consequence, though intra-layer domain boundaries may be created, a good 3D crystalline order is achieved. This seems to indicate that in this particular system, intra-layer domain boundaries are more energetically favoured, while the stacking fault energy is never overcome. The capability of inducing

the crystalline growth of molecular layers by AFM nanolithography could help on the nanostructuration of future organic nanodevices, i.e. OFETs with nanoscale channel lengths.

Energy level alignment in solar cells

<div style="text-align: right">5</div>

Contents

5.1   ITO work function modification by self-assembled monolayers and origin of s.shaped J-V curves

As detailed in Section 2.3.1, the basic structure of bulk heterojunction (BHJ) solar cells consists of a nanoscale blend with conjugated polymers acting as electron donors and fullerene derivatives as electron acceptors. This layer is sandwiched between a metal electrode and an indium tin oxide electrode. In a conventional forward solar

cell structure, the ITO layer acts as hole collection electrode. However, ITO does not perform well for such purpose due to its work function mismatch with the HOMO energy level of the polymer. Although ITO modification with SAMs allows low cost processing as well as chemical selectivity, the exploration of alternative hole-transport layers (HTLs) in BHJ systems to improve device performance has been limited in part due to the successful application of poly(3,4-ethylenedioxythiophene):poly(styrenesulfonate) (PEDOT:PSS) as HTL in a wide range of polymer OSCs.

Equivalently, in perovskite solar cells, an organic semiconductor hole transporting layer is required in order to achieve high energy conversion eficiencies. The spiro$-$OMeTAD $[2, 2', 7, 7'-$ tetrakis (N,N$'-$di$-$p$-$methoxyphenylamine) $-9, 9'-$ spirobifluorene] is the material of choice for most of the reported examples of triple cation mixed halide perovskite solar cells [143]. The inverted architecture is widely used, with the FTO / d$-$TiO$_2$ / CsFAMAPbIBr / HTL/Au structure, where FTO is fluorine doped tin oxide, d$-$TiO$_2$ is a dense layer of TiO$_2$ (40nm), and Au is the gold metal contact. As well as in organic photovoltaic devices, it is of great interest to develop novel HTLs for improving the devices efficiency as well as its stability.

In the following, two different studies will be detailed. In the first place, we will study the effect of SAMs as interlayer replacement of PEDOT:PSS in BHJ solar cells. In the second part of the chapter, we will address the impact of the deposition of two different organic HTLs on top of the perovskite on the final energy level alignment of the system, as well as in the interfacial carrier recombination kinetics of the final devices.

SAMs, already introduced in Section 2.1, have been proved to be effective interfacial modifiers modulating the surface properties of ITO, such as work function, surface energy, and electron-transfer kinetics that might lead to an enhancement in the efficiency and/or operational range of organic electronic devices. The advantages over other

electrode treatments are that the deposition, traditionally through immersion in a solution of the modifiers, is simple and allows for recycling of solutions. Furthermore, the diversity of terminal groups offers the possibility of choosing the functionalities needed for a given surface or application [41]. Phosphonic acid (PA), silanes and amines have been widely used to tune the surface properties in both multi-layer and bulk heterojunction OSCs and OLEDS [42–45, 144]. One of the main effects of dipolar SAMs is to modify the work function (ϕ) of the ITO in order to favour the energy level alignment between the electrodes and the active layer and herewith improving the OVP performance via an increase in the open-circuit voltage V_{OC}.

However, it has been seen that the device performance is not well correlated with the ITO ϕ modification [43, 47, 48]. For instance, Hotchkiss et al. use phosphonic acids in order to functionalize the ITO electrode of a bilayer Pentacene: C_{60} OSC by the fluorinated phosphonic acids [43]. Although an increase of the work function of ITO upon SAM modification by 0.9 eV was observed, the V_{OC} was found to be constant in all the investigated photovoltaic devices. In that work, this observation was attributed to Fermi level pinning effects between the ITO work function and the HOMO of the organic donor. Thus, it is yet clear that the role of the contact work junction is complicated by interfacial phenomena occurring between the electrode and the active layer.

Stubhan et al [145] while exploring phosphonic acid anchored aliphatic and fullerene funcionalized SAMs obtained J-V characteristics with a pronounced s.shape, as depicted in Figure 5.1(a), which was attributed to the insulating layer formed by the SAM. J–V characteristics with s.shape have been observed before and attributed to various effects, such as hindered charge transport through the active layer/electrode interface [147], charge accumulation [148], barriers due to interfacial dipoles, defects or traps [149] and phase segregation [150]. Wagenfahl et al. simulated the s.shaped current-voltage characteristics (depicted in Figure 5.1(b)) by introducing a reduced
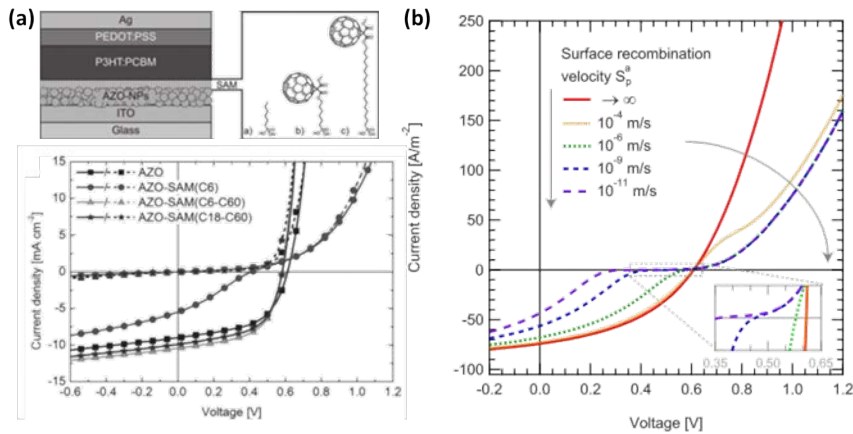
Fig. 5.1: (a)Device scheme and J−V characteristics of solar cells with AZO, AZO-SAM(C6), AZO-SAM(C6-C60) and AZO-SAM(C18-C60) modified ITO, extracted from reference [145]. (b) Simulated S.shaped J−V characteristics due to a reduced majority surface recombination velocity for holes at the hole conducting anode extracted from reference [146].

recombination velocity of majority carriers (holes in this case) [146]. If photogenerated charges are transported faster towards the interface than extracted, they will pile up creating a local space charge that modify the internal electric field and the energy levels in the bulk of the active layer, increasing the probability of recombination [146, 150]. The s.shape has been observed for interlayers with low transport properties [147, 151] and has also been discussed in terms of work function mismatch. Tress et al. simulated that an extraction barrier (due to misalignment between the HOMO and Fermi level of the electrode) can cause hindered extraction of photogenerated holes leading to the s.shape behavior [151]. Experimentally, similar s.shape effects have been reported for solar cells based of CuPc/C_{60} with ITO modified with C18-PA and P3HT:PCBM with C6-PA modified AZO, and attributed to recombination due to the insulating character of the alkyl chain and the low tunneling efficiency [145].

This extraction barrier can be also caused by a charge accumulation density leading to an electric field opposite to the charge extraction direction. This charge accumulation can be induced by intrinsic sur-
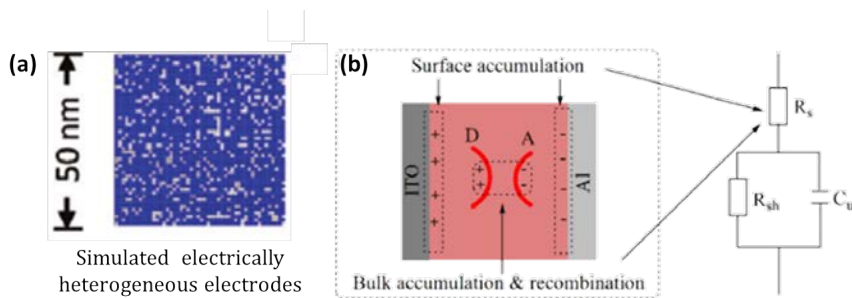
Fig. 5.2: (a) Schematic view of simulated electrically heterogeneous electrodes with the 20% of the area active for a random distrubution (extracted from reference [152]). (b) Schematic diagram to show bulk accumulation and recombination as well as surface accumulation at the organic/electrode interfaces and the modified circuit model of a solar cell extracted from reference [153].

face defects in the electrode/active layer interface that can function as interfacial traps and therefore as recombination centres [153]. These surface defects have been investigated by Zacher et al. by modelling the ITO electrode surface as a grid consisting of electrically active or inactive sites, the latter making a "blockage" effect (Figure 5.2(a)) [152]. It was concluded that the charge density at the ITO/active layer interface increases with the amount of "blocked" squares and the distance between them, due to a less accessibility of the electrical active sites. Moreover, for higher photocurrent generated inside the active layer, the inhomogeneity of the contact becomes more important and the charge density at the electrode/active layer interface increases. This fact leads to an electric field that enables charge extraction and increases recombination rates at that interface. The effects of this undesired opposite electric field would be observed in the J_{SC} and FF parameters of the devices. The study also reveals an advantage for very high charge mobility values, which would enlarge the characteristic diffusion lengths allowing the charges to reach the electrically conductive areas. Chen et al. also explore the effects of interfacial charge accumulation on the FF in OSCs [153] by performing capacitance measurements on un-annealed and annealed ITO/PEDOT/PBTTPD:PCBM/Al. An scheme of the charge distribution is shown in Figure 5.2(b). By increasing the illumination light inten-

sity, the FF of the annealed device continuously decreases, which can be attributed to both bulk and surface recombination. By performing capacitance vs voltage measurements (C−V), it was deduced that surface charge accumulation induced recombination dominates all the devices and strongly affects their FF of the IV characteristics, leading to s.shape effects in the J−V curves [148].

This section aims at understanding the effect of ITO functionalization by means of Phosphonic acid SAMs on the performance of OSC devices. The selected SAMs have been used before as ITO modifiers and induce a favourable change in the electrode work function [43, 66, 154].

5.1.1 Description of the active layer

Solution-processed organic solar cells have been fabricated with PBDTTT-CF as donor material and $PC_{71}BM$ as acceptor.
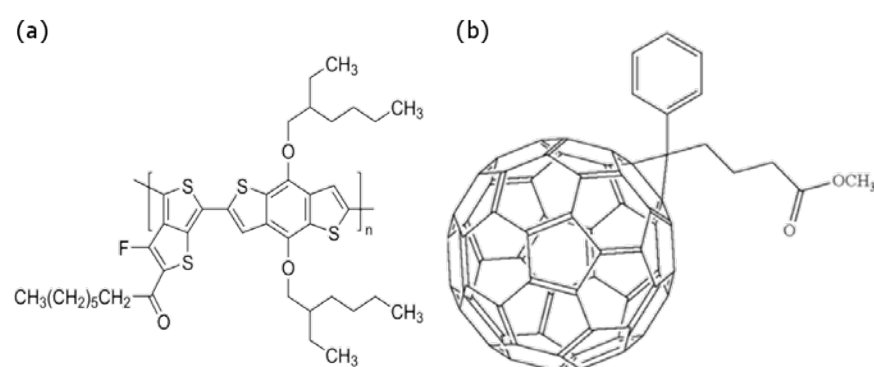
Fig. 5.3: Donor (a) PBDTTT-CF and acceptor (b) $PC_{71}BM$ materials used in solution process OSCs during this thesis.

Although poly(3−hexylthiophene) (P3HT) is currently the most widely used polymer in solution processed donor/acceptor blends in bulk heterojunction organic solar cells, a lot of interest is focused in synthesizing new polymers which fulfil the requirements for enhanced performance: (i) reduced bandgaps for larger light harvesting in order to increase short-circuit current (J_{SC}) and (ii) low HOMO polymer

level, for higher open circuit voltage (V_{OC}) values [155]. In particular, poly[4,8-bis-substituted-benzo [1,2-b:4,5-b0] dithiophene-2,6-diyl-alt-4-substituted-thieno [3, 4-b] thio-phene-2,6-diyl] (PBDTTT) derived polymers show an optimal bandgap of 1.6eV [156], as well as a desired energy level position of the HOMO, leading to J_{SC} higher than 15 mA cm^{-2} and V_{OC} around 0.6V. Chen et al. have enhanced the devices performance by replacing the alkyloxy group on the carbonyl of the thieno [3,4-b] thiophene unit with an alkyl side chain, which significantly increases the HOMO energy level. They have also added the high electron affinity atom fluorine, leading to the synthesis of poly [1-(6-{ 4,8-bis [(2-ethylhexyl) oxy[-6-methylbenzo [1,2-b:4,5-b] [dithiophen-2-yl}-3-fluoro-4-methylthieno [3,4-b] thiophen-2-yl)-1-octanone] (PBDTTT-CF) polymer. Devices based on this material blended with the fullerene derivative PC$_{71}$BM have shown V_{OC} values of 0.76V, J_{SC} currents higher than 15 mA cm^{-2} and a total efficiency of 7.73% [155]. The structure of this polymer is shown in Figure 5.3 (a).

PCBM derivatives are still the most commonly used n-type acceptor materials in organic semiconductor devices. Fullerenes (C$_{60}$ derivatives) are in the focus of research of acceptor materials because of several reasons: (i) low LUMO level, which leads to a very high electron affinity molecule, (ii) stability, (iii) ultrafast photoinduced charge transfer and (iv) very high electron mobility (up to 1 cm^{2}V^{-1}s^{-1}) [157]. PC$_{61}$BM preserves the electronic and physical properties of C$_{60}$ while LUMO is around 0.2 eV lower, and therefore the achieved V_{OC} and FF values are around 30% higher [158]. C$_{70}$ has an unsymmetrical structure with a significantly stronger absorption, which has resulted in the high performance fullerene PC$_{71}$BM. OSCs fabricated with PC$_{71}$BM have reported significant improvements in J_{SC} and V_{OC} values compared to PC$_{61}$BM [159, 160]. Although the solubility is not as good as with PC$_{61}$BM, devices fabricated with PC$_{71}$BM have shown to allow shorter annealing times and improved stability. The structure of PC$_{71}$BM is shown in Figure 5.3 (b) and the energy level scheme of the fabricated devices is depicted in 5.4.
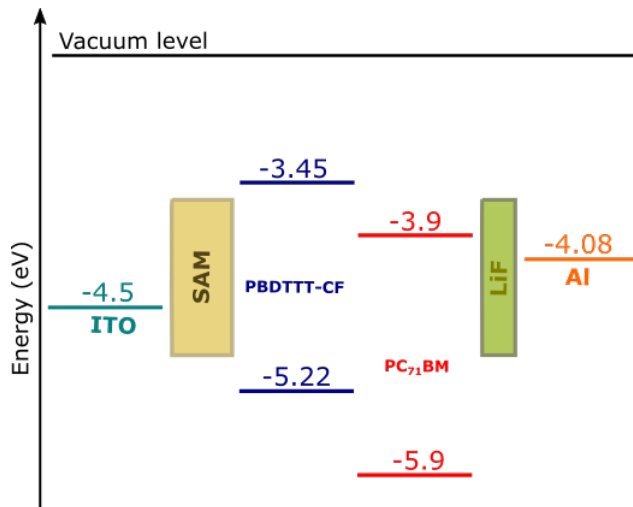
Fig. 5.4: Schematic energy level diagram of the studied devices.

5.1.2 SAMs impact on the devices

The two selected phosphonic acid were 3,3,4,4,5,5, 6,6,7,7,8,8,8−tridecafluoro octylphosphonic acid (FOPA) and 4-cyanophenyl phosphonic acid (CPPA) (Figure 5.5). They were selected as a case of study of the ITO functionalization, as both have a similar dipole that changes the ITO work function equivalently although their chemical termination has different properties.

In order to first study their influence on the ITO work function, two types of substrates were characterized by AFM: complete monolayers and patterned surfaces. The patterned surfaces, prepared with the μCP technique detailed in Section 3.1.2 allowed us to study the impact of the selected SAMs using non modified ITO as reference. Because the small SAM thickness (h≈ 0.6-1 nm) and the ITO surface roughness (rms≈ 0.51nm), areas covered by the SAM cannot be distinguished in the topographic image (Figure 5.5 (b)) but clearly observed in lateral force imaging (Figure 5.5 (c)), due to the lower friction experienced over the SAM. The patterend ITO surfaces were also employed to determine the relative CPD between regions with different functionality [161].
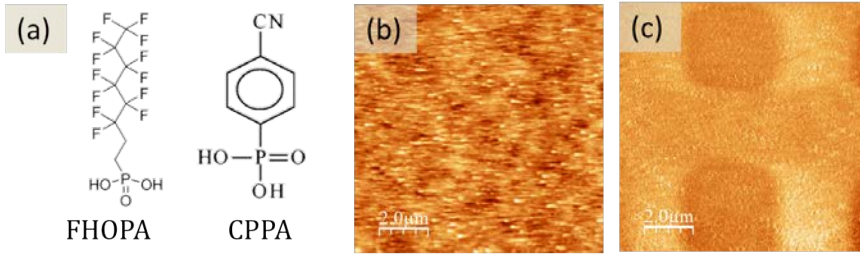
Fig. 5.5: (a) Scheme of FHOPA and CPPA molecules. Topographic (with height scale up to 1.9nm) (b) and lateral force (c) images of of a ITO substrate patterned with FHOPA.

Figure 5.6(a) shows the CPD map of an ITO substrate patterned by μCP with FHOPA functionalized regions (blue) surrounded by bare ITO (yellow). The resulting difference in work function between these two regions is of ≈ 0.6 eV. By immersion of this patterned substrate in a CPPA solution, FHOPA and CPPA terminated regions coexist on the same surface and their CPD can be directly compared. Thus, in Figure 5.6(b) the FHOPA functionalized ITO (dark blue) appears surrounded by CPPA functionalized ITO (dark yellow). The difference in CPD between them of ≈ 0.3 eV (profile in Figure 5.6(c)), proving that the CPPA functionalization also changes the ITO work function in the sense of decreasing the hole injection barrier.

As the ITO is functionalized with complete monolayers in the device, fully formed SAMs were studied. As can be observed in Figure 5.7, the morphology of the SAM-functionalized ITO is very similar to that
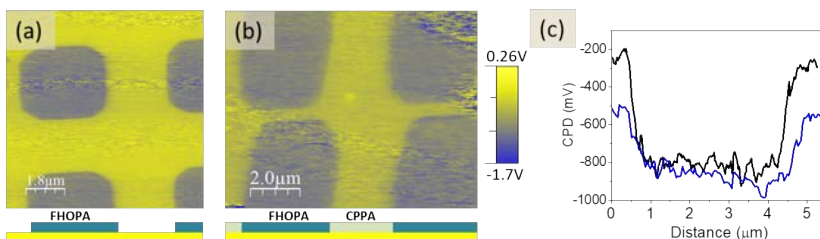
Fig. 5.6: CPD images of the patterned ITO surface with FHOPA (a) and FHOPA surrounded by CPPA(b) and (c) profiles taken along the marked lines.

of bare ITO indicating the formation of a complete monolayer over the whole surface. The quality of the SAMs was also checked by contact angle measurements (Figure 5.7 bottom). Contact angles were measured with 5ml water droplets on monolayers grown by overnight immersion. Bare ITO, cleaned by sonication cycles shows a contact angle value of 71.2°. When it is treated by UV ozone, as in the device fabrication process, the surface becomes more hydrophilic degrading in time [162]. CPPA functionalized shows a contact angle values of 50.2°, while a value of 108° is achieved when FHOPA is used due to its hydrophobic nature [154, 163].
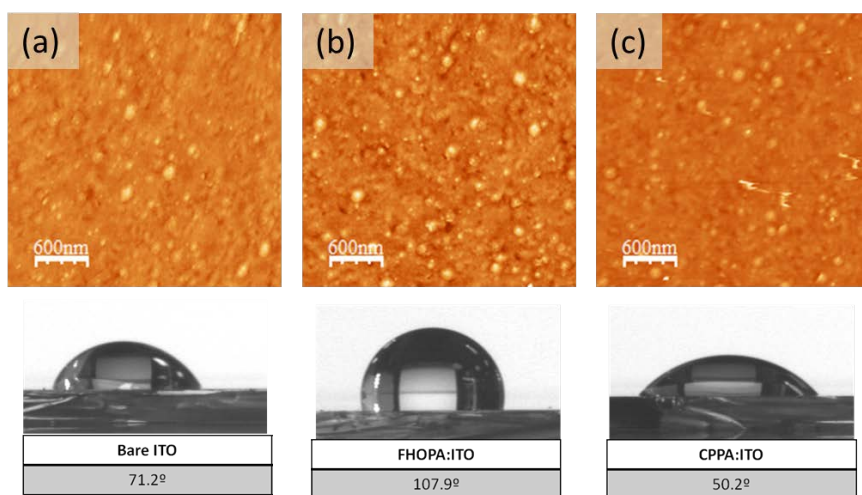
Fig. 5.7: Top: Topography images of (a) bare ITO, and a FHOPA (b) and CPPA (c) monolayers (SAMs) grown by immersion with a height up to 6nm. Bottom: Contact angle of bare, FHOPA and CPPA covered ITO substrates.

The influence of the fully formed monolayers on the substrate work function was evaluated from the Phase$-$V$_{\text{BIAS}}$ curves. Figure 5.8 (a) shows the Phase$-$V$_{\text{BIAS}}$ curves and the corresponding parabolic fit obtained for bare ITO, ITO/PEDOT:PSS and FHOPA and CPPA functionalized ITO. Up to 20 different locations at the surfaces were sampled to obtain an averaged value of the work function for each sample using a gold substrate ($\phi_{Au} = 4.9$ eV [164]) as a reference (Figure 5.8 (b)). It can be observed that the ITO functionalization with FHOPA and CPPA increases the overall work function from 4.5
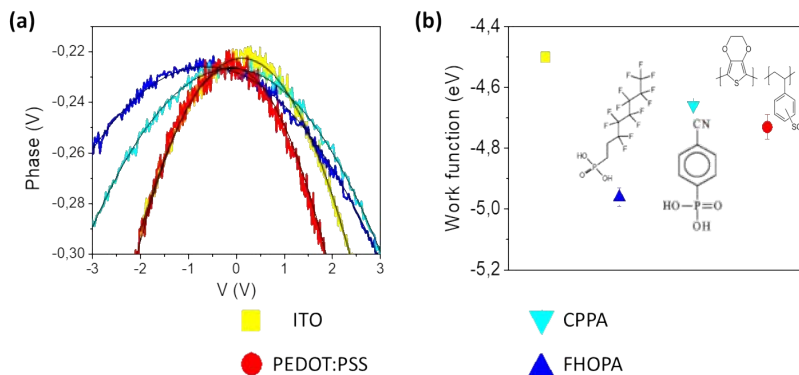
Fig. 5.8: (a)Phase$-$V$_{BIAS}$ curves performed in the functionalized ITO substrates and (b) the obtained work function values.

eV to a value of 4.9 and 4.7 eV, respectively, slightly lower than the values found in literature for these SAMs. Data for the PEDOT:PSS covered ITO also show the favourably role of PEDOT:PSS in increasing the work function (ϕ = 4.75 eV) in agreement with the literature [66, 154]. It has been reported that differences in CPD measured for the same SAM in patterned or soaked ITO may exist due to differences in molecular packing [161].

SAMs influence in the donor/acceptor blend

In addition to modify the work function, the alteration of the surface energy of ITO upon functionalization can potentially impact the formation and morphology of the active layer. To examine this possibility, the morphology and surface composition of blend PBDTTT-CF:PC$_{71}$BM films spin$-$coated on top of bare ITO, PEDOT:PSS and SAM functionalized ITO substrates were characterized by AFM, KPFM, c-AFM and XPS.

The topographic images shown in Figure 5.9 (a) and (b) look essentially identical, with a rms value of $\approx$ 1.7 nm (Figure 5.9 (c)),
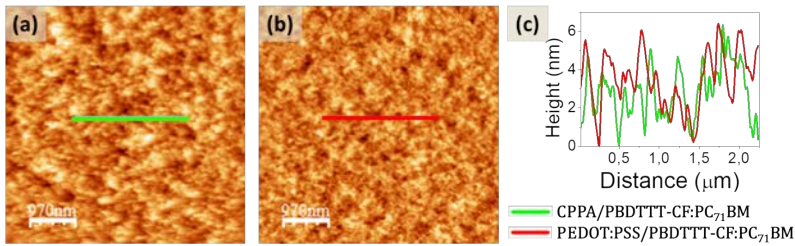
Fig. 5.9: Topographic AFM images of the active blend PBDTTT-CF:PC$_{71}$BM spin coated on top of a CPPA (a) and PEDOT (b) modified ITO substrates and (c) profiles taken along the marked lines.

indicating that the SAMs do not induce significant changes in the blend morphology.
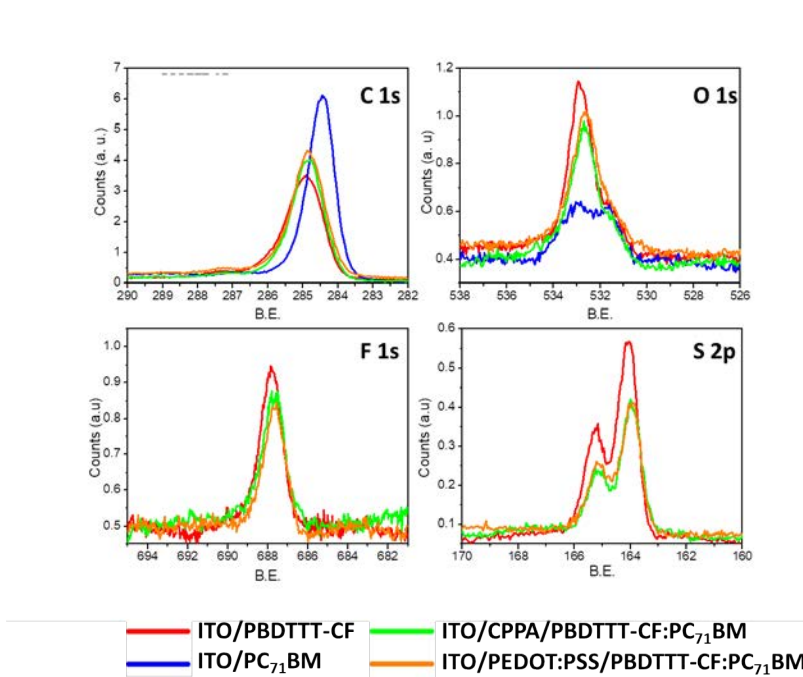
Fig. 5.10: C 1s, O 1s, F 1s and S 2p XPs peaks of blend PBDTTT-CF:PC71BM and PC$_{71}$BM spin coated on top of bare PEDOT and CPPA modified ITO substrates.

Plots of the XPS spectra of the blend on the two modified ITO surfaces, in particular the chemical information obtained from the 1Cs, 1Os, 1Fs and 2pS core-level are represented in Figure 5.10. Outstandingly, the

core levels of Fluor and Sulfur (elements only present in PBDTTT-CF) are significantly observed in both blend samples, indicating the presence of the polymer on the blend surface regardless of the substrate. Therefore, it can be concluded that the ITO functionalization with CPPA does not affect the interface between the active layer and the top Al electrode.

C-AFM was also used to explore the effect of the SAM on the I-V response in the PBDTTT-CF:PC$_{71}$BM active layers. To have an in-situ reference, the measurements were performed on PBDTTT-CF:PC$_{71}$BM layers spin-coated on FHOPA-patterned ITO substrates. The measurements were taken under dark and 1 sun illumination conditions with white light as described in Section 3.3.1.
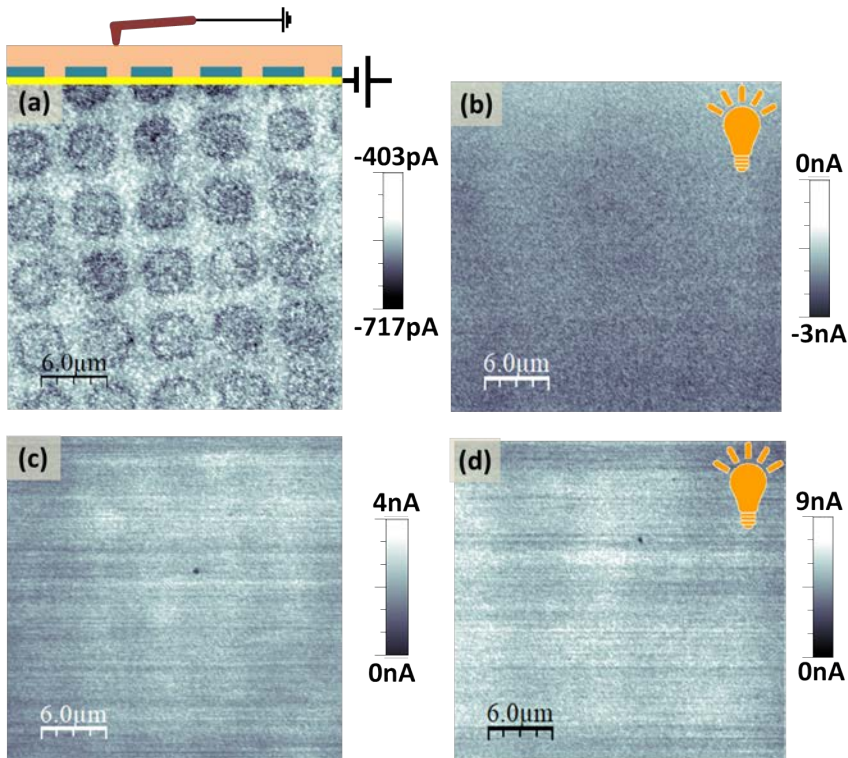
Fig. 5.11: Current images of a 100nm thick PBDTTT-CF:PC$_{71}$BM layer spin coated on top of a FHOPA patterned ITO substrate taken in dark conditions (a) and (c) under illumination (b) and (d) for a 2V ((a), (b)) and -2V ((c),(d)) bias applied to the sample.

This method allows the measurement of the nanoscopic electrical photoresponse of the blends as a complete device in which the cathode role is played by the metallic tip. Figure 5.11 shows the current map acquired in dark conditions (a) with the sample biased at 2 V and the tip grounded. At these conditions, holes are injected from the ITO electrode into the active layer and collected at the tip (see Section 3.3.1). The results in dark reveal a higher extracted current for the blend on top of FHOPA-patterned areas (dark squares). This agrees with the lower hole injection barrier for functionalized ITO due to the local increased work function induced by the SAM. When the sample is illuminated, the photocurrent extraction is enhanced globally and the squares pattern becomes indistinguishable (Figure 5.11 (b)). When the sample is biased with -2V, in dark conditions (Figure 5.11 (c)) or under illumination (Figure 5.11 (d)) the pattern is only faintly distinguished in the current images. This is explained by the absence of energy barrier for hole extraction through the ITO electrode. Therefore, the presence of the patterned SAM, when using the tip as top electrode, is not having any impact in the charge collection. The only difference between the current maps collected in dark conditions or under illumination is an overall increase of the photocurrent when the sample is illuminated.

Device characterization and modelization

Bulk heterojunctions organic solar cells were fabricated by spin coating a 1:1.5 solution of PBDTTT-CF:PC$_{71}$BM [155] with architecture glass/ITO/interlayer/PBDTTT-CF:PC$_{71}$BM /LiF/Al using three interlayers, namely PEDOT:PSS, FHOPA and CPPA.

Figure 5.12 shows the J-V characteristics under 1 sun (a) and in dark (b). It can be observed that the J-V curves in light for FHOPA and CPPA functionalized ITO present a strong s.shape in the fourth quadrant. As corroborated in Table 5.1, this kink emerging near the open circuit voltage in the J-V characteristic of illuminated organic
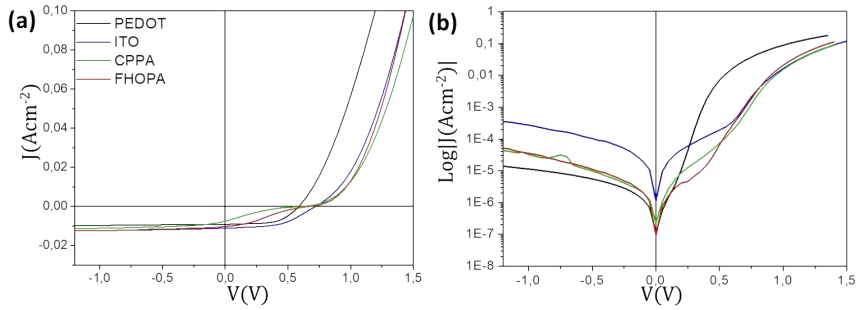
Fig. 5.12: J-V characteristics of the fabricated devices under illumination (a) and in dark (b) conditions. Linear and logaritmic representations are used respectively.

	$R_S/A(\Omega cm^{-2})$	$J_{SC}\ (mAcm^{-2})$	FF(%)
PEDOT	0.26	-15.1	64.0
ITO	0.24	-11.1	51.1
CPPA	0.21	-9.1	34.9
FHOPA	0.27	-9.6	22.6

Tab. 5.1: R_S, J_{SC} and FF parameters of the best fabricated devices with the different SAMs. The R_S values are obtained in the bias range 1.2-1.5V

solar cells has detrimental consequences on the fill factor (FF) of the devices. The current in the forward direction is little affected upon functionalization, presenting only a shift in the turn-on voltage, and series resistance (R_S) with no significant change from that of the ITO devices.
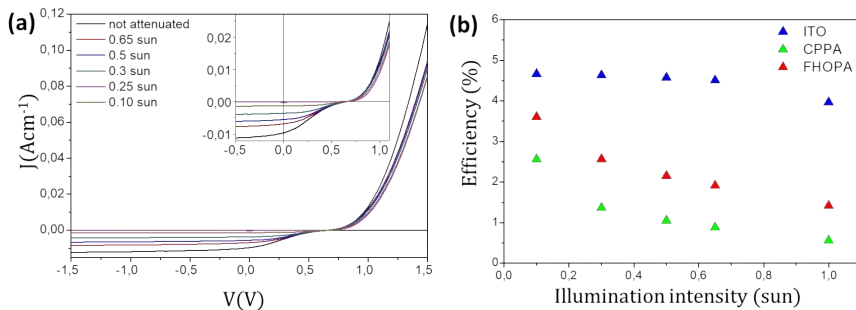
Fig. 5.13: (a)J-V characteristics of FHOPA:ITO devices under different illumination intensities and (b) efficiency vs illumination intensity.

In order to further understand the factors causing the arise of the s.shape, the devices where measured under different intensities from 0.1 to 1 sun under AM1.5 illumination in inert atmosphere. Figure 5.13 (a) the J-V characteristics of FHOPA:ITO devices under different illumination intensities are plotted. The values extracted of the efficiency are represented in Figure 5.13 (b) as a function of the light intensity. It is noticeable how, while the efficiency barely changes for the ITO devices, in the SAM functionalized ones it decreases with increasing illumination intensity. This increase in the efficiency seems to be due to a reduction of the s.shape at lower illumination intensities i.e. for lower photogenerated carrier concentrations.
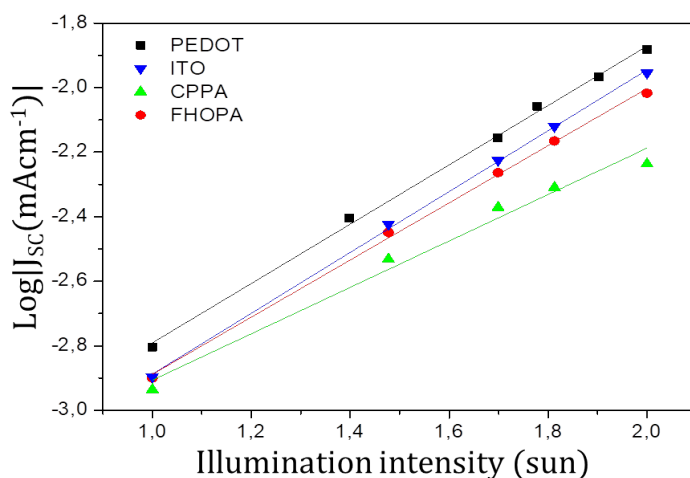
Fig. 5.14: J_{SC} vs illumination intensity extracted from the curves in Figure 5.13 (a)

In Figure 5.14, J_{SC} of the devices are plotted on a log scale and fitted to a power law $I \propto I^{\alpha}$, where values of $\alpha < 1$ are frequently attributed to bimolecular recombination [165] while values of $\alpha \approx 1$ are related to molecular recombination [166, 167]. Molecular or geminate recombination occurs before polarons dissociation while bimolecular refers to the recombination of an electron and a hole that have been photogenerated. The best fits yield $\alpha_{\text{PEDOT}} \approx 0.9$, $\alpha_{\text{CPPA}} \approx 0.7$ and $\alpha_{\text{FHOPA}} \approx 0.8$, indicating a larger bimolecular recombination in the

SAM functionalized devices. Although it cannot be attributed directly to an interfacial phenomena, it is evident that the use of SAMs instead of PEDOT:PSS as HTL causes additional bimolecular recombination in the devices.

Thereby, although the functionalization of ITO by the selected PA SAMs leads to a beneficial increase of work function, the J−V characteristics point to significant extraction problems. The widely used equivalent circuit solar cell model, which represents the solar cell J−V behavior by a photocurrent source, a diode that takes into account the dark current, a series resistor and a shunt resistor, cannot simulate the s.shape of the curves. Instead, the s.shaped curves can be modeled by a three−diode circuit with exact analytical solutions, as the one schematized in Figure 5.15 [168]. The details of the following description can be found in the publication from Romero et al. included in the frame of this thesis [169].
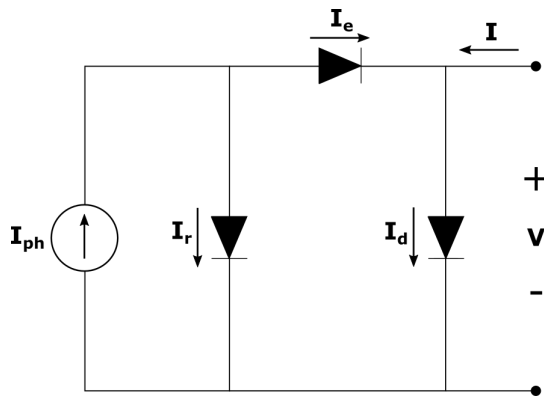
Fig. 5.15: Scheme of Mazhari's model [168].

In the absence of parasitic series and shunt resistances the model includes two extra diodes: a recombination diode that models recombination and an extraction diode that models the extraction of free carriers. These two extra diodes only operate in forward conditions under illumination, so they don't have any impact in the dark I-V

characteristics of the cell. Therefore, the total current (I) flowing through the circuit will be:

$$I = I_d - I_e = I_d + I_r - I_{ph} \tag{5.1}$$

where I_{ph} is the photogenerated current, and I_d, I_r and I_e, are the current flowing through the dark, recombination and extraction diodes respectively (Figure 5.15). Each one of these diode currents are described by the standard equation of a diode:

$$I = I_0(e^{nV} - 1) \tag{5.2}$$

where I_0 is the reverse saturation current and $n = q/(\nu K_B T)$, where ν is the diode ideality factor, K_B the Boltzmann's constant and T the absolute temperature. I−V curves can be simulated varying the values of ν and I_0 for each diode, while the other parameters remain constant.
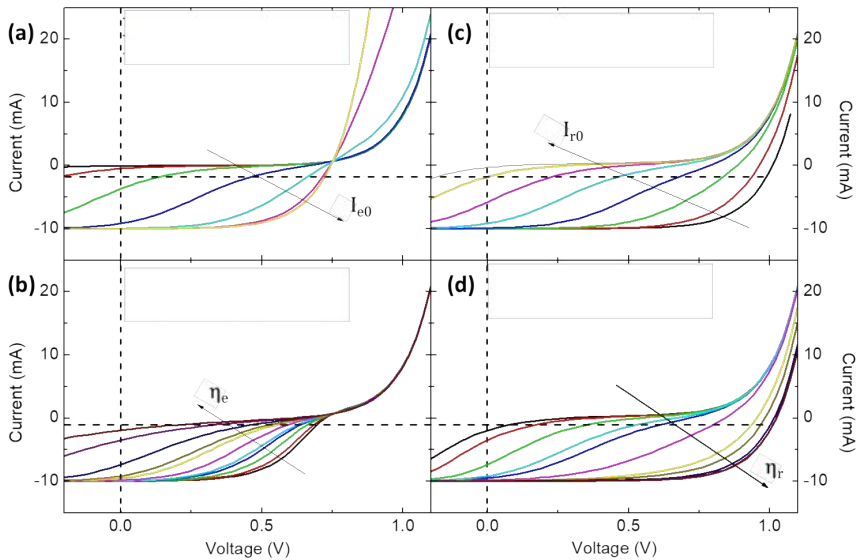
Fig. 5.16: Simulated I-V characteristics for several values of four model parameters: I_{e0} (a), I_{r0} (b), ν_r (c) and ν_e (d). Default parameters are $I_{e0} = 4\text{x}10\text{-}4$ A, $I_{r0} = 7\text{x}10^{-6}$ A, $\nu_e = 6$, $\nu_r = 4$, $I_{ph} = 10$ mA

Figure 5.16 shows the impact of the of varying the described parameters. These results indicate that, upon decreasing the ideality factor of the extraction (ν_e) diode and increasing the one of the recombination (ν_r) diode, the s.shape kink location is shifted towards higher voltage values. Similarly, increasing the reverse saturation current of the extraction diode (I_{e0}) or decreasing the recombination value one (I_{r0}) also shifts the location of the kink toward higher voltage values. This confirms that the s.shape kink tends to vanish when the current flowing through the recombination diode decreases and becomes negligible compared to the current flowing through the extraction diode. This can be achieved by either increasing ν_r or decreasing I_{r0}. As a first step of the modelization, the dark I−V characteristics are
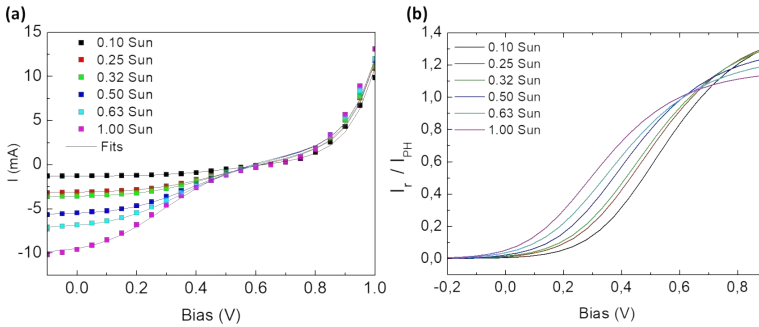
Fig. 5.17: (a)Experimental J-V data for different illumination intensities and the respective fits of a FHOPA functionalized ITO deviced and (b) normalized current flowing through the recombination diode (I_r) vs applied bias for the same illumination conditions.

fitted to obtain the reverse saturation current and the ideality factors of the diodes and afterwards these are kept constant to fit the I−V characteristics under illumination. Figure 5.17(a) shows the excellent agreement between experimental data and the corresponding fits. In Figure 5.17(b) the current through the recombination diode (I_r) normalized to the maximum photocurrent (I_{ph}) is plotted for different illumination intensities. We can observe that for higher illumination intensities, the current through the recombination diode is higher for voltages below V_{OC}, implying that the current through the recombination diode becomes dominant. Photocurrent can only be extracted upon applying a reverse bias which is larger for higher illumination

intensity. Note that for 1 Sun illumination, the recombination is 100% when the voltage is close to V_{OC}.

In this work, the recombination responsible for the s.shape kink does not occur for bare ITO or when ITO is covered with PEDOT:PSS. Thus, it seems to be caused by the properties of the ITO/SAM interface. The fact that the recombination current becomes higher at larger illumination intensities correlates well with the hindered hole extraction at the anode interface.

Electrical characterization at the nanoscale

Since the anode interface seems to play a critical role on the charge extraction dynamics, the influence of the SAMs was also investigated by analyzing the surface conducting response with C-AFM (detailed in Section 3.3.1). We note that though in all C-AFM experiments the current is measured, it depends on the contact area, which varies from tip to tip and depends as well on topographic aspects of the surface and the applied force. For this reason, slightly different current values may be obtained for the same voltage as a result of differences in the set points used for the image acquisitions. The way to overcome the current and resistance dependence on contact area is performing comparative analysis from measurements made using the same tip. In order to have accurate characterization of the SAM-functionalized ITO, C-AFM measurements were performed on patterned substrates. Figure 5.18 shows the current image of a bare ITO substrate, revealing very inhomogeneous conduction at length scales of 20nm, with sites of very different resistances. This is manifested in the current histogram in Figure 5.18 (b), in which we can observe that, although some highly conductive spots (of ≈3.8 nA) are found, most of the current values are 0 nA or slightly above 0 nA. Such lateral electrical inhomogeneity of the ITO surface has been already reported [154, 162, 163] although its implications for the overall device efficiency have not been systematically analysed [170–172].
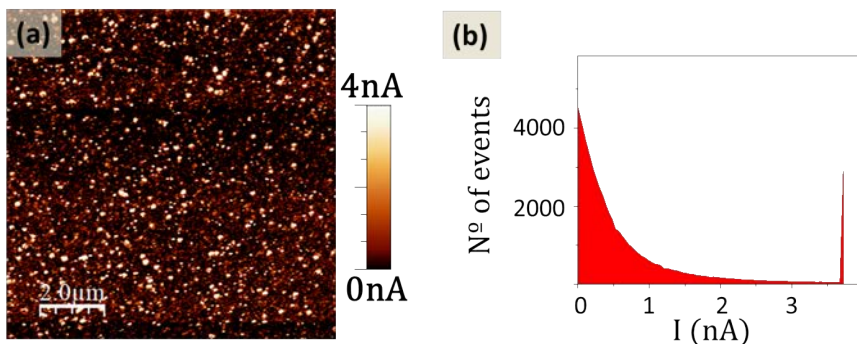
Fig. 5.18: (a) Current images of a bare ITO substrate with the tip biased at 2V and (b) current histogram of the image in (a).
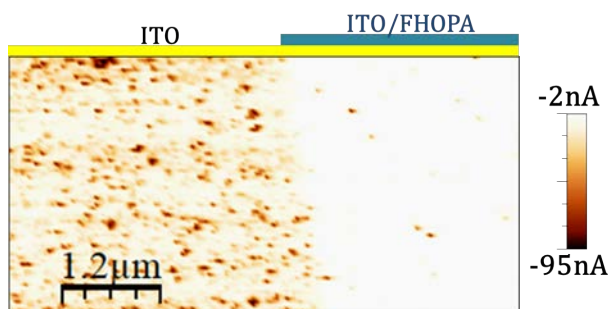

Fig. 5.19: (a) Current images of a FHOPA patterned ITO substrate taken at -3V.

Figure 5.19 shows the current images of an ITO sample patterned with $3\mu m$ stripes of FHOPA by μCP. Although the whole image shows an important electrical inhomogeneity, we note that two different areas clearly identified. As can be observed in the functionalized areas, the FHOPA functionalized surface shows reduced current at the same applied voltages (a behaviour also observed for CPPA).

A similar study was made on a PEDOT:PSS layer spin coated on ITO (Figure 5.20). In this case, the conductivity improves, the current is overall increasea even at lower voltages. In the histogram plotted in Figure 5.20 (b) this behaviour is manifested in higher current (less resistance) as well as in larger electrically conductive areas.
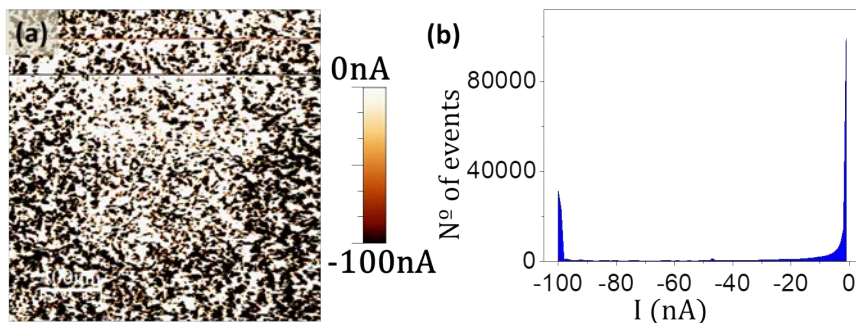
Fig. 5.20: Current images of a PEDOT:PSS covered ITO substrate taken at -2V and (a) current histogram of the images (b).

In Figure 5.21 are shown the I-V curves taken with the AFM tip in the different samples. For bare ITO, curves taken in the conductive sites show a ohmic behaviour with low resistances of $\approx 0.2M\Omega$ (black curve in Figure 5.21 (a)). Differently, curves taken in the non conductive areas show how the current is only extracted at higher applied voltage bias as seen in the grey I-V curve depicted in Figure 5.21(a). These non conductive areas show a resistance varying in more than 3 orders of magnitude. The I-V curves taken on the functionalized areas exhibit a behaviour typical of tunnelling through the SAMs. Even the IV curves taken in the conductive spots (black curves) show much higher resistances than in ITO ($\approx 600M\Omega$). .

From the image and IVs analysis, it seems that the SAM impedes the charge (electrons) extraction through the electrode, increasing the contact resistance. SAM-functionalized ITO exhibits rather inho-
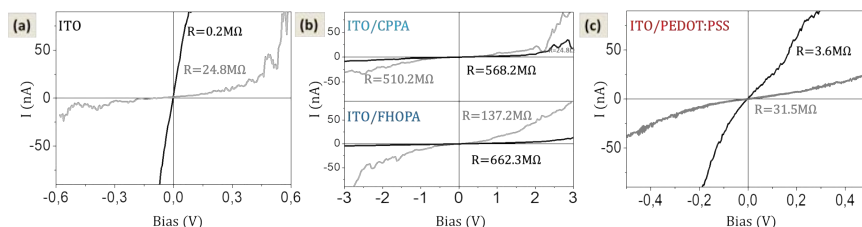
Fig. 5.21: I-V curves taken in bare (a), SAM functionalized ITO (b) and a PEDOT:PSS layer spin coated in ITO (c).

mogeneous current pathways and distribution of conducting spots. PEDOT:PSS layer however, induces a higher homogeneity in both conductivity magnitude and density of conducting spots (Figure 5.20(a)). The IV curves taken all over the sample surface (depicted in Figure 5.21(c)) reveal the well-known space charge limited current of the PEDOT:PSS covered electrodes [167, 173], with an ohmic behaviour at low voltages and a quadratic dependence of the current at higher voltages.

In spite of the increase in the work function of the ITO covered with the SAM, tour conductivity studies conclude that the SAMs result in an increase of the contact resistance while leaving large areas of electrically inactive surface (as for the bare ITO).

The role of the electrical heterogeneity

So far, it seems that the interfacial recombination at the cathode/active layer interface is significantly increased for the SAM functionalized ITO devices (Figure 5.17(b)). The result of this phenomena is the strong s.shape in the J-V characteristic. Moreover, the plot of I_{SC} vs illumination intensities (Figure 5.14 (b)) indicates that the use of the functionalized ITO substrates induces an increase of the bimolecular recombination.

We suggest that this no-radiative recombination is assisted by structural defects like the charge accumulation caused by the "blocked" sites in the interface, observed by c-AFM (Figure 5.19) for the bare ITO and the SAM functionalized ITO. Taking into account that this phenomena is not present in the PEDOT:PSS devices, we conclude that an important amount of recombination is taking place at the anode that can be attributed to charge density accumulation due to the electrically blocked areas in the ITO functionalized interface.

As introduced before, the role of the electrode heterogeneity on the device performances has been subject of recent discussion. In the case of the studied functionalized ITO substrates, although the beneficial worfunction change, the SAMs would act as a blocking layer inducing more accumulated charge density than in the case of the non functionalized ITO, impeding a good performance in the fabricated devices. In fact, the electrode conduction inhomogeneity is more pronounced in the bare and SAM functionalized ITO cells, leading to a interfacial electric field that would play an important role reducing extraction in this electrode and thereby higher V_{BIAS} values must be applied to extract charge (Figure 5.17(b)). The s.shape evanescence with lower illumination intensities (Figure 5.14 (a)) also correlates with the advent of this charge accumulation, as less charges are photogenerated.

5.1.3 Conclusions

It has been proven that phosphonic acids SAMS modify the ITO work as expected, forming homogeneous monolayers as evidenced from KPFM and contact angle measurements. The more beneficial energy level alignment in ITO/modifier/PBDTTT-CF:PC$_{71}$BM was also confirmed through conductive AFM measurements of the active layer casted on top of SAM patterned substrates. However, the fabricated devices present strong extraction problems, with a significant s.shape J-V curves in the third quadrant for the bare and functionalized ITO devices. An insightful study of the interface ITO:modifier performed by c-AFM has revealed a very inhomogeneous lateral conductivity in the bare ITO substrates, with an importantly increase of the resistance in the SAM functionalized ITO surface in contrast with the more homogeneous and better conductive PEDOT:PSS layer casted on top of the ITO. This inhomogeneous conductivity was observed and modelled before and leads to a surface charge accumulation on the ITO-modifier/active layer interface. In this work, the resulting s-shaped J-V curves of the fabricated devices are attributed to this charge accumulation, as they induce an electric field that impedes

the hole extraction in the ITO-modifier electrode. Through a further analysis of the J−V characteristics with the Mazhari model, it has been proven that at higher illumination intensities the current through the recombination diode becomes more relevant while at lower illumination intensities it becomes negligible compared to the extraction current. This fact supports the hypothesis of a charge accumulation density at the anode that would be responsible for the s.shape kink in the characteristic curves.

It can be concluded that, although the beneficial work function change, the studied SAMs do not fulfil the requirements for becoming efficient HTL in high efficient OSCs.

5.2 Evidence of HOMO-LUMO Energy Shift for Hole Transport Material in Perovskite Solar Cells.

5.2.1 Motivation

As introduced before, the highest efficiencies in perovskite solar cells have been achieved with the inverted architecture FTO / d−TiO$_2$ / CsFAMAPbIBr / HTL/Au [174]. The HTL seems to play a crucial role in the hole transport and extraction, as well as in the interfacial charge recombination [175]. In brief, a good hole transport material should have an HOMO level above the perovskite valence band, high hole conductivity,stability and finally high solubility in organic solvents [176]. The route to design HTLs is tuning the ionization potential (IP) or position of the Highest Occupied Molecular Orbital (HOMO) level in order to maximize the open circuit voltage (V$_{OC}$). However, as happens in OSC, a more favourable HOMO position is not clearly related to a better performance of the devices [177–179].

The most common used material nowadays is 2,2',7,7'-tetrakis(N,N'-di-p-methoxyphenylamine)-9,9'-spirobifluorene] (spiro-OMeTAD) [143], whose energy levels are compatible with the perovskite ones and leads to high performances [143, 180]. However, due to its complex synthesis, instability and high cost, a great interest is devoted to developing novel materials that could substitute it.

In this work, we focus in the impact of two different HTLs in the performance of CsFAMAPbIBr solar cells with the previously intro-duced structure. The two HTLs present close chemical and physical properties: the well known spiro-OMeTAD and the recently reported etra4-[N,N- (4,4-dimethoxydiphenylamino)]phenyl ethene (TAE-1) [181], which has a slightly deeper HOMO level in comparison with spiro-OMeTAD, as depicted in Figure 5.22. The HOMO and LUMO given values are determined by theoretical calculations and measure-ments of the oxidation potential by cyclic voltammetry presented in previous communications [181]. The goal in this work is to get insight
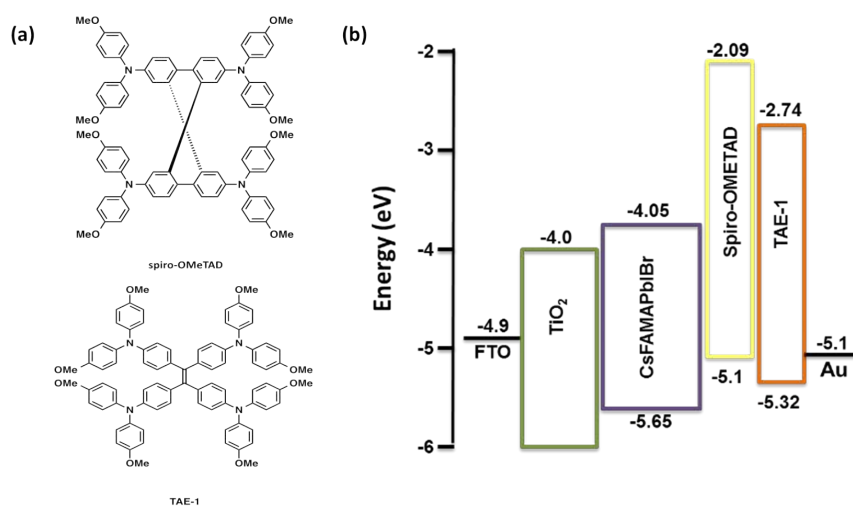
Fig. 5.22: (a) Molecular structures of spiro-OMeTAD and TAE-1 and (b) energy diagram for the of materials studied in this work. The HOMO and LUMO values of TAE-1 and Spiro-OMeTAD have been determined by electro-chemical analysis.

in the origin of the differences in V_{OC} in devices using the mentioned HTMs. This work was made in collaboration with Dr. Emilio Palomares

group, which synthesized TAE-1, fabricated the devices and performed the electrical characterization as well as the theoretical experiments. My contribution to this work has been the work function determination of the HTMs when casted on top of FTO/d-TiO2CsFAMAPbIBr and FTO/d-TiO2.

5.2.2 Experimental: work function measurements

In this work, we employed KPFM to evaluate the contact potential difference (CPD) between the metallic tip and the sample. The relationship between the contact potential difference and the work function of the tip and sample was described in Section 3.3.1. Due to this CPD, an electrostatic force is developed which obeys Coulombs's law as explained in Section 3.3.1. As shows equation 3.1, this electrostatic force has a parabolic dependence with the tip-sample bias voltage. As the frequency or phase shift of the oscillating probe is proportional to the force gradient, they will also present the same dependence. Therefore, the CPD of the different samples was extracted from the direct measurement of the frequency shift versus applied bias (as in equation 3.14).

Knowing the work function of the tip (ϕ_{tip}), the work function of the sample (ϕ_{sample}) can be calculated from equation 3.7. However, the tip work function is susceptible of changing during the measurement, due to its interaction with the sample. Therefore, the gold electrodes deposited on top of each surface layer were used as reference, allowing a reliable comparison between different samples. We used the value of ϕ_{Au} = 4.9 eV [182]:

$$\Delta\phi = \phi_{sample} - \phi_{Au} = e[V_{CPD}(sample) - V_{CPD}(Au))] \qquad (5.3)$$

The protocol of the measurement consisted on taking alternate CPD curves in the central area of the sample, and in one of the gold grounded electrodes. This was repeated in the same sample at least

twice, checking in every occasion that the CPD in the gold remained unchanged. Moreover, in order to assure the reliability of the method, diverse locations were evaluated and several curves were obtained at each position. When changing between samples, CPDs in the gold electrode were first taken in order to assure the state of the tip and therefore the reproducibility of the measurements. The error in the measurement was estimated as the standard deviation of the mean: $SDO = \pm\sigma/\sqrt{n}$ where σ is the standard deviation of the data and n is the number of data values.

5.2.3 Devices characterization and work function determination

The devices were characterized, and the solar cell parameters are shown in Table 5.2: From these parameters, it must be noted that

Device	J_{SC} $(mAcm^{-2})$	V_{OC}(V)	FF(%)	PCE(%)
spiro-OMeTAD	22.6	1.08	0.76	16.7
TAE-1	20.2	1.02	0.70	14.3

Tab. 5.2: Solar cell parameter for spiro-OMeTAD and TAE-1 devices.

V_{OC} is larger in spiro-OMeTAD. This behaviour is the contrary as the expected one, considering that TAE-1 has a deeper HOMO energy level than spiro-OMeTAD (Figure 5.22(b)).

Time resolved spectroscopy experiments were carried out, revealing that both devices with spiro-OMeTAD and TAE-1 as HTM present the same carriers recombination kinetics and, therefore, the same interfacial carrier recombination. Thus, the differences in V_{OC} for the two HTMs must arise from a difference in the energy offsets at each HTM/perovskite interface.

In order to understand the interfacial effects in the energy alignment, the work function of the different layers was estimated from the CPD measurements, including control samples consisting of the HTL layers deposited on d-TiO$_2$ and the bare perovskite. For these control samples, the measured work function was 4.86 ± 0.08 eV for TAE-1/TiO$_2$, 4.91 ± 0.08 eV for spiro-OMeTAD/TiO$_2$. It must be noted that these values correspond to the effective work function of the HTM/TiO$_2$ system, and therefore may differ from the values extracted from cyclic voltammetry shown in Figure 5.22(b).

When the HTMs are spin-coated on top of the CsFAMAPIBr layer, the ϕ values of the system change remarkably respect to the bare perovskite sample, resulting in a final TAE-1/CsFAMAPIBr work function (4.20 eV) higher than for the spiro-OMeTAD/CsFAMAPIBr (4.08 eV). The representative CPD parabolae, as well as the calculated work function values for each sample are plotted in Figure 5.23
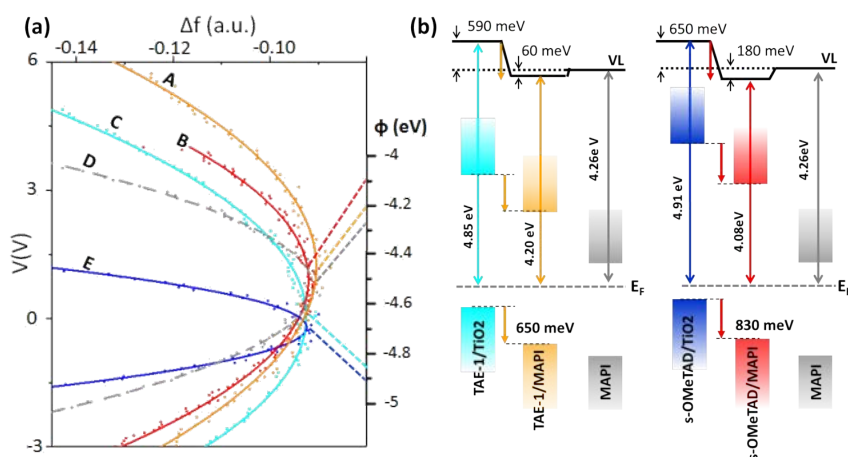
Fig. 5.23: a) ϕ values obtained from the contact potential difference (CPD) between tip and sample for the pristine MAPI (D), spiro-OMeTAD/MAPI (B) and TAE-1/MAPI (A) devices (where MAPI holds for CsFAMAPIBr), as well as on spiro-OMeTAD/TiO2 (E) and TAE-1/TiO2 (C) employed as control samples. The corresponding work function values obtained from the parabolic fit of the data (continuous lines) are given at the right axis. (b) Scheme of the proposed energy diagram for the different layer stacks of materials in the solar cells. The corresponding vacuum level (VL) shifts are obtained from the work function values.

The different behaviour of each HTM on the CsFAMAPIBr layer reveals that the VL of spiro-OMeTAD shifts towards lower ϕ values with respect to that of the perovskite (180 meV) than the TAE-1.

Although the absolute position of the HOMO levels respect to the Fermi level cannot be determined by this local probe technique, and certainly differ from the values extracted from cyclic voltammetry (Figure 5.22(b)), the higher V_{OC} seems too indicate a more favourable energy alignment for the spiro-OMeTAD despite of its higher HOMO level position, which is supported by the proposed energy diagram deduced from the work function measurements by KPFM (Figure 5.23 (b)). Consequently, the spiro-OMeTAD experiences a larger shift of its HOMO towards the VBM of the perovskite, than the TAE-1 (60 meV).

5.2.4 Conclusions

In this work, we have investigated the causes of the differences in V_{OC} of CsFAMAPIBr solar cells with two different HTMs, which show quite similar chemical structure and red/ox properties: Diarylamino-substituted tetraarylethene-based molecule (TAE-1) and spiro-OMeTAD.

According to the estimated HOMO position by cyclic voltammetry, devices with TAE-1 as HTM are expected to have higher V_{OC} than with spiro-OMeTAD. However, the V_{OC} of the fabricated devices shows the opposite trend. By transient optoelectronic measurements it was proven that there are no significant differences in the recombination dynamics at the interface for both devices. KPFM experiments, however, indicate significant modification of interfacial energetics upon HTM casting. Specifically, TAE-1 seems to lead to a less favourable alignment of the energy in contact with the perovskite layer, which would explain the lower V_{OC} values experimentally obtained.

Solvent vapor annealing effect on solution-processed solar cells.

6

Contents

6.1 Photovoltaic response upon SVA: the role of alkyl side chains

The morphology of the active layer plays a critical role in the performance of bulk heterojunction organic solar cells [183, 184]. Different methods have been developed in order to gain control over the structure and spatial organization of donor and acceptor materials in the active layer such as the use of additives [185, 186], thermal treatment [187] or solvent vapor annealing (SVA) [188–191]. This section is adapted from the publication [192]. My contribution in this work has been the structural characterization by grazing incidence wide angle X-ray scattering (GIWAXs), as well as some of the KPFM measurements. In the last years, solution−processed bulk heterojunctions prepared from conjugated oligomers, considered *small molecules*, as

donors and fullerenes as acceptors have developed a great interest, due to their advantages respect to conjugated polymers, such as well defined molecular weight, high purity and high batch-to-batch reproducibility [189, 193]. Among these oligomer classes like squaraines [194], merocyanines [195] and oligothiophenes [196–199] are the co-oligomers, which consist of donor and acceptor subunits [188, 191, 192, 200, 201]. In this part of the thesis, the donor material consisted of a series of A-D-A oligomers with a dithienopyrrole (DTP) central unit as donor moiety (D) and dicyanovinyl-substituted oligothiophene acceptor units (A) [191, 202]. Figure 6.1 represents the two isomers
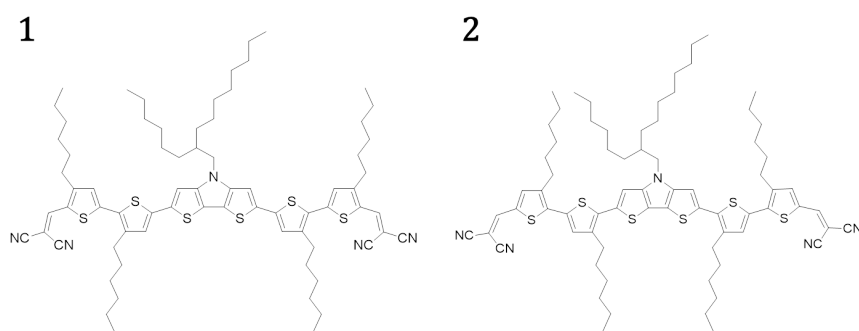
Fig. 6.1: Chemical structures of A-D-A type oligothiophene 1 and 2, composed of dicyanovinyl (DCV) groups as terminal acceptor (A) and a fused dithieno$[3, 2 − b : 2, 3 − d]$pyrrole (DTP) as a central donor (D) unit, which only differ in the positioning of the side chains.

object of study, synthethized by Dr.C. D. Wessendorf. in Dr. P. Bauerle's group. These two isomers were found to present the major differences in performance and photovoltaic properties in a previous study [191]. Both oligomers differ in the position of the linear alkyl chains, either outer (1) or inner (2) position.

Solvent vapor annealing (SVA) is a well studied method for tuning the morphology of the photoactive layer. It consists in exposing the sample to vapors of one or more solvents. When applied, the solvent vapor penetrates into the blend allowing for re-organization of the donor and/or acceptor materials. By doing this, it has been demonstrated to affect the polymer [189, 190] or oligomeric [203] donor crystallinity as well as the fullerene acceptor aggregation [190]. By affecting the

crystallinity, this method strongly influences the phase separation between donor and acceptor in BHJs solar cells, therefore affecting the photovoltaic characteristics.

In this work, oligomers (1) and (2) (Figure 6.1) were used to fabricate bulk-heterojunction solar cells and went through a solvent vapor annealing process in order to enhance their performance. Table 6.1 collects the photovoltaic parameters for both oligomers before and after solvent annealing treatment. As can be observed, solar cells with $1:PC_{61}BM$ as absorber material are only slightly improved after SVA from 3.8 % to 4.6 % PCE, whereas devices based on oligomer 2 show a much strong increase in efficiency upon SVA. Oligomer 2, that showed the best performance in the previous work [191], was tested with both $PC_{61}BM$ and $PC_{71}BM$ as acceptors. A drastic improvement is achieved for both fullerenes upon SVA, from 1.1% PCE to 6.1 % PCE in the case of $PC_{61}BM$ and from 1.1% PCE to 7.1 % PCE in the case of $PC_{71}BM$. The main difference between both lies in the J_{SC} (12 mAcm^{-2}) with $PC_{71}BM$ instead of 10 mAcm^{-2} with $PC_{61}BM$ as result of enhanced absorbance of $PC_{71}BM$ (Figure 6.2).
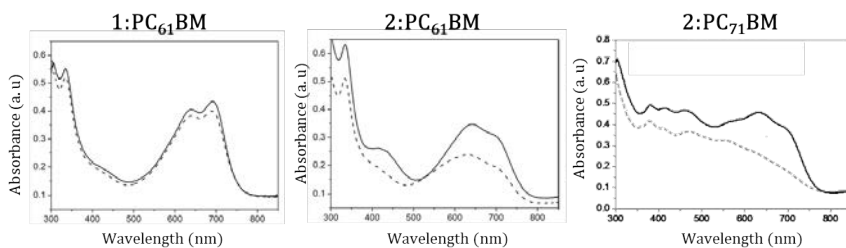
Fig. 6.2: Absorption spectra of $1:PC_{61}BM$, $2:PC_{61}BM$ and $2:PC_{71}BM$ solar cells without (dotted line) and with (full line) SVA.

In Figure 6.2 it can be observed how the UV-visible absorption spectra barely changes upon SVA for $1:PC_{61}BM$, while for 2, there is a noticeable change for both fullerenes. This is consistent with the enhanced parameters showed in Table 6.1. For $1:PC_{71}BM$, as reported in the previous work, the absorption peaks at 640 nm and 691 nm are only slightly increased by SVA. In contrast, for $2:PC_{71}BM$, without SVA (dotted line) the spectrum has only peaks in the region where $PC_{71}BM$

	SVA (s)	PCE(%)	V_{OC}(mV)	J_{SC} (mAcm^{-2})	FF(%)
1:PC$_{61}$BM	0	3.8	837	7.1	64
	120	4.6	840	8.4	66
2:PC$_{61}$BM	0	1.1	817	4.1	32
	90	6.1	843	10.1	72
2:PC$_{71}$BM	0	1.1	816	4.4	30
	90	7.1	827	12.0	71

Tab. 6.1: Photovoltaic parameters for best cells made from oligomers 1 and 2 blended with PC$_{61}$ or PC$_{71}$, respectively, with and without SVA.

absorbs, with a maximum at 378 nm and a shoulder at 410 and at 469 nm. In the range of the donor, at higher wavelengths, the spectrum does not show more peaks, with only two broad shoulders around 548 and 617 nm. Upon SVA, the absorption is strongly enhanced and exhibits more pronounced spectral features which are strongly red-shifted to 569 (shoulder), 632 (maximum) and 693 (shoulder) nm (full line). Similarly, for 2:PC$_{61}$BM, without SVA the absorption maximum is at 632 nm, with a small shoulder at 690 nm. After SVA treatment, there is a noticeable red-shift of the absorption peak to 642 nm and 697 nm.

6.2 SVA effect on crystallinity and morphology

The changes manifested in the UV−visible absorption spectra are indicative of significant morphological changes, probably leading to better molecular packing after SVA. In order to study the structural changes of the BHJs upon SVA, the absorber layers have been investigated by GIWAXS, PL and KPFM.

In Figure 6.3(a) is depicted the scheme of the diffraction measurement geometry for GIWAXS experiments. The two-dimensional (2D)
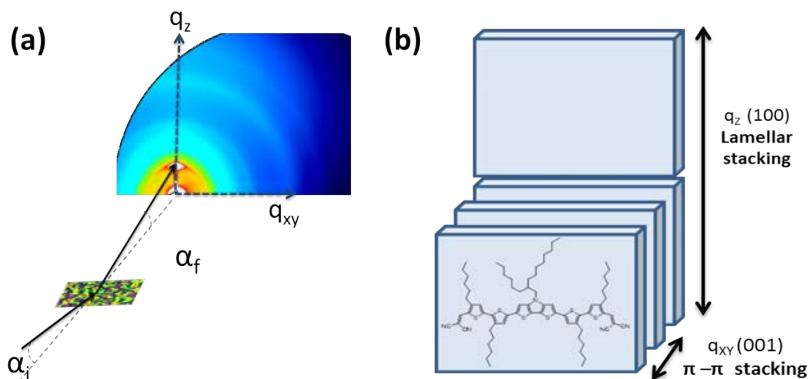
Fig. 6.3: (a) Scheme of the GIWAXS diffraction geometry, where q_z and q_{xy} are directions in the detector reference frame. The absolute value of the scattering vector, q, is determined from the total scattering angle 2θ, $q = 4\pi \sin 2\theta / \lambda$. (b)Scheme of molecular packing crystallites with edge-on orientation on the surface.

GIWAXS patterns provide information of the lamellar stacking spacing (Bragg peak, (100)) and the spacing associated to the π-π stacking of the oligomers and allow us to describe the molecular packing crystallites as shown in Figure 6.3(b).
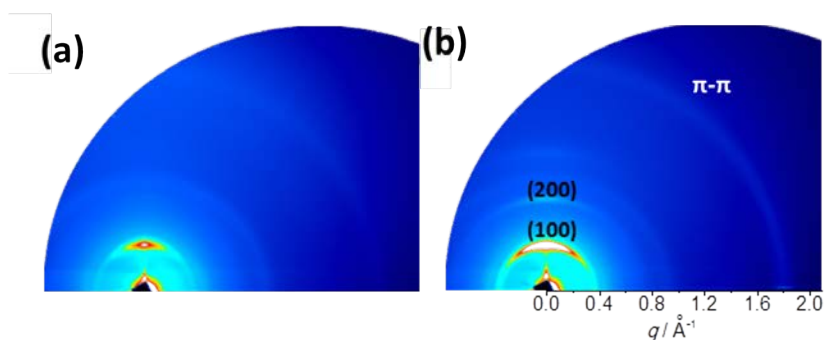
Fig. 6.4: 2D diffraction patterns of the pristine films for 1 (a) and 2 (b), respectively.

Figure 6.4 displays the 2D GIWAXS patterns of neat 1 (a) and 2 (b) films. The (100) Bragg peak corresponding to a lamellar stacking of the oligomers is found at q = 0.392 Å^{-1} for 1 and at q = 0.370 Å^{-1} for 2, which indicates an average spacing of about 16Å for 1 and

17 Å for 2. The intensity of the (100) peaks indicates that the predominant orientation is the edge-on (parallel orientation of the (100) planes on the surface). However, the arching of the intensity around (100) indicates a certain angular distribution of the orientation of the oligomer crystallites. For both films, a scattering ring appears at q = 1.80 Å^{-1}, corresponding to the π-π stacking of the oligomers, with associated spacing of ≈ 3.5Å. The fact that it appears as a rings takes into account the fraction of randomly oriented crystallites in the film. Figure 6.5 shows 2D X−ray scattering patterns of 2:PC$_{61}$BM and 2:PC$_{71}$BM films, before and after 90s of SVA with chloroform. It is noticeable how, before the SVA treatment, both blends exhibit the (100) diffraction peak of the oligomer and the isotropic scattering ring corresponding to the short-range ordered aggregates of the fullerene component (crystalline coherence length of $\approx$ 3.5nm) [204]. If compared with the pristine film in Figure 6.4 (b), blending the oligomer with the fullerene does not appreciably change the orientation or spacing of the lamellae. The (100) scattering intensity appears as a superposition of a scattering ring, that corresponds to the formation of unoriented crystallites, and an out-of-plane peak indicating a fraction of crystallites predominantly edge-on oriented (scheme in Figure 6.3(b)) with an angular distribution orientation of $\sim 6°$. Such mixture of aligned lamellae and unoriented crystallites has been observed for polymer blends and attributed to heterogeneous nucleation at the film interface and at the bulk of the film [204, 205].

The faint intensity of the π-π stacking ring, however, when compared with the pristine films, suggests that the fullerene impedes to large extent the π-π stacking in the 2 oligomer. This might be related to the large steric hindrance of the hexyl side chains of the oligomer, as detailed in the previous work [191].

Upon SVA, the most noticeable effect is the increased intensity of the π-π stacking ring (profiles in Figure 6.5 (e) and (f)), indicating more extended π-conjugation. This enhancement correlates with the red-shift observed in the UV-vis absorption upon SVA and is probably
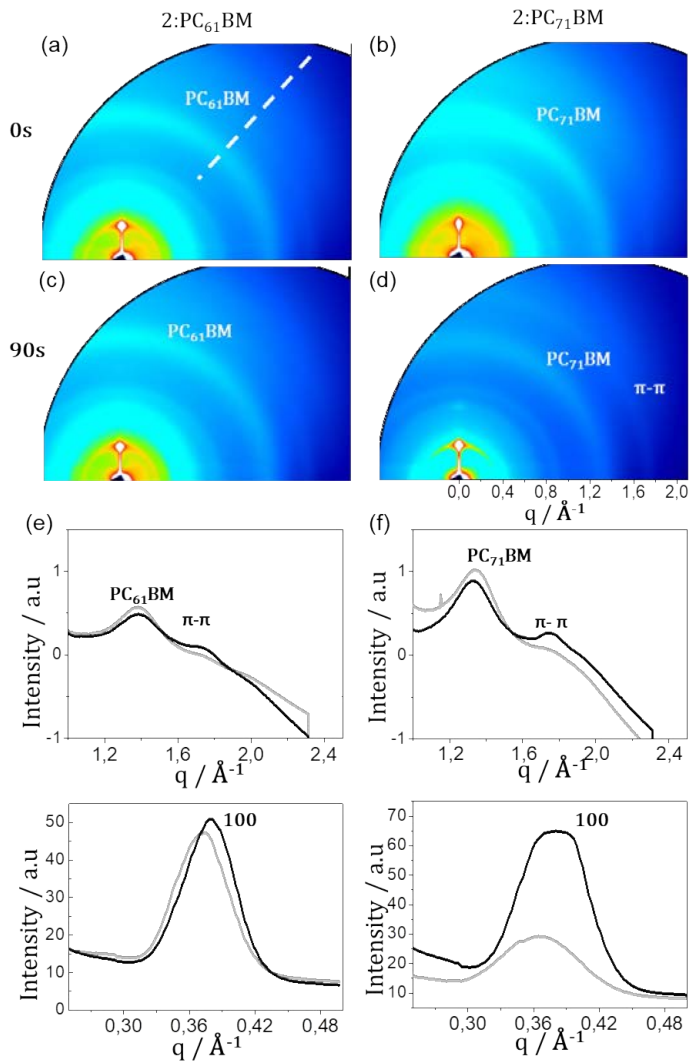
Fig. 6.5: Two dimensional diffraction patterns of 2:PC$_{61}$BM and 2:PC$_{71}$BM. (a), (b) before and (c), (d) after 90 s of SVA in chloroform environment. (e) Radial profiles along the marked direction (white dashed line) showing peaks corresponding to PCBM and $\pi - \pi$ stacking of the oligomer, and (f) along the (100) Bragg peak (black dashed line) before (grey) and after SVA (black).

strongly contributing to the improvement in the photovoltaic performance (Table 6.1), as the π-π stacking plays an important tole in facilitating hole mobility and charge delocalization.

In order to estimate the coherence length of the π-π stacking with better signal/noise ratio, GIWAXS employing a point-detector was performed. Using this detector, the in-plane peak FWHM was calculated and a mean coherence length of the π-π stacking of $2\pi/\delta \sim 10$ nm was estimated, corresponding to ~ 28 π-π stacked molecules. In Figure 6.5 (e) and (f) (right) are plotted the profiles along the (100) Bragg peak. In both films, it is noticeable a shift towards larger q values upon SVA (from 17.1Å to 16.6Å for 2:$PC_{71}BM$ and from 16.9 to 16.6Å for 2:$PC_{61}BM$). This indicates a slight densification of the lamella packing for both oligomers. In Table 6.2 are collected the obtained average

| SAMPLE | Average spacing and Bragg peak position | | | |
| | Before SVA | | After SVA | |
	Å	q(Å^{-1})	Å	q(Å^{-1})
1 pure	15.9	0.392		
2 pure	17.0	0.370		
1:$PC_{61}BM$	15.9	0.395	15.8	0.399
2:$PC_{61}BM$	17.0	0.372	16.6	0.378
2:$PC_{71}BM$	17.0	0.367	16.6	0.379

Tab. 6.2: Average spacings and Bragg peak positions before and after SVA of either pure oligomers 1 and 2 or blended with $PC_{61}BM$ or $PC_{71}BM$, respectively.

(100) q positions for all the films. Another effect of the SVA treatment is observed in an increase in the (100) Bragg peak intensity, indicating an enhancement of the (100) oriented crystallites (Figure 6.5 (f)). However, the angular distribution of edge$-$on oriented crystallites is not very affected, indicating enhanced crystallization of unoriented crystallites. In summary, for oligomer 1 (only blended with $PC_{61}BM$), similar structure is observed: edge-on oriented oligomer (angular distribution of $\sim 7°$), randomly oriented crystallites and disordered $PC_{61}BM$. Differently from oligomer 2, the ring correspondent to the π-π stacking is visible before the SVA treatment (Figure 6.6). Moreover, the SVA treatment does not seem to induce visible changes in the ordering of $PC_{61}BM$ and the π-π stacking as well, as the profiles
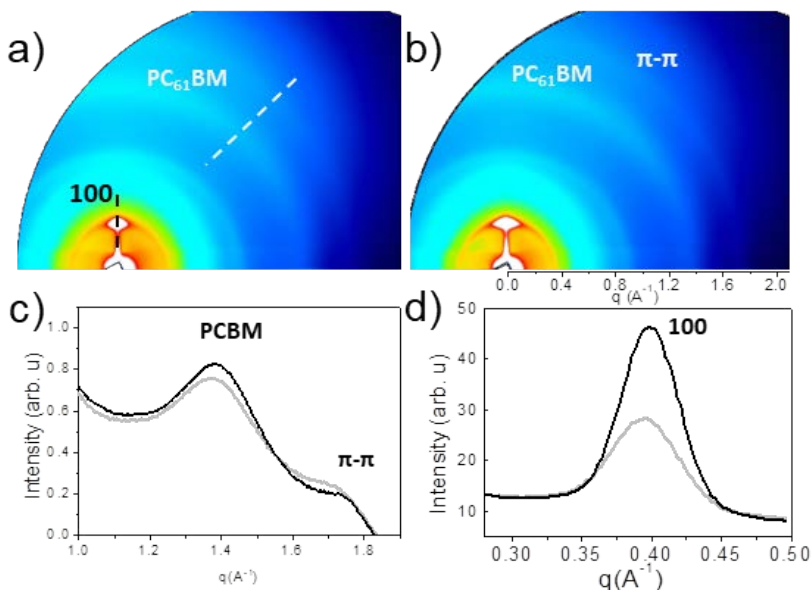
Fig. 6.6: Two dimensional diffraction pattern of 1:PC$_{61}$BM (a) before and (b) after 120 s of SVA in chloroform environment. Radial profiles along marked directions before (grey) and after SVA (black): c) along white dashed line, showing peaks corresponding to 1:PC$_{61}$BM and π-π stacking of the oligomer, (d) along black dashed line, the (100) Bragg peak.

in Figure 6.6 (c) almost overlap. However, as in oligomer 2, upon SVA treatment the (100) intensity peak is increased (profile in Figure 6.6 (d)), which implies an enhanced crystallization of unoriented crystallites. As for oligomer 2, a slight densification of the lamella packing is observed.

One critical issue in the devices performance is the nanoscale morphology (including phase separation of both components) in the oligomer-fullerene blend [206–208]. In order to investigate the SVA effect on the phase segregation, contact potential difference (CPD) maps were made with KPFM. It has been proven that these maps can contain information related to local differences in work function [209, 210], or to charging phenomena in the different materials. Thus, spatially resolved contact potential difference can provide with info about the photo−induced charges in donnor-acceptor systems [211–213].

The sign and magnitude of the surface potential in a donor-acceptor blend will depend on the properties of the underlying substrate [214]. This implies that the measured CPD will be influenced by the charge equilibration with the surface.
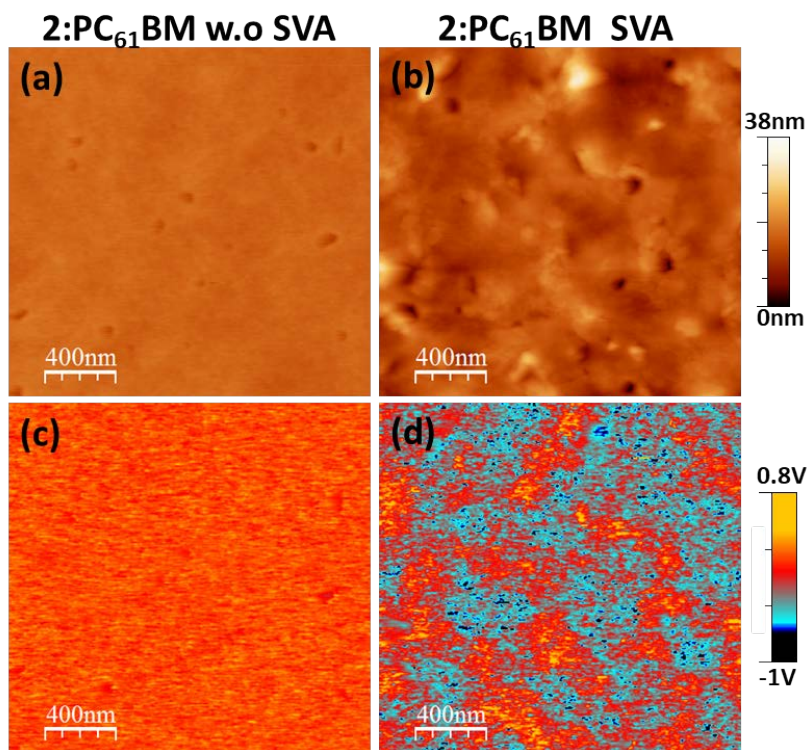
Fig. 6.7: Topographic (a),(b) and (c), (d) CPD images of a 2:$PC_{61}BM$ film before and after SVA.

In Figure 6.7, topographical and CPD images are shown of 2:$PC_{61}BM$ films before and after SVA. After the solvent vapour treatment, two noticeable phenomena occur: the surface roughness increases from ∼1.2 up to ∼3.3 nm (Figure 6.7 (a) and (b)) and higher contrast arises in the contact potential image in Figure 6.7 (d). We ascribe these emerging features to re−organization process, that would lead to an enhanced phase separation of the oligomer and fullerene components. In the case of the 1:$PC_{61}BM$ films, new contrasts emerge as well in the CPD image upon SVA treatment (Figure 6.8(c) and (d)). However, these structures show dimensions up to 350 nm, while for oligomer

Chapter 6 Solvent vapor annealing effect on solution-processed solar cells.

1:PC$_{61}$BM w/o SVA   **1:PC$_{61}$BM SVA**
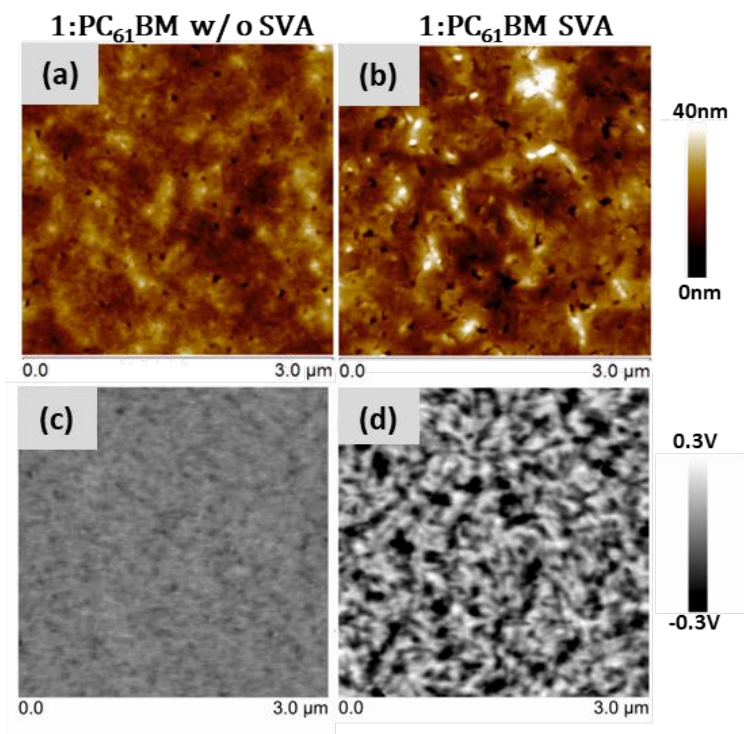
Fig. 6.8: Topographic (a),(b) and (c), (d) CPD images of a 1:PC$_{61}$BM film before and after SVA. Images courtesy of Dr. Andreas Arndt

2 the regions can be as large as 1μm, leading to conclude that phase separation appears for both oligomer blends but it is promoted more strongly for oligomer 2. However, it must be noted these regions are more likely to be oligomer and fullerene enriched regions rather than pure or acceptor phases. The stronger effect in the phase separation in 2:PC$_{61}$BM correlates with the more significant changes in the J$_{SC}$ in devices fabricated with oligomer 2 upon SVA. Noticeably, for oligomer 1, the surface roughness is only slightly affected, as can be observed in Figure 6.8(a) and (b).

Photoluminescence studies were also performed in the three blends upon SVA. In Figure 6.9 it can be observed how the photoluminiscence (PL) spectra is also affected by the SVA. Upon the treatment, for all three blends, an increase in the emission intensity is observed, in a more noticeable way for oligomer 2. For oligomer 2, the maximum
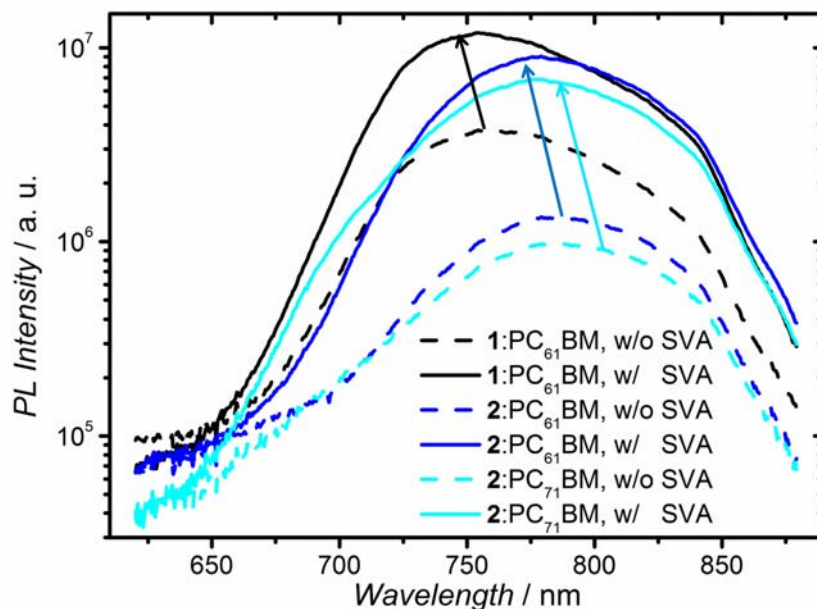
Fig. 6.9: Photoluminescence spectra of blends containing 1:PC$_{61}$BM (black), 2:PC$_{61}$BM (blue) and 2:PC$_{71}$BM(cyan) without (dashed) and with (solid) SVA.

PL intensity is increased by a factor of ~ 7 for both blends while for oligomer 1 it only rises by a factor of ~ 3. We attribute this rise to the increase in the average domain size in the blends upon SVA, which enhances the radiative recombination increasing the average distance to a donor−acceptor interface from the exciton generation spot. Therefore, for BHJs with the oligomer 2, PL suggest a stronger re−organization of donor and acceptor molecules upon SVA (related to oligomer 1) which is consistent with larger lateral length scale of phase separation observed in KPFM, as well as the changes in crystallization observed by GIWAXS. This improvement also indicates that, before SVA reatment, the exciton dissociation is not the limiting factor for the lower photocurrent in the oligomer 2 blends, but rather the charge transport due to the molecular organization in the blend.

6.3 Vertical blend composition

In order to study the vertical phase separation, we have used SIMS depth profiling and angle dependent GIWAXS measurements for films before and after SVA. In Figure 6.10 are shown the depth profiles of $1:PC_{61}BM$ (left), $2:PC_{61}BM$ (center) and $2:PC_{71}BM$ (right) films before (dashed lines) and after SVA (solid lines) on top of PEDOT:PSS and ITO. The signals generated exclusively by the oligomer parts of the blend are sulphur correspond to the sulphur ($S32^-$, dark yellow) and cyano group ($CN26^-$, blue). The oxygen ($O16^-$, red) derives exclusively from the PCBM, while the carbon signal ($C12^-$, black) is used for reference. The ITO is visible in the the $InO131^-$ (grey) signal. We can observe that, for both oligomers, the species corresponding to the oligomers and the fullerene are constant as a function of depth, with exception of the air surface, in which a oligomer enrichment (for a few nanometers) is found. The $1:PC_{61}BM$, upon SVA, does not present significant changes, which correlates with the little improvement in the devices performance. Remarkably, for oligomer 2 films, significant changes are observed upon SVA, being more pronounced in the case of blends with $PC_{61}BM$. For both PCBM, three regions are distinguished:

1. Oligomer−enriched surface

2. Sub−surface region with decreased concentration of oligomer, as evidenced by a depletion in the oligomer signals.

3. Slightly oligomer−enriched region up to bottom interface with more or less constant signals.

Upon SVA, the ratio oligomer 2 to $PC_{61}BM$ is affected, showing an oligomer poor layer close to the air interface and increased oligomer concentration on the bottom of the film. Interestingly, for the film with $PC_{71}BM$, (Figure 6.10(c)), we find a lower gradient than for $PC_{61}BM$, probably due to the larger size of $PC_{71}BM$, which allows less mobility
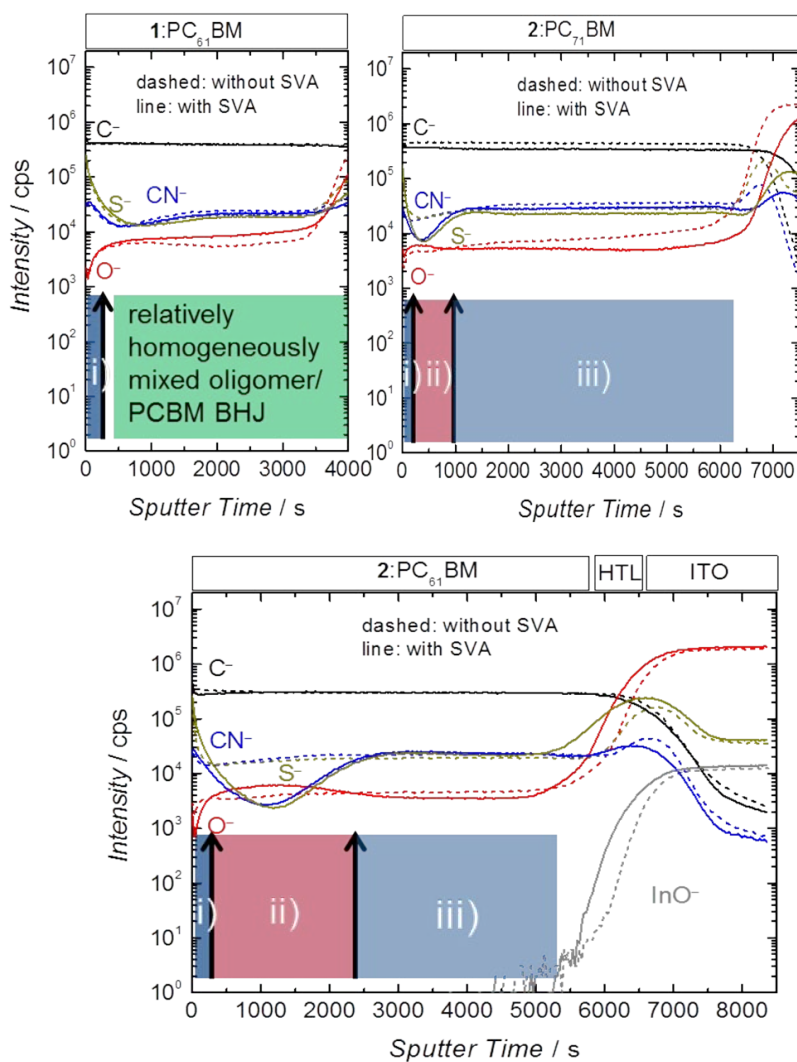
Fig. 6.10: Negative SIMS depth profiles of 1:PC$_{61}$BM (left), 2:PC$_{61}$BM (center) and 2:PC$_{71}$BM (right) absorber layers on ITO substrates with PE-DOT:PSS as hole transport layer (HTL) without (dashed) and with (solid) SVA. For the samples with SVA (solid lines) the three regions are marked: i) oligomer-enriched surface, ii) sub-surface region with decreased concentration of oligomer, iii) a slightly oligomer-enriched region up to the bottom interface with more or less constant signals.

within the absorber blend. This is not noticeable in the KPFM images. The vertical gradient for the oligomer 2 blends is probably a cause for

the improvement of the devices performance upon SVA: the anode is enriched with the donor and the cathode with the acceptor, facilitating the flow direction of charges inside the device and ensuring a more efficient charge extraction. This affects in a positive manner the series resistance (R_S) reducing it, and increasing the parallel resistance (R_P) and the J_{SC} upon SVA.

By changing the incident angle in GIWAS, we can have depth−resolved information of the structure. For 0.10° (black line), the incidence
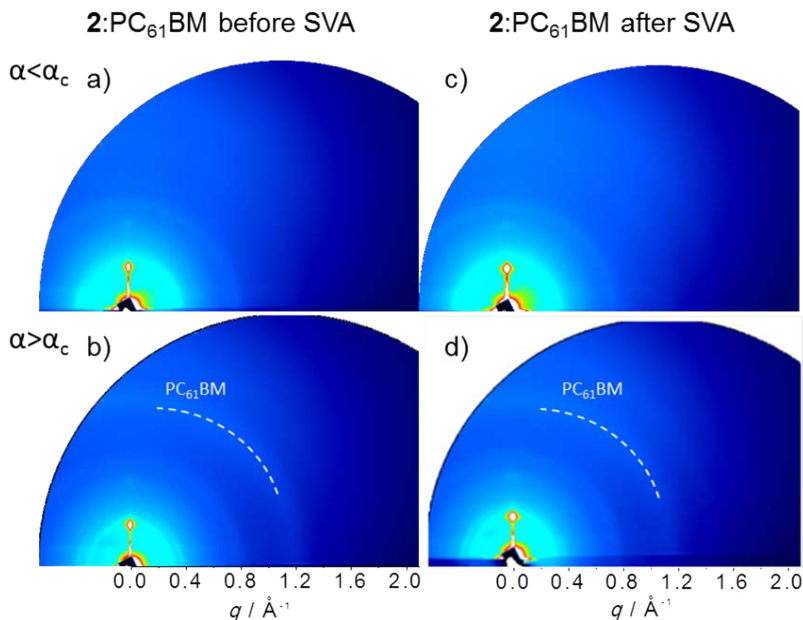
Fig. 6.11: Two dimensional diffraction patterns of 2:PC$_{61}$BM before and after solvent annealing, a) and c) for incident angle below the critical angle α_c, b) and d) for incident angle above α_c.

angle is below the critical angle (α_c), reaching a penetration depth of ~ 7 nm. As can be observed in Figure 6.11 (a) and (c) and in the in plane scan presented in Figure 6.12 (black line), for this penetration, the PC$_{61}$BM is not distinguishable while the (100) is clearly visible. For an incident angle of 0.14°, above α_c, when the X−rays penetrate in the bulk, the PC$_{61}$BM ring appears (Figure 6.11 (b) and (d) and in plan scan in Figure 6.12 (red line)). This confirms an oligomer−rich air/film surface which remains after SVA. The formation of a polymer
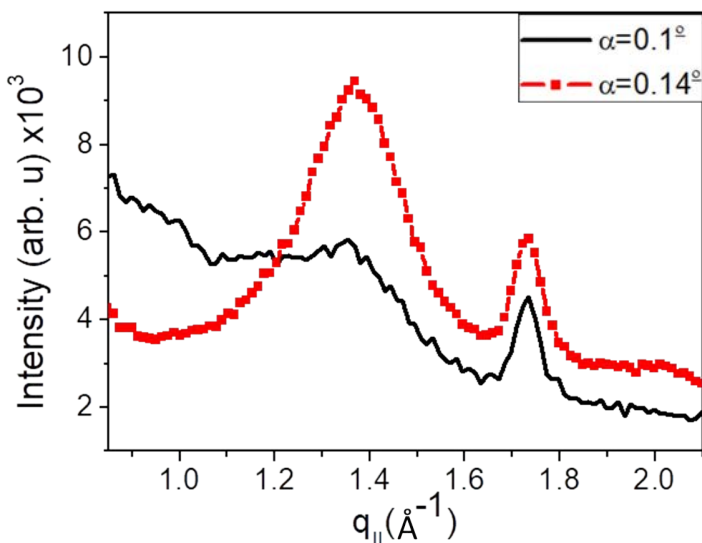
Fig. 6.12: In-plane scans for the solvent-vapor annealed 2:PC$_{61}$ films collected with a point detector for incident angle of 0.10° (below the critical angle, i. e. penetration depth limited to few nanometers) and 0.14° (above the critical angle, i. e. penetration of the x-rays in the bulk of the film).

"skin layer" on top of the active layer has been reported before for polymer BHJs such as P3HT:PC$_{61}$BM without appreciably impact on the performance of the OPV devices [215, 216]. The angle-dependent GIWAXS studies support the SIMS findings, being able to conclude that the active layer consists of a few monolayers of oligomer 2 on top, followed by a PCBM-rich/oligomer-poor layer and a slightly oligomer-rich layer at the bottom, as it is depicted in 6.13.

6.4 Conclusion

In a previous publication [191], it was reported that the oligomer 2 shows a larger solubility, compared to oligomer 1. This effect seems to be related to steric hindrance between the inner position of the hexyl side chains and the DTP−moiety, causing a twisted backbone of oligomer 2 and enabling a larger interaction between solvent

Fig. 6.13: Scheme of the vertical configuration of the oligomer 2:PC$_{61}$BM or PC$_{71}$BM solar cells. For the solvent-vapor annealed sample three regions are marked: i) oligomer-enriched surface, ii) sub-surface region with decreased concentration of oligomer, iii) a slightly oligomer-enriched region up to the bottom interface.

molecules with the hexyl chains. Indeed, the results from GIWAXS indicate that before the SVA treatment, the reduced planarity of the backbone hinders the development of π-π stacking in the as-casted films with oligomer 2. In contrast, for oligomer 1 before SVA, the improved photovoltaic performance can be explained by a better crystallinity than oligomer 2 due to the outer position of the hexyl chains, which allows higher co-planarity of its molecular backbone, facilitation the π-π organization of the oligomers during drying. Upon SVA, no major structural changes are observed for oligomer 1, correlating with the little improvement of the solar cells .

Upon SVA, oligomer 2 is affected in two different ways: (i) the π-π crystallization of the oligomer and (ii) an enhanced segregation of the fullerene component. The segregation of the fullerene leads to larger domains, revealed by AFM and PL and also to changes in the vertical composition, as confirmed by SIMS. After the SVA treatment, an oligomer-poor layer at the cathode side followed by an oligomer-rich layer at the anode side is obtained, which is beneficial for charge carrier extraction and therefore contributes to a higher current density and improved fill factor of the solvent vapour annealed devices. The fact that the gradient is stronger for PC$_{61}$BM than for PC$_{71}$BM is attributed to the smaller size of PC$_{61}$BM. Also, the slightly better performance of the devices with PC$_{71}$BM is attributed to the better absorption for this fullerene derivative. Thus, it can be concluded that the inner positioned hexyl side chains of isomer 2, although

they hinder the π-π stacking during spin-coating, they also allow larger diffusive motion of the molecules during the process of solvent vapour annealing and their later rearrangement in a more favourable nanomorphology.

Organic Film Effect Transistors

<div style="text-align: right;">7</div>

Contents

7.1 Nanoscale characterization

This Section is adapted from reference [217].

7.1.1 Introduction

Organic field effect transistors (OFETs) have been widely studied due to their potential in a wide range of applications such as printable and

flexible electronics. Organic semiconductors are especially interesting owing to their compatibility with solution-based coating techniques, which promise low-cost manufacturing by high-throughput continuous roll-to-roll printing methods on flexible substrates [218]. Over the past years intensive research efforts from both academia and industry have been performed for achieving superior performance of OFETs processed with solution-based coating techniques. As organic semiconducting polymers are generally less crystalline than small molecules and, as a result, tend to exhibit lower carrier mobility [219], many efforts have been devoted to develop soluble small conjugated molecules. However, the processing of small molecules from solution encounters coating problems related with dewetting and lack of control over the nucleation and growth of the molecular crystallites [7, 219]. Therefore, obtaining highly reproducible and uniform crystalline films by solution-coating is challenging for many molecular systems and, as a consequence, large performance disparity among devices is obtained even on the same substrate type [220, 221]. One of the advances in solution-manufacturing process raised from the idea of blending small conjugated semiconductor molecules with an amorphous insulating polymer to benefit from the advantages of both types of materials: uniform film-forming properties from the polymer component and high carrier mobility from the small molecule component [7, 72, 218, 222–224]. This strategy has led to an overall rise in charge carrier mobility accompanied by an improvement of devices processability, reproducibility and stability [72, 218, 225, 226]. A key to understand the superior performance of OFETs fabricated with blended films seems to be the vertical phase separation of the two material components, previously confirmed by ex situ measurements, such as transmission electron microscopy (TEM) [227, 228] secondary ion mass spectrometry (SIMS) [229] and neutron scattering [230] or variable angle spectroscopic ellipsometry [230]. Thus, discerning the structural details of the vertical stratification of the blends and the way it changes as a function of different processing parameters is an issue of fundamental importance. Successful demonstration of OFETs based on small molecule/polymer blends have been reported for Cn-BTBT

alkylated derivatives of benzothieno, one of the most promising small semiconducting molecules due to their proven high hole mobility [141, 227, 231–233]. It has been reported that blending polystyrene (PS) with 2,7-dioctyl[1]benzothieno[3,2-b][1]benzothiophene (C8-BTBT) (chemical structure depicted in Figure 7.1 (a)) enhances the device to device reproducibility, as well as improves the already remarkable stability of single component C8-BTBT films [218]. Moreover, evidences of the vertical phase separation of both components, with the PS segregated to the dielectric/semiconductor interface have been provided by cross-sectional TEM [227]. A bottom PS layer (in which a small percentage of C8-BTBT cannot be excluded) is believed to ensure a low density of traps at the semiconductor/dielectric interface [72, 218]. Nevertheless, the detailed structure of the films at the nanometer scale has not been fully determined yet.

In this chapter we have studied the OFET electrical properties as a function of the blend ratio, as a good systematic procedure to analyse the vertical phase separation taking place in each film and thus understanding its impact on the electrical properties of PS:C8-BTBT devices.

7.1.2 OFETs fabrication

Blend films were deposited by the bar-assisted meniscus shearing technique (BAMS) [218] (Figure 7.1 (b)) in ambient conditions, as described in Section 3.2. The materials, C8-BTBT and PS (with molecular weight Mw = 10000 g·mol^{-1}), were purchased from Sigma-Aldrich and used without further purification. Blend solutions of C8-BTBT and PS in chlorobenzene 2 wt% were prepared at different weight ratios: 1:2, 1:1 and 4:1. The Mw of the PS was selected following the previously published optimized conditions [218] and results in solutions with a good viscosity to be processed into homogenous films. The bottom gate substrates were Si/SiO$_2$ (200 nm SiO$_2$) from Si-Mat, and were cleaned with high purity acetone and isopropanol and then

dried under a nitrogen flux. The electrodes consisted of 7 nm of MoO_3 and 35 nm of gold deposited by metal evaporation through a shadow mask (channel lengths from L=30 to 100 μm and channel width of W=4 mm) in the configuration shown in Figure 7.1 (c).
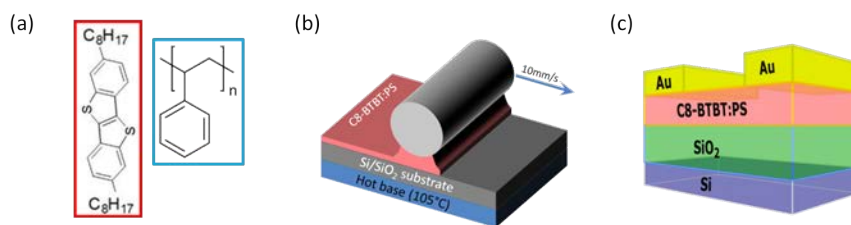
Fig. 7.1: (a) Chemical structures of C8-BTBT and PS. (b) Schematic illustration of the BAMS technique. (c) Scheme of the geometry of the devices.

7.1.3 Morphological characterization

Electrical characteristics and vertical phase separation

Devices fabricated with 1:2, 1:1, 4:1 ratios were characterized as described in Section 3.3.3. Representative transfer curves of the three devices (with a 30 μm channel length) are shown in Figure 7.2.
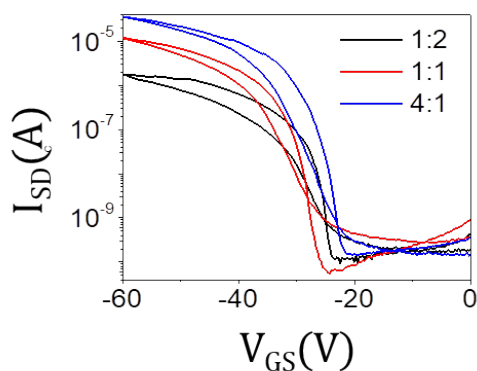
Fig. 7.2: Representative transfer curves corresponding to the OFETs for the 1:2, 1:1, 4:1 i ratios of C8-BTBT:PS (V_{SD}=40V)

The reproducibility of the devices was significant for the 4:1 ratio, with an average hole field-effect mobility of 0.3 cm^{2}V^{-1}s^{-1} [218]. The reproducibility of the devices was significant for this ratio, with over 90devices showing a good performance. For the 1:1 ratio, the reproducibility dropped around 80, and for 1:2 it reached 50. The performance of the latter formulations also diminishes with respect to the 4:1 ratio up to one order of magnitude.

Blend architecture and materials assignment

The optical microscope images for the three different ratios devices are depicted in Figure 7.3. Although devices 1:1 and 4:1 do not present distinguishable topographical features, for 1:2 device, the optical images reflect significantly smaller crystal domains. Topographic images

Fig. 7.3: Optical images of three different devices fabricated using different C8-BTBT:PS ratios (1:2, 1:1 and 4:1).

are displayed in Figure 7.4, showing very similar features for the three investigated blend ratios, hampering direct correlation between thin film morphology or crystallinity and electrical performance of the devices. Close inspection of the organic films topography inside the channel reveals a uniform and smooth surface consisting of large flat platforms or terraces with lateral sizes in the micrometer range. The height of each terrace is 3.1 ± 0.2 nm or multiples of it, as can be seen in Figure 7.5 which is only slightly higher than the inter-planar distance of the reported C8-BTBT thin film structure consisting of a layered herringbone packing with the lamellar planes parallel to the surface. We note that this is the most favourable orientation for charge transport in OFETs. [141, 142, 234].
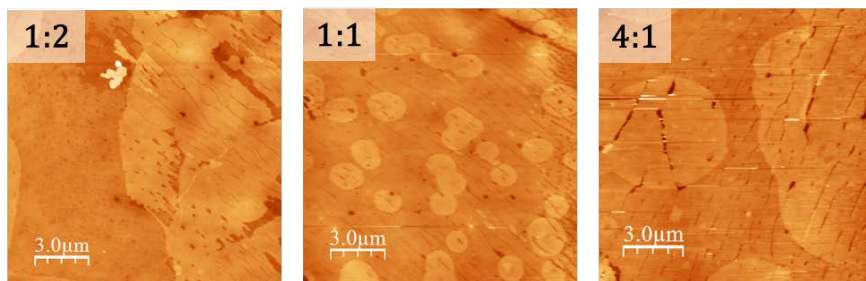
Fig. 7.4: Topographic AFM of three different devices fabricated using different C8-BTBT:PS ratios (1:2, 1:1 and 4:1).
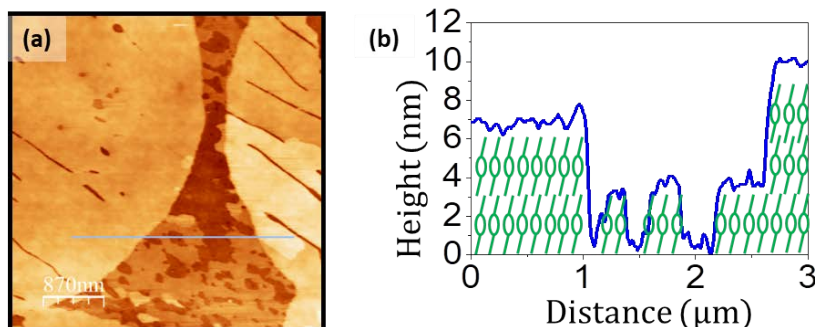
Fig. 7.5: (a) Topographic AFM image of a detail within the channel of a C8-BTBT:PS with 1:2 ratio OFET and (b) morphological profile along the marked line in (a). A cartoon with molecules at scale has been included to illustrate the proposed molecular packing and layer thickness.

When inspecting the films with AFM, two different contrast arise in the Lateral Force signal image, as can be observed in Figure 7.6 (bottom), more remarkably in the 1:2 ratio films. It seems that in the large scale images the only significant change in morphology is observed between the 1:2 ratio and the others, as bigger round island appear and the Lateral Force images show big areas of a brighter contrast.

As detailed in Section 3.3.1, the investigation of the local frictional properties by means of FFM has shown to be a valuable tool to reveal structural details of molecular films which are difficult to visualize with other techniques [100, 123, 235–237]. Furthermore, on samples with a heterogeneous composition, the lateral force maps have been proven to be useful in identifying materials with different chemical

nature (such as graphene flakes [238, 239] or organic islands on a substrate [119, 240, 241]) or to distinguish between two different chemical species in mixed self-assembled monolayers [242].
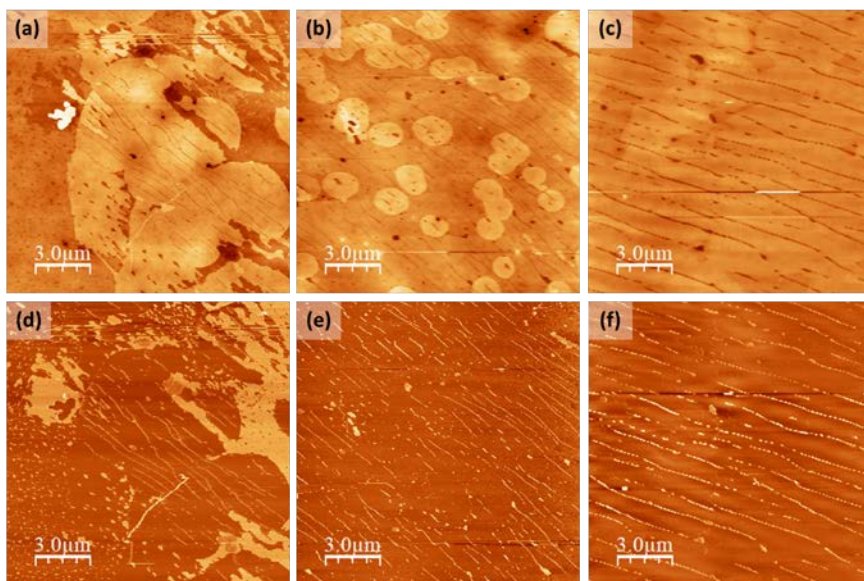
Fig. 7.6: Topographic (up) forward Lateral Force (bottom) images of three different devices fabricated using different C8-BTBT:PS ratios (1:2, 1:1 and 4:1).

During this part of the thesis, we have used FFM for identifying the two different blend constituents, PS and C8-BTBT, based on the frictional response.

We first analyse the C8-BTBT:PS 1:2 ratio, for which a substantial contrast between some areas is observed in the lateral force signal, where darker colour corresponds to lower friction (Figure 7.6 (bottom)). Figure 7.7(a) shows a topographic image and the simultaneously recorded lateral force taken on the device channel. On the terraces exhibiting the highest friction (lightest colour), molecular-resolved images are obtained (Figure 7.7(b)) with an in-plane lattice constant ($\approx 0.6 \pm 0.1$ nm) in agreement with the next neighbours distance of C8-BTBT molecules in the herringbone packing within the plane (a=0.59 nm, b=0.78 nm) [141], evidencing the high crystalline qual-

ity of the C8-BTBT layer. Moreover, information about the phase
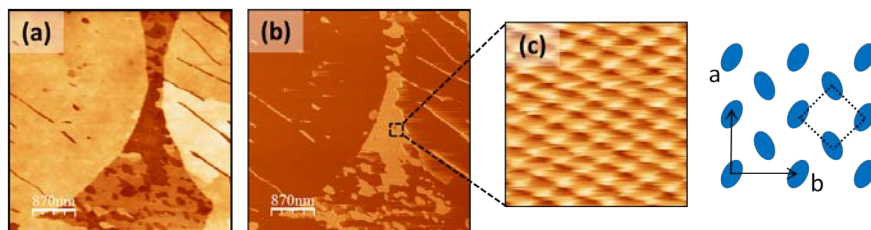
Fig. 7.7: (a) Topographic and (b) lateral force images obtained within the channel of the 1:2 OFET. (L=30 μm) (c) Magnified molecular resolution image (5 nm x 5 nm) of C8-BTBT and top view model of the in-plane herringbone unit cell reported in literature [141]. Blue ellipsoids represent the methylene groups.

separation is gained from the lateral force signal that allows relating the friction contrast with material composition, i.e., high friction for crystalline C8-BTBT and low friction for PS areas, respectively. As a matter of fact, molecular order is not observed on those terraces with low-friction as expected from the amorphous structure of PS.

PS skin layer Interestingly, by consecutive scanning (or slightly increasing the imaging load) an extremely thin layer is peeled off by the swept action of the tip, leaving uncovered a surface exhibiting the friction contrast of C8-BTBT where molecular resolved images are obtained. Figure 7.8 shows two different areas upon sweeping, in which the higher frictional C8-BTBT areas are uncovered. In (c) is plotted a topographic profile marked in (a) showing the height difference between the topmost layer and the C8-BTBT revealed underneath. The thickness of this ultrathin PS layer can be quantified from profile analysis between two consecutive images. This is depicted in Figure 7.9, in which (a) and (b) correspond to two consecutive topographical images. In the profile shown in (c) it is manifested how the vertical height is decreased by 0.5-2 nm upon sweeping.

Vertical structure This removal of such a thin material permits firmly establishing the existence of an ultrathin skin layer of PS with a thickness varying between 0.5 and 2 nm covering large areas of
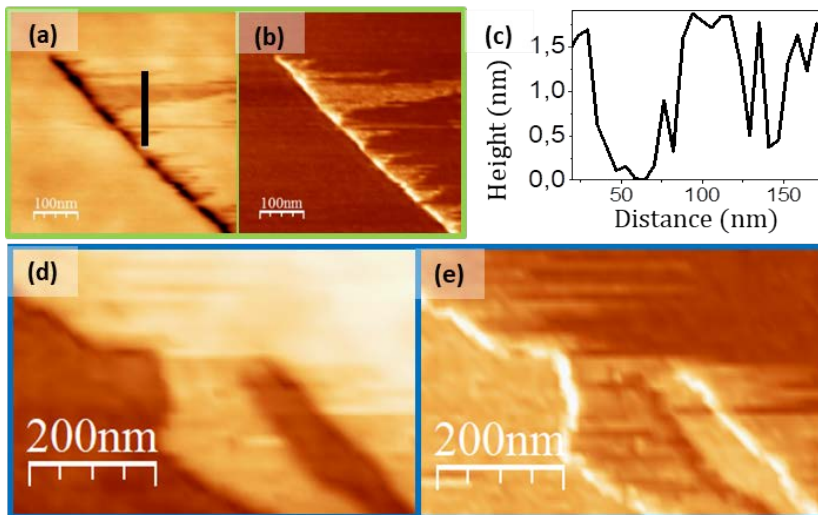
Fig. 7.8: Topography (a),(d) and forward lateral force (b)(e) images during PS layer removal of two different areas illustrating the difference in friction corresponding to PS and C8-BTBT. (c) Profile along the marked line in (a)
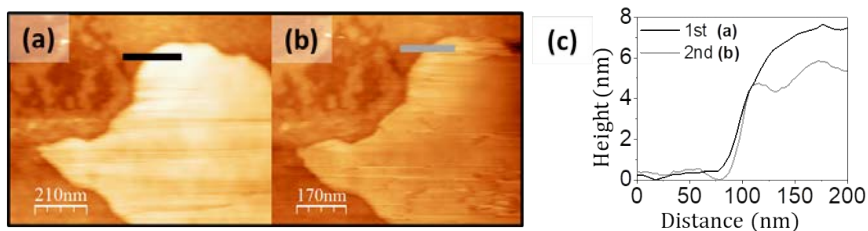
Fig. 7.9: (a) and (b) consecutive topographic AFM images showing that the PS skin layer existing on the surface top can be removed by the sweeping action of the AFM tip. (c) Profile taken along the marked lines.

crystalline C8-BTBT. In addition, correlating topography and friction is particularly helpful for determining the vertical structure of the system. The 1:2 ratios samples were of a big relevance in order to decipher the vertical structure of the , as there are regions of the channel where the C8-BTBT film is not complete but leaves exposed areas at lower vertical level.

The topographic image of an area for which the two different contrast are found in the lateral force image Figure 7.10 (b) is shown in (a). The frictional signal of the base level terrace is lower than that of

the surrounding C8-BTBT film and similar to that of the PS skin layer on the topmost level. In fact, no molecular order is attained at these regions suggesting a similar composition of skin and bottom layers. In order to clarify whether the lowest level in Figure 7.10 (a)
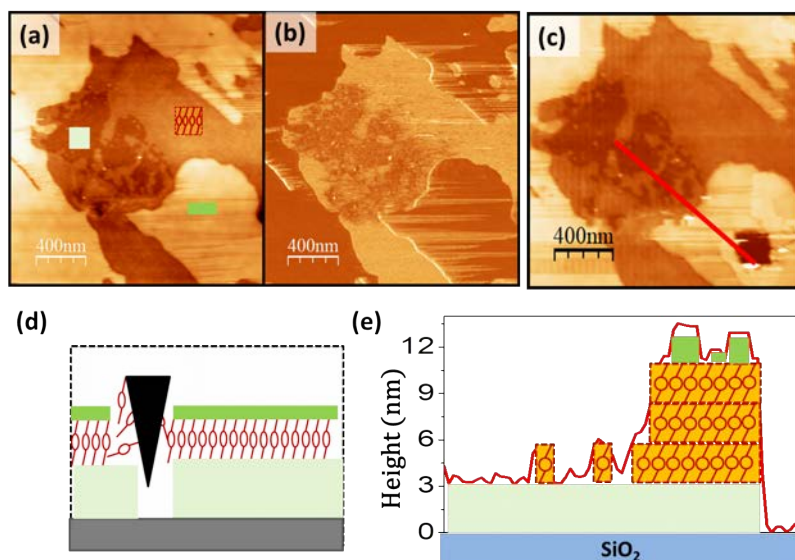
Fig. 7.10: (a) Topography and (b) lateral force images taken within the channel of a 1:2 OFET and (c) the same area after scratching the film. (d) schematic illustration of the scratching experiments. (e) Relief profile (red line) along the segment marked in (c).

corresponds to the substrate or to the presence of an underlying PS buffer layer, the film was locally scratched by scanning at a higher load (> 1 nN) till reaching the substrate (Figure 7.10 (d)). After this procedure, the same area was re-imaged at released load revealing that scratching had led to a square cavity exposing the bare substrate. The uncovered SiO_2 serves as a reference to evaluate the thickness of the different layers as well as that of the overall film (Figure 7.10 (c)). The height analysis confirms the existence of a layer of ∼2-3 nm under the C8-BTBT film (profile in Figure 7.10 (e)) identified by FFM as PS rich (Figure 7.10 (b)). We conclude that the films have a vertically phase separated structure consisting of a C8-BTBT crystalline film sandwiched between two PS layers at the bottom and on the top. The interface between the different layers is very smooth and structurally

well defined. The segregation of PS at both interfaces, with SiO$_2$ and air, despite their dissimilar surface energy, suggests a phase separation driven by the crystallization of the C8-BTBT rather than by surface energy minimization. The formation of a PS layer at the bottom has been suggested in the literature to serve as a nonpolar dielectric medium that assures low charge trapping between the dielectric and the organic semiconductor [72, 227, 243]. However, as far as we know, the presence of a skin layer on top of the film has not been yet experimentally proven for this system.

Following the above described procedure we characterized the vertical distribution of PS and C8-BTBT with nanometer precision for the samples prepared with diverse C8-BTBT:PS ratios (1:2, 1:1 and 4:1). Although the films surface morphology has a similar appearance (as can be observed in Figure 7.6) there are quantitative differences in the individual thickness of the three-layers of the structure, which are schematically summarized in Figure 7.11. The total thickness
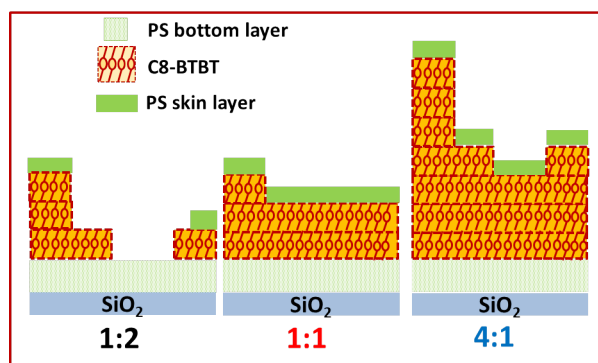
Fig. 7.11: Deduced structure of the films for the three C8-BTBT:PS ratios.

determined for the 1:2, 1:1 and 4:1 ratios was $\approx$ 16 nm, 13 nm and 25 nm, respectively. It is noteworthy that for the 4:1 ratio, with the thickest C8-BTBT layer, the extracted current and mobility are the highest, whereas for the blends with 1:2, where not even a complete C8-BTBT layer is formed, a poor performance and lack of reproducibility was obtained.

Remarkably, the PS bottom layer and skin layer have the same thickness for all compositional ratios. Conversely, it is noticeably that, compared to the other ratios, in the case of the 1:2 blend, the C8-BTBT layer is the thinnest and consists of an incomplete C8-BTBT film, with a heterogeneous distribution of heights that leaves uncovered some areas of the bottom PS layer. For the other samples, the hole transporting layer consists of two complete C8-BTBT layers for the 1:1 ratio and three complete layers for the 4:1 ratio. Hence, we conclude that the ratio between blend components affects the number of complete C8-BTBT crystalline layers formed, but it does not alter the thickness of both bottom and top PS layers. It must be also noticed
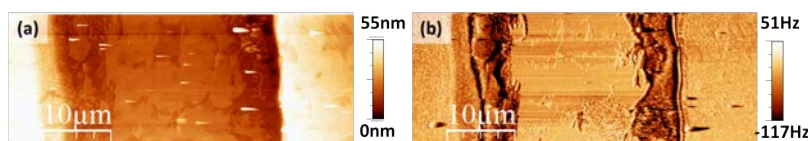
Fig. 7.12: (a) Topographic and (b) excitation images taken in the C8-BTBT:PS OFET with 1:2 ratio. In addition to the channel, the two electrode edges of the device are imaged to illustrate the defective characteristics of the film at the channel-electrode boundaries

that for the case of 1:2 blend, besides a thinner and discontinuous C8-BTBT film, a largely defective film coverage is also found at the electrodes boundary, with large areas of uncovered C8-BTBT, which suggests degradation of the film upon evaporation of the electrodes. This can be observed in Figure 7.12, in which the topographic (a) image of the channel is taken in AFM dynamic mode. The corresponding excitation signal image (b) reveals the presence of a defective PS coverage along the electrode borders, leaving exposed C8-BTBT.

Role of PS in the films stability.

In order to understand the role of the PS layers in a possible aging, two types of samples were investigated by AFM as a function of time: the above described C8-BTBT:PS blend (4:1) and control samples processed under similar conditions but containing only C8-BTBT.
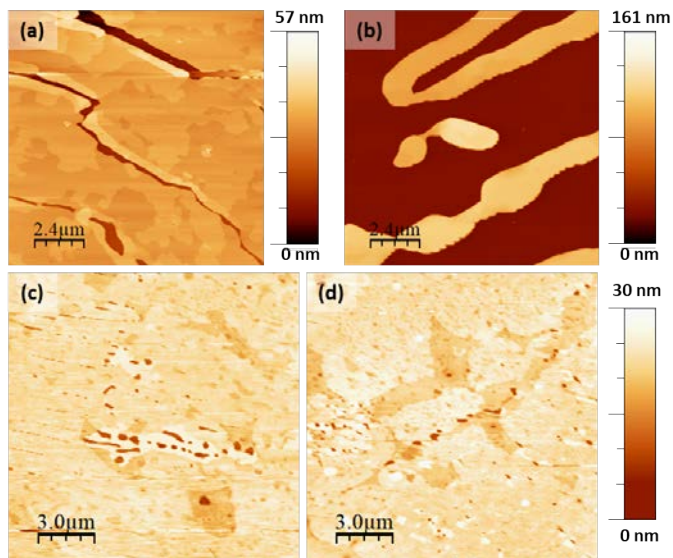
Fig. 7.13: Topographic images of (a) freshly prepared C8-BTBT film (without PS), (b) the same sample 4 months later, (c) freshly prepared C8-BTBT:PS film (4:1) and (d) the same sample 14 months later.

Comparison of the very same samples (Figure 7.13), just as prepared (fresh) and after several months reveals that, in particular, the single component C8-BTBT films suffer from a strong dewetting with time. The initial 30 nm thick and laterally continuous films (Figure 7.13 (a)) evolves to 90 nm high islands that leave uncovered large substrate regions (Figure 7.13 (b)). Remarkably, for the C8-BTBT:PS blend, morphologically and structurally aging is negligible and the films present basically the same appearance at the nanoscale after more than one year from preparation (Figure 7.13 (c) and (d)). It has already been reported that the hydrophobicity of the underlying PS buffer layer leads to an enhancement of the stability and reduces the trap density at the semiconductor-dielectric interface [72, 227, 243]. From this work, we conclude that the formation of both, top and bottom PS layers act as an encapsulation film for C8-BTBT impeding the dewetting of the C8-BTBT layers upon time.

7.1.4 KPFM in operando OFETs

Our results highlight that the C8-BTBT:PS blends have the basic ingredients to attain a high electrical performance: a crystalline film of C8-BTBT, favorably oriented for in-plane hole transport, sitting on top of a PS buffer layer acting as passivating dielectric and encapsulated by an ultra-thin PS layer conferring stability to the devices. The measured C8-BTBT thickness for each device correlates with their different electrical performance (Figure 7.2). As mentioned above, for the 4:1 ratio, with the thickest C8-BTBT layer, the extracted current and mobility are the highest, whereas for the blends with 1:2, where not even a laterally complete C8-BTBT layer is formed, a poor performance and lack of reproducibility was obtained. To better understand the implications of the vertically phase-segregated structure on the device performance, we performed a KPFM nanoscale characterization of the OFETs under operation, as the contact potential difference (CPD) maps can shed light onto the charge transport and carrier injection [54, 55, 109, 112].

The formation or not of the accumulation layer of the OFETs can be locally evaluated by measuring the CPD within the channel as a function of the applied gate voltage (V_{GS}). In order to get information from the whole tri-layer structure (including the top and bottom PS layers), the measurements were performed at channel locations well away from any film void or topographic defect. The results are plotted in Figure 7.14 for OFETs with 1:2 and 4:1 blend ratios together with the schematics of the interpretation in terms of the formation or not of the charge accumulation channel. A completely different tendency is observed for each device. In device 1:2, the measured CPD coincides with V_{GS}, implying that no charges are injected into the device to screen the applied gate bias and, consequently, the charge accumulation channel is not formed (bottom cartoon in Figure 7.14 (b)). This fact is directly related to the lateral discontinuity of the transport layer, consisting of an incomplete C8-BTBT film for this ratio. Additionally, in these devices, largely defective film coverage is also
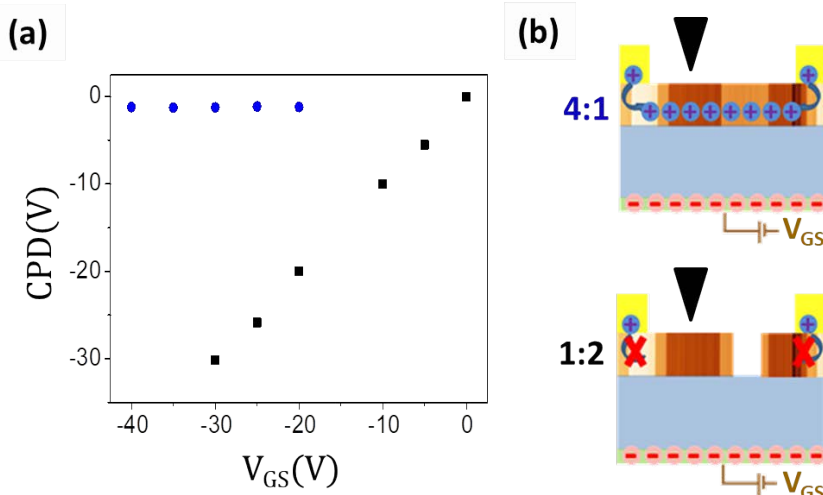
Fig. 7.14: (a) CPD values inside the channel for $V_{SD} = 0$ upon applied V_{GS} bias for 1:2 and 4:1 OFETs and (b) schematic illustration of the formation or not of the charge accumulation channel upon V_{GS} application for 4:1 (top) and 1:2 (bottom) devices, respectively.

found at the electrodes boundary, which suggests degradation of this C8-BTBT film upon evaporation of the electrodes.

These inhomogeneities at the film-electrode contact hinder at some extent the injection of charges needed to form the transport channel, however, there must be conductive paths connecting source and drain electrodes and making the device to work at macroscopic level although with low I_{SD} (see Figure 7.2). Conversely to the above description, devices based on the 4:1 blend show the expected behaviour for an operating OFET. In this case, the CPD in the channel does not change upon application of a gate bias, implying that charges are rapidly injected from the electrodes into the channel forming the accumulation layer that screens the gate bias (upper cartoon in Figure 7.14 (b)).

Contact resistance

It is noteworthy that even for the optimal case of the 4:1 ratio, the hole field-effect mobility extracted from the devices transfer characteristics (0.3 cm^{2}V^{-1}s^{-1} in average [218]) is lower than that reported in the literature for C8-BTBT OFETs [227]. One of the critical issues that can severely affect the OFET performance is the contact resistance between the metal electrodes and the semiconductor layer [57]. Determination of contacts resistance is found to be crucial in characterization of transistors as it may obscure mobility extraction. In the case of C8-BTBT, a hole injection barrier exists due to the large mismatch between the HOMO and the work function of the gold electrode that is commonly ameliorated by using self-assembled monolayers (SAMs) [244], inserting a MoO$_x$ layer [245], doping the contacts [246, 247] or using a metallic organic charge-transfer complex [248].

In order to understand the influence of the electrode on the mobility extraction, devices with the C8-BTBT:PS blend 4:1 ratio were fabricated with two different interlayers:

- **Au/MoO$_x$**: with one layer of MoO$_x$ is incorporated underneath the Au contact.

- **Au/F4-TCNQ** : F4-TCNQ is incorporated as interlayer underneath the Au contact in order to improve the injection properties by means of its strong acceptor character enabling contact doping.

Both contacts were studied by KPFM, as described in Section **??**. With these two configurations, CPD line profiles were taken for both linear and saturation regimes. Figure 7.15 displays representative CPD line profiles at two different V$_{SD}$ values (V$_{SD}$= 0 V and V$_{SD}$= -5 V) and using a V$_{GS}$= -40 V for the OFET with a 4:1 ratio of the C8-BTBT:PS blend and in which a MoO$_x$ layer has been incorporated underneath the Au contact (Au/MoO$_x$). As can be noticed from the CPD profile,
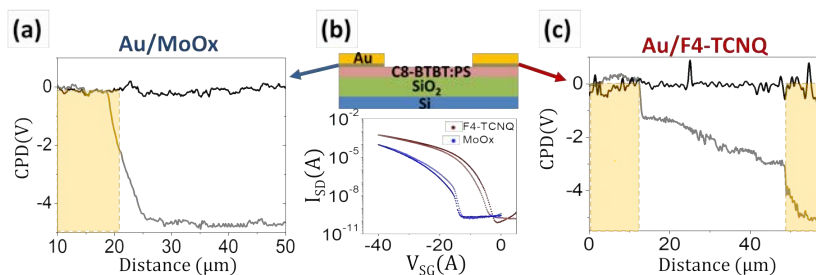
Fig. 7.15: Contact potential difference profiles for $V_{SD} = 0V$ and $V_{GS} = -40V$ (black) and $V_{SD} = -5V$ and $V_{GS} = -40V$ (grey) for C8-BTBT OFETs with 4:1 ratio using (a) Au/MoOx and (c) the Au/F4-TCNQ contacts (L=40 μm). (b) Top: Schematics and transfer characteristics of the devices fabricated with Au/MoOx (in blue) and Au/F4-TCNQ (in red) contacts.

microscopically the contact resistance (R_C) manifests by a sudden voltage drop at the source (marked in yellow). In order to assure the ohmic behaviour of the contact in the devices, and therefore extract the R_C values by Ohm's law, the CPD drop at the source and drain electrodes (see Figure 2.10) were taken as a function of the applied V_{SD}. The plot in Figure 7.16 confirms the linear dependence of the CPD drop with the applied bias to the electrodes. The extracted resistance at the source Au/MoOx contact is $R_C \cdot W = 23.9 k\Omega \cdot$ cm (OFET in linear regime, $V_{SD} = -5$ V and $V_{GS} = -40$ V). The resistance in the channel, estimated from the total resistance in the OFET, is $R_{CH} \cdot W = 0.74 \ k\Omega \cdot$ cm, which gives evidence of a large relative contribution of the contact resistance and suggests a considerably higher charge mobility in the film than the effective mobility extracted from the current-voltage characteristics, following equation 2.5.

Differently, in the Au/F4-TCNQ device, the strong drop at the source contact is decreased, and similar voltage drop in both source and drain electrodes the same order of magnitude. Therefore, the obtained resistances are very similar ($R_C \cdot W$=5.5 $k\Omega \cdot$ cm and $R_C \cdot W$=2.1 $k\Omega \cdot$ cm for drain and source contacts, respectively) and significantly lower by about one order of magnitude than those extracted for the Au/MoO$_x$ electrodes. This decrease in the contact resistance is manifested in the higher device mobility. On average from 11
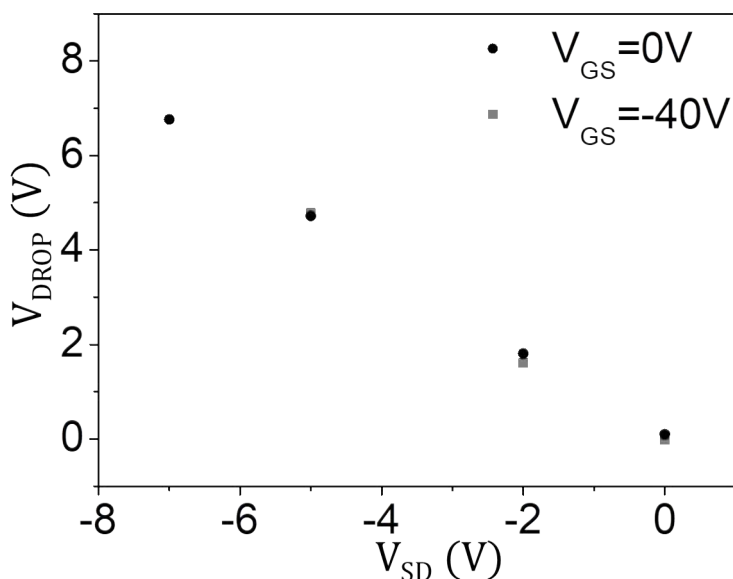
Fig. 7.16: Measured V_{DROP} in the CPD profiles as function of the applied V_{SD} showing a linear dependence for the device with 4:1 ratio of C8-BTBT:PS and Au/MoO$_x$ contacts.

devices, the switch-on voltage is considerably smaller (V_{ON} = -5 V) while the effective mobility is significantly larger (1.5 cm^{2}V^{-1}s^{-1}) for the OFETs with Au/F4-TCNQ contacts in relation to the reported Au/MoO$_x$ devices [218]. In particular, from the transfer characteristic curves of Figure 7.15 (b) the switch-on voltage and mobility values obtained were V_{ON} = -13 V and μ = 0.45 cm^{2}V^{-1}s^{-1} for the device with Au/MoO$_x$ and V_{ON} = -2.1 V and μ = 0.94 ^{2}V^{-1}s^{-1} for the device with Au/F4-TCNQ.

The estimated channel resistance ($R_{CH} \cdot W$ = 0.88 $k\Omega \cdot cm$) is comparable to channel resistance extracted from the devices with Au/MoO$_x$ electrodes, in agreement with a channel free of dopants. The role of contact doping has been widely studied, being the overall injection improvement attributed to a thinning of the depletion region (thus allowing tunneling injection) and to the reduction of traps density in the metal-semiconductor interface [56, 246, 249, 250]. The effect

of the contacts can be excluded to obtain the intrinsic field-effect mobility along the channel in the linear regime, considering $V_{SD} \ll V_{GS} - V_{TH}$ using equation 2.7 [52, 251, 252].

For the Au/F4-TCNQ eletrodes device the extracted channel mobility (i.e. excluding the influence of the contacts) is $\mu_{CH} = 10 \pm 1$ cm^{2}V^{-1}s^{-1}. Such a high channel mobility has been reported for C8-BTBT single-crystal devices fabricated by the inkjet-printing method [253], evidencing the high crystalline quality and the good connectivity between domain boundaries in the 4:1 ratio film prepared by BAMS.

7.1.5 Conclusions

By means of a microscopic characterization that combines topologic, tribologic (FFM) and electrostatic (KPFM) measurements we have deciphered the vertical structure of thin blend films with nanometer precision for three different C8-BTBT:PS ratios. We have also established the correlation between the stratified structure and the local electronic response of the OFETs. The films consist of a C8-BTBT crystalline layer sandwiched between two PS layers, one at the bottom and an ultra-thin skin PS layer on the top. We have confirmed that these PS layers improve the OFET stability, as they impede the C8-BTBT films dewetting through time. The thickness of the C8-BTBT layer depends on the blend composition ratio. In particular, the thinnest and laterally incomplete film is found for the 1:2 blend and the thickest film formed by three complete molecular layers, for the 4:1 blend. The investigation of the electronic properties at the nanoscale by KPFM in operando OFETs reveals that the thickness and continuity of the C8-BTBT layer play a fundamental role in the transport channel formation and, herewith, in the overall performance of the devices. KPFM also demonstrates that the contact resistance is the critical factor limiting the devices performance, which is significantly improved by doping the contacts with F4-TCNQ. By excluding the contact resistance, a

hole mobility in the channel as high as $\mu_{CH} \approx 10 \pm 1 \text{cm}^2 \text{V}^{-1} \text{s}^{-1}$ for the OFET with 4:1 ratio was obtained, giving evidence of the excellent transport properties of the film. The optimization of the contacts makes it feasible to reach hole mobility values in high throughput solution processed thin films close to those reported for single-crystal C8-BTBT-based devices.

7.2 Charge distribution in working OFETs by KPFM

As introduced in Sections 3.3.1 and 2.3.2, KPFM is a powerful method for characterizing the CPD at the nanoscale. It has been widely used to characterize charge transport in OFETs [55, 254, 255], as well as to analyse the charge trapping effect in the materials [109, 256, 257].

Understanding the appearance and location of the trapped charges is of relevance, as it can provide insight on one of detrimental phenomena occurring in OFETs: hysteresis in the transfer curves.

Hysteresis manifests as a difference in I_{SD} observed during forward and backward sweeps of the gate voltage V_{GS}. Among other causes (polarization of the dielectric material, charge injection from the gate electrode into the dielectric, charge injection from the organic semiconductor into the dielectric or the slow reaction of charge carriers), the presence of mobile traps has been proven to induce hysteresis in OFETs [258]. We can distinguish between two types of mobile traps,depending on the nature of the trapped charge: majority traps (like holes traps in C8-BTBT) or minority traps (like electron traps C8-BTBT). These traps, that fill fastly and empty slowly, are found in the channel close to the semiconductor/dielectric interface. The resulting lower back sweep current (BSC) hysteresis for both types of traps in a p-type OFET is described in Figure 7.17. For clarification, forward scan is considered the turn on direction of the device.
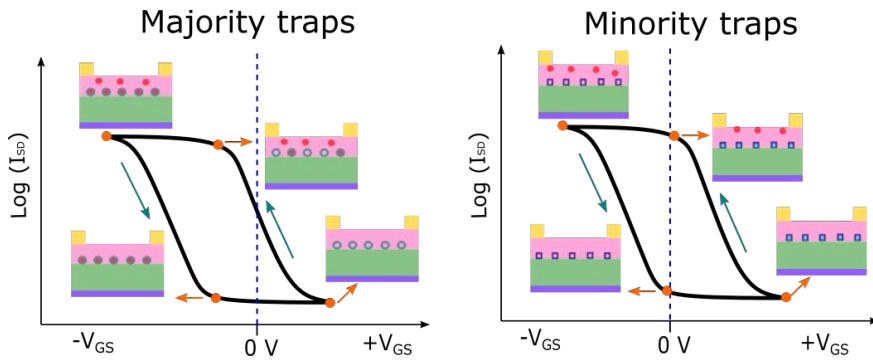
Fig. 7.17: Hysteresis for a p-type OFET caused by the trapping of majority (left) and minority (right) charge carriers. The holes are red dots and green circles correspond to holes traps. Electrons are light blue filled squares and electron traps are dark blue squares. Adapted from reference [258].

When the scan starts from the off-state, the majority traps (blue circles) are empty. When V_{GS} goes to negative values, holes (red dots) are induced due to the field effect. These holes are quickly trapped and, during the on-to-off sweep, are slowly released. It must be noted that the releasing speed is much slower than the sweep rate. Due to that, the resulting I_{SD} is lower.

In order to observe the minority traps (electrons), the sweeping is started in the on-state. In this state, the minority traps (blue squares) are empty. When the OFET is turned off and a positive V_{GS} bias is applied, the traps are quickly filled (light blue). When the OFET is turned on again, the negative trapped charges induce more holes in the channel than the ones corresponding to the applied V_{GS}, causing a higher I_{SD} in the forward sweep. It can be concluded that, as mobile charges are at the origin of the hysteresis cycles, the cycle itself would strongly depend on the sweeping speed or even on the history of measurements performed in the device.

So far we have introduced how the trapping dynamics of mobile charges cause the hysteresis in the devices. Fixed traps has been proven to be at the origin of V_{TH}. Specifically, a surface charge density of σ at the semiconductor/dielectric interface results in a

threshold voltage of $V_{TH} \cdot = \sigma/C_i$ [259], where C_i is the capacitance of the dielectric. These charges can be observed by KPFM as well. The expected CPD behaviour upon different gate bias is shown in Figure 7.18. When the device goes from the off to the on-state, the fixed
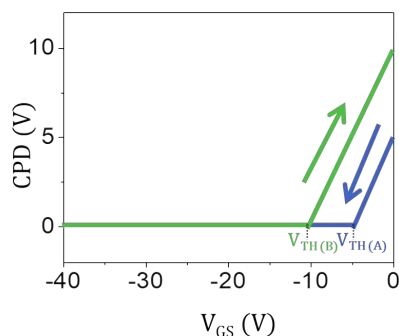
Fig. 7.18: Expected CPD behaviour for different applied V_{GS}.

trapped charges would be at the origin of $V_{TH(A)}$ (blue line). During the forward scan (switching on), the trapping of mobile charges would cause the hysteresis and therefore a shift in the threshold voltage to $V_{TH(B)}$ (green line). The involved charges in the hysteresis cycle could be quantified with the observed ΔV_{TH}.

The trapping sites in the channel are associated to grain boundaries and structural defects of the semiconductor film. During this Chapter of the thesis, one of the studied systems is an OFET fabricated with a 4:1 ratio of the blend C8-BTBT:PS with Au/F4-TCNQ contacts, that showed outstanding electrical characteristics: V_{ON} = -2.1 V and a channel mobility of $\approx$ 10 cm^{2}V^{-1}s^{-1} (with an effective mobility of μ = 0.94 cm^{2}V^{-1}s^{-1}). Figure 7.19 shows an area of the channel of this OFET examined by AFM, depicting Topography (a), Excitation (c) and CPD (d). An optical polarized microscopy image of the same area is shown in (b). While for other zones the optical polarized microscope different contrasts appeared, as can be seen in Figure 7.3, in this particular area the image shown in Figure 7.19 (b) does not give evidence of significant differences of crystalline orientation. However, some visible cracks can be distinguished along the channel, formed
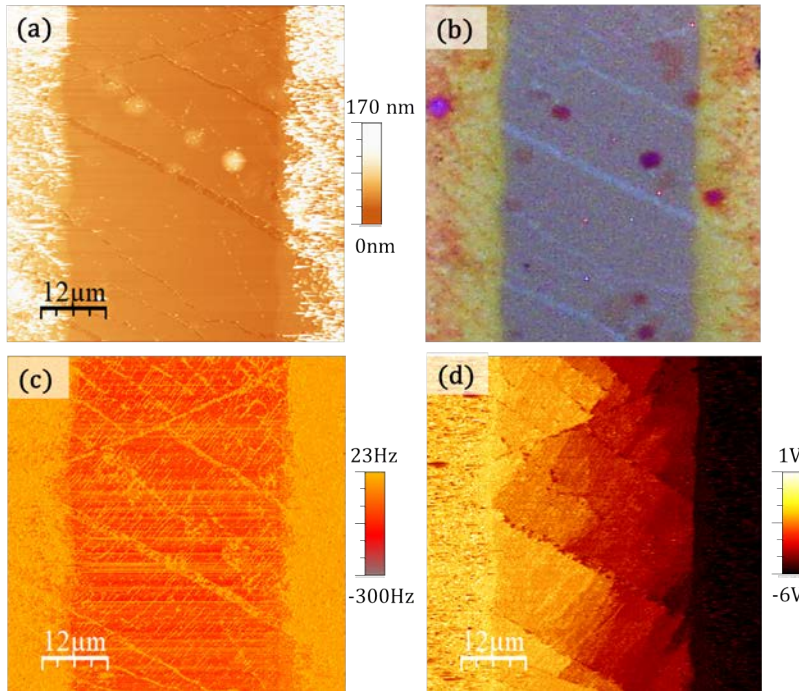
Fig. 7.19: Topographic (a), excitation (c) and CPD (working in saturation regime with V_{GS}= -6 V and V_{SD}=- 5 V) (d) maps of the same channel area. (b) Optical polarized microscopy images of the same area.

during the film formation by BAMs (explained in detail in Section 3.2). These cracks are also recognized in the topographic AFM image in Figure 7.19 (a) and in the Excitation channel image in Figure 7.19 (c). It is noteworthy that, besides the cracks visible in the topography, more features appear in the excitation channel. These features, not distinguishable in the topographic AFM neither in the optical image, consist on parallel lines perpendicular to the main cracks. These lines are also observed in the Surface Potential image in (d), in which the OFET is working in saturation regime. The CPD map shows abrupt changes within the channel coinciding with the lines observed in the Excitation image.

Motivated by these observations, during this part of the thesis we focused the investigation in the spatial variation of CPD along the channel for the different OFET working regimes. The potential drops,

and therefore the resistance between domains in the crystalline films, have been studied. Moreover, the potential in the channel upon switching off the OFET gives us an insight on the charge trapping phenomena. By monitoring the temporal evaluation of the CPD, the charge dynamics were visualized.

7.2.1 Test for Au/MoO$_x$ electrodes on SiO$_2$

In order to understand the CPD maps on working OFETs, a previous characterization of the Au/MoO$_x$ electrodes evaporated on the SiO$_2$ substrate was made without the semiconducting film. This is a control test that serves to prove that the SiO$_2$ dielectric is free of charges and from ionic transport. Figure 7.20 (a) shows the topographic image two electrodes edges of a $\approx 20\mu$m channel in which MoO$_x$ / Au contacts were evaporated onto the SiO$_2$ substrate. It must be noted that the evaporation of both materials does not result in a steep edge, but in a non perpendicular edge formed by MoO$_x$ at the bottom and Au at the top. This strongly affects the KPFM images of the channel. In Figure
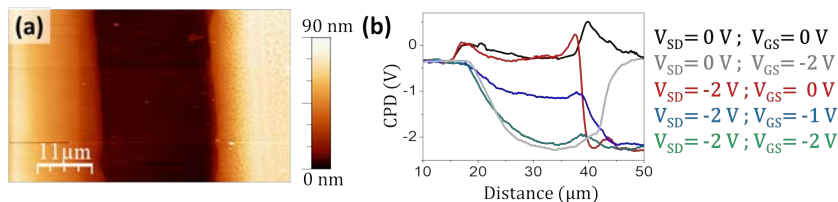
Fig. 7.20: (a) Topographic image and (c) CPD profiles for different V$_{GS}$ and V$_{SD}$ values.

7.20 (b) the CPD profiles taken for different V$_{GS}$ and V$_{SD}$ values. When V$_{GS}$=V$_{SD}$=0 (black profile), we observe that three different CPD values; the more external part of the electrode, with a CPD of ≈ 0.45V, a peak up to ≈ 0.1V in the electrode edge and ≈ 60 mV in the centre of the channel. These differences within the channel are probably due to the uncovered MoO$_x$, fact also supported by the tilted electrode edge that suggests shadowing during the metals evaporation. In general, the three different CPD values arise from the difference

between the materials work function (black line). When V_{SD} is increased to -2V (red profile), the potential in the drain electrode drops to that value as expected while the CPD value in the channel remains unchanged (close to zero volts). When a bias gate of - 2V is applied (green and grey profiles), the CPD follows the bias gate, as there are no injected charges to screen the bias. For example, the blue profile corresponds to the case when V_{GS}= -1 V and V_{SD}= -2 V and we can observe how, as expected, the measured CPD follows these values.

This behaviour is similar to the one reported in the previous section, for the 1:2 C8-BTBT:PS OFET. In that case, the semiconductor layer was not homogeneous enough to form the accumulation layer, so the observed CPD in the channel followed the applied V_{GS}. This experiment allows us to discard possible effects, such as charge accumulation on the gate dielectric that could affect the results obtained in the studied OFETs in this thesis.

7.2.2 CPD in the channel for the different working regimes.

In the first place, the behaviour of the channel depending on the gate voltage with grounded source and drain electrodes has been studied. Under operation, no changes in the CPD are expected upon negative gate bias, as the field effect would screen the applied potential. In a p-type OFET, for positive V_{GS}, the absence of accumulation channel would result in a direct observation of the applied gate voltage. This behaviour was already introduced in the previous section, and is here in detail analysed for a C8-BTBT:PS OFET (4:1 ratio) with Au/F4-TCNQ electrodes. In Figure 7.21 are shown the CPD maps of the same area, including the Source and Drain electrodes in the left and right parts respectively, for V_{SD} = 0 V. In (a) the gate voltage was stepwise changed from 0 to -40 V. No changes are observed evidencing the rapid formation of the accumulation layer of holes, that constantly
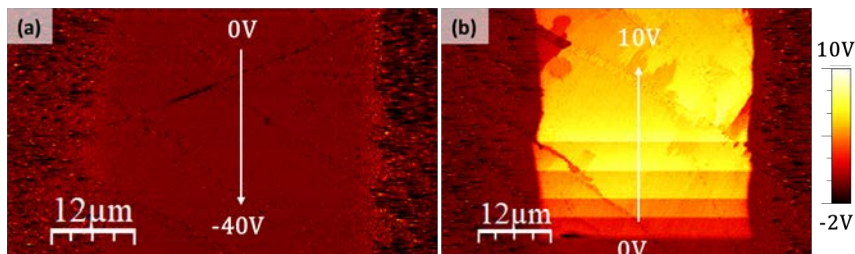
Fig. 7.21: CPD images adquired by KPFM of the channel of a C8-BTBT:PS OFET (4:1 ratio) with Au/F4-TCNQ contacts changing V_{GS} for negative (a) and positive (b) bias values for $V_{SD} = 0$ V. The arrow indicates the direction the sample is imaged.

screens the applied V_{GS}. On the contrary, for positive V_{GS} (Figure 7.21 (b)), the CPD in the channel briefly increases up to the applied gate bias and is slightly reduced shortly after stabilizing at a positive bias. This implies that not enough electrons are injected into the channel in order to screen the applied V_{GS}, as expected in a p-type OFET.

Once the formation of the channel has been checked, a V_{SD} of -5V was applied. In Figure 7.22 are shown the CPD images of the same area for different V_{GS}, going through the different working regimes. In (a), for $V_{GS} = 0$ V, where the OFET is in the off-state, most of the potential in the channel is nearly zero (as seen in the yellow profile in Figure 7.23). Surprisingly, close to the drain electrode, some areas (marked with white dashed rectangles) present the same potential as the applied drain bias (-5V). These areas display none correlation with topographical features. As the OFET is in the off-state, the negative CPD must arise from injected negative charges. Similarly, the adjacent domain (marked in blue), shows a CPD value of -2.8V, indicating as well a presence of negative charges. However, the limits of these domains are clearly defined and no charges seem to be injected in the rest of the channel. It is plausible that this behaviour is related with the presence of doped-grains due to the diffusion of F4-TCNQ into the channel. A charge transfer phenomena between the semiconductor
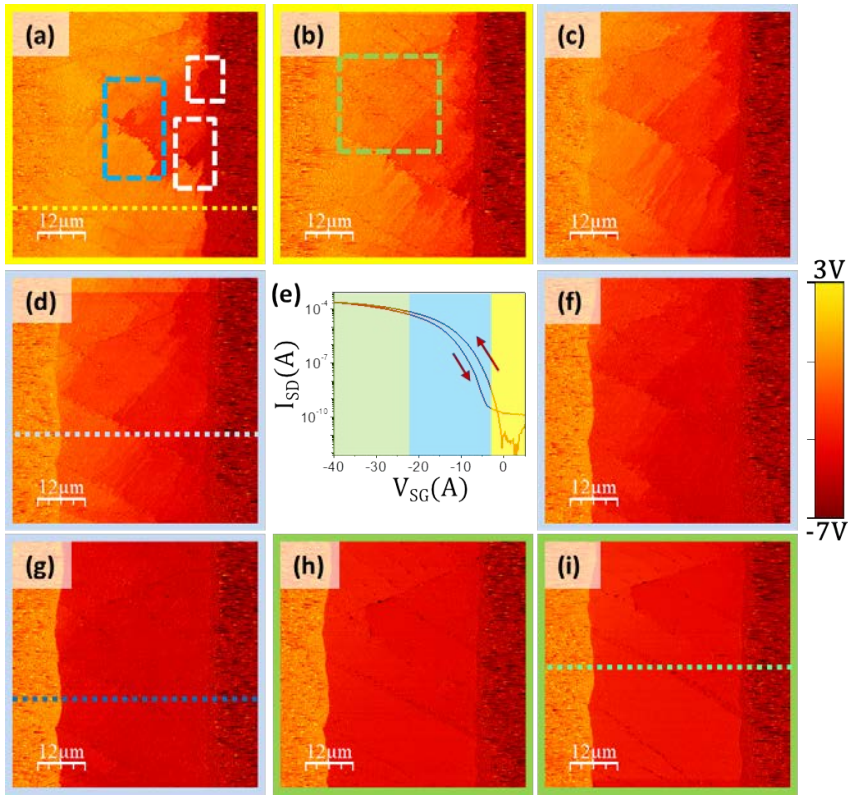
Fig. 7.22: CPD images taken in a C8-BTBT:PS OFET (4:1 ratio) with Au/F4-TCNQ contacts. Source and drain were all the time maintained at V_{SD} =-5V while the gate bias was changed: V_{GS} = 0 (a), V_{GS} = -2V (b), V_{GS} = -4V (c), V_{GS} = -6V (d), V_{GS} = -8V (f), V_{GS} = -10V (g), V_{GS} = -30V (h) and V_{GS} = -40V (i).

and F4-TCNQ as well as the diffusion of the latter in the semiconductor layer have been reported before [260, 261].

When the OFET is switched on, with V_{GS} < -2V, the adjacent region towards the source direction (marked in green in Figure 7.22 (b)) shows presence of charges as well, indicating that the conduction channel is being formed. Through (c), (d), (f) and (g), the OFET works in saturation regime. By increasing V $_{GS}$ the potential of the channel evolves towards a nearly linear decay between the two electrodes, with a steep potential drop at the source electrode edge, which can be attributed to a contact resistance arising from the charge
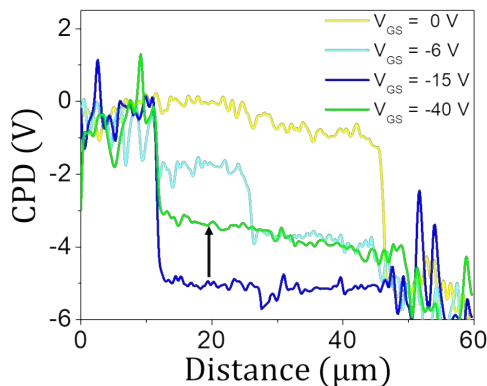
Fig. 7.23: CPD profiles marked in Figure 7.22, taken with V_{SD} =-5V and the indicated V $_{GS}$.

injection barrier in the source, as introduced in the previous section. Figure 7.23 displays the CPD profiles marked in Figure 7.22. In the blue profile in Figure 7.23 (d) a potential drop is also observed in the middle of the channel, corresponding to a domain boundary. In Figures 7.23 (f) and (g), the majority of the potential drops close to the source electrode, indicating a large electric field in that electrode.

When V_{GS} <-20V, and the OFET enters in the linear working regime region (marked in blue in the curve in (e)). In this situation, the potential drops in both drain and source electrodes. Because in the linear regime the accumulation channel of holes is homogeneously formed (black arrow in the profiles), one would expect a linear potential drop between the source and drain electrodes. However, the charge extraction barrier introduces a resistance at both electrodes, as commented in the previous section. Within the channel, the potential predominantly drops at some domain or grain boundaries.

7.2.3 Interdomain resistance

As observed in Figures 7.19 (d) and 7.23, the potential profile decreases stepwise along channel. This is due to the high conductance of the BTBT-C8 film, mainly disrupted some resistive boundaries. Grain

boundaries in OFETs have been widely studied, as they act as charge trapping centers that can have a detrimental effect in the charge mobility in the channel [109, 112, 254, 262].

In the studied C8-BTBT:PS films, a closer look reveals that some of these steps on the CPD image do not show any noticeable features in the Topography image, as seen in Figure 7.24 corresponding to a region close to the drain electrode in the off-state OFET. In the
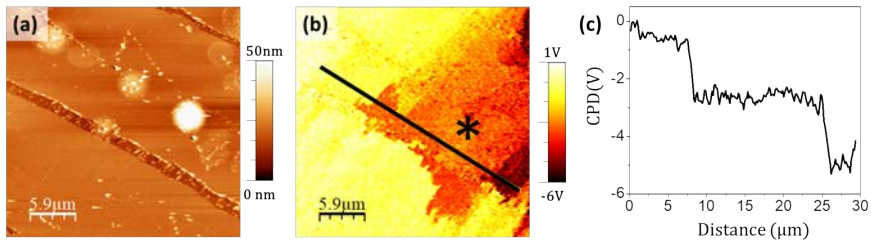
Fig. 7.24: Topography (a) and CPD (b) image of a detail in the channel marked with a blue dotted square in Figure 7.22 (a) taken with V_{SD} =-5V and V_{GS}=0V. (c) Profile marked in (b)

profile in (c), three different CPD values are clearly distinguished, whereas in the topographic image the film seems to be smooth, only exhibiting some parallel cracks. In the surface potential image, the darkest domain shows the same potential value as the biased drain electrode, and therefore must be electrically connected to it. The red domain (marked with a star) in the CPD image, however, is not directly connected to the drain neither to the source electrode while the yellow one shows the same potential than the source electrode. This seems to indicate that, although there are no visible domains in topography, there must be resistive boundaries between crystalline domains. It is unknown yet if there is a role played by the insulating PS underneath (see Section 7.1.3).

As shown in Figure 7.25, there are some areas, though, in which some features in topography coincide with the CPD image. In the profile in (c) it is evidenced how the potential drop coincides with an island in the Topography image (see Figure 7.5). The height
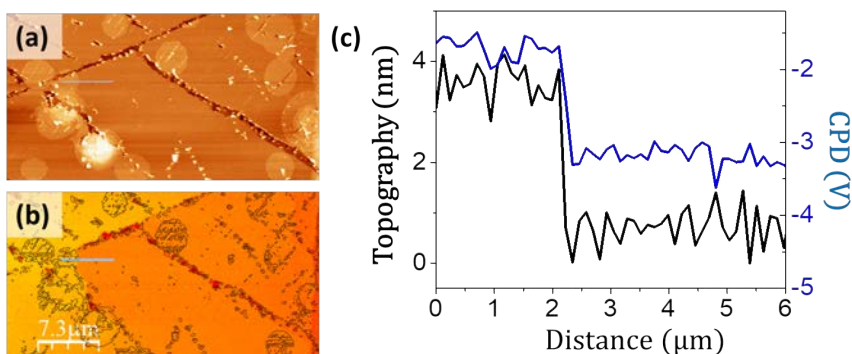
Fig. 7.25: Topography (a) and CPD (b) image of a detail in the channel taken with V_{SD} =-5V and V $_{GS}$=-40V. In (b) is shown the contour of the Topography image. (c) Profile marked in (b)

of the island coincides with the interplane distance of the C8-BTBT unit cell ($\approx 3nm$)[141]. Outstandingly, this island shows a different potential from the grain where it is located, while most of the observed islands show a potential value similar to the grain where they stand. Additionally, it is one of the observed grain boundaries with larger potential drop. We have examined the potential drop in Figure 7.25 (c) for different V $_{GS}$ values keeping drain voltage at -5V. Boundary resistance values (R_B) for the domain boundary in Figure 7.25 are extracted for the different values an plotted in Figure 7.26 (a).
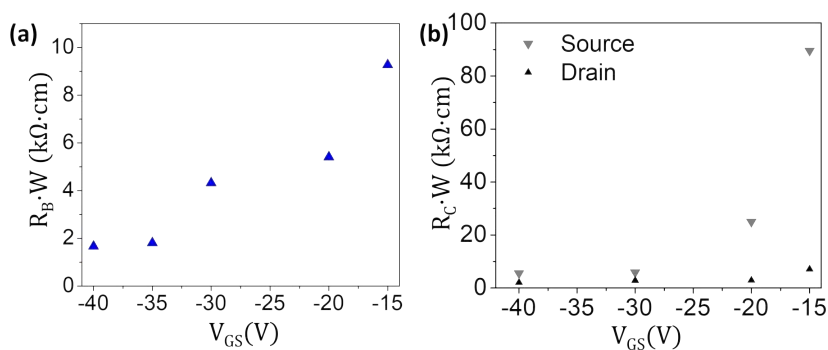
Fig. 7.26: Values of the extracted R_B (a) and R_C (b) for different V_{GS} from the grain boundary marked in Figure 7.25.

For bias higher than -15V, no resistance could be extracted either because of the similar potential in all the channel (in the saturation working regime) or barely measured currents. The R_B values clearly decrease with the applied gate voltage. This is consistent with the hypothesis that an electrostatic barrier arises at the domain boundaries due to the presence of charges. These trapped charges cause an energy barrier to hole transport that must be overcome. At higher V_{GS}, we observe how R_B decreases, and therefore the conductivity increases, indicating that the energy barrier is reduced. The decrease of the energy barrier for intergrain transport was reported by Kelley et al. in sexithiophene (6T) crystals [263]. The contact resistance values for both source and drain electrodes were also extracted and plotted in Figure 7.26 (b). We can observe how the contact resistance at the source (where the largest potential drop is observed) decreases two orders of magnitude for higher V_{GS}. This increase has been related an to increase of the charge density and has been reported before [53, 54, 264]. At low gate bias values, as observed in the yellow profile Figure 7.23 (a), the contact resistance becomes dominant and most of the potential falls at the source electrode.

It is noteworthy that the obtained resistances are at least one order of magnitude higher than the channel resistance estimated before ($R_{CH} \cdot W = 0.88 \ k\Omega \cdot cm$). Our hypothesis is that the low density of grain boundaries with significant resistance does not significantly affect the total channel resistance.

7.2.4 Charging and discharging dynamics

As introduced before, once the accumulation layer is formed, if the bias gate is turned off, the charges might remain in the channel, trapped in the film defects. This was clearly observed for some of the studied systems in this thesis. In this section are presented charge accumulation experiments done for three OFETs with different types of electrodes.

Au electrodes In a 4:1 ratio C8-BTBT OFET with Au contacts, we turned off the gate bias gradually while keeping both source and drain electrodes grounded. CPD values measured in the middle of the channel are plotted in Figure7.27 (b). The green points correspond to
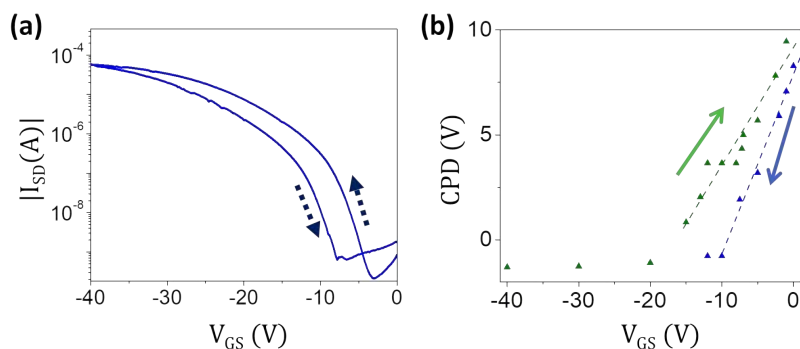
Fig. 7.27: (a) Transfer characteristic of the 4:1 ratio C8-BTBT OFET with Au contacts. (b) CPD values in the centre of the channel upon gate bias with V_{SD} =0V.

the situation when the gate bias is gradually increased from -40V to 0V in intervals of 4-5 minutes. Although for V_{GS}<-20V no changes are observed, beyond that value the CPD values become more positive until reaching a maximum value of 9.47 V when V_{GS} = 0V. This can be explained by a presence of holes in the film that are not discharged after the OFET has been switched off. A hole density value can be extracted in the channel from the expression $\sigma = C_i \cdot V_{CPD}/e$ where C_i is the SiO$_2$ 200 μm layer capacitance per area and e the electron charge [257, 265]. For V_{GS} = 0 V, the observed CPD corresponds to the trapped holes and a hole areal density of 1.05×10^{12} cm^{-2} can be extracted. Considering the unit cell of C8-BTBT, we can estimate an a charge density in the film volume of approx 10^3, i.e., one hole every thousand C8-BTBT molecules. Similar values have been observed for one monolayer pentacene OFETs [257]. The V_{TH} extraction from the transfer curves in Figure 7.27 (a) allows us to estimate a hole trap density of 4.5×10^{11} cm^{-2}. This value is very similar to the one calculated from the CPD value.

In fact, we can assume that the holes forming the accumulation channel experience two different phenomena: some of them leave rapidly the channel while others remain trapped leaving the film positively charged. Afterwards we have followed the evolution of the surface potential as a function of V_{GS} in the channel when the OFET is switched on again. The blue points in the Figure 7.27 (b) correspond to the CPD values when the gate bias is again negatively biased (blue arrow). It is noteworthy that both the on-to-off sweep (green dots) and the off-to-on sweep (blue dots) ways do not coincide. The effect of the hysteresis would be manifested in a shift in the V_{GS} at which the channel would screen the applied bias and the CPD would be zero. The transfer characteristic in Figure 7.27 (a) shows a BSC hysteresis, experiencing a shift in of $\Delta V_{TH} = 3.8V$ towards more negative bias in the back sweep. The hysteresis of ≈ 7.4 V in the CPD values does not completely correlate with the hysteresis in the devices. It must be noted that the sweeping speeds in the transfer characteristics are much faster than the changes in bias in the CPD experiment, and therefore the hole trapping dynamics can differ preventing to stablish a comparison in quantitative terms.

So far, we have proven the presence of traps for mobile charges (that cause the hysteresis both in the CPD and Transfer characteristics) and of fixed charges (that are at the origin of V_{TH}).

.

Au/TCNQ electrodes   Figure 7.28 shows the transfer characteristics of a 4:1 ratio C8-BTBT:PS OFET with Au/TCNQ contacts. As for the Au contacts, the BSC hysteresis in the curve suggests a charge trapping mechanism, either for electrons or holes or both. The V_{TH} value would correspond to a charge density of $\sigma = 4.7 \times 10^{11}$ cm^{-2}. Once again, charge trapping dynamics can be evaluated by consecutively measuring the potential decay when the transistor is switched off. Figure 7.29 shows two CPD images acquired after the V_{GS} is set to zero, the scanning direction is specified. In (a), after a $\approx$4 minutes at
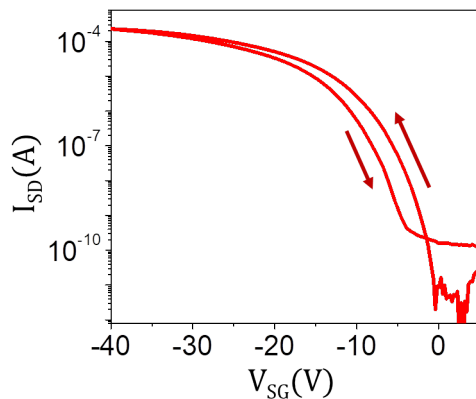
Fig. 7.28: Transfer characteristic for 4:1 ratio C8-BTBT:PS OFET with Au/TCNQ contacts with V_{SD} =-5V.

V_{GS}=-40V, V_{GS} was reset to 0 V. In the scanning line just after, the CPD in the channel reaches up to 6.13 V due to the trapped holes in the channel. The calculated hole accumulation density for this CPD value is of 6.8×10^{11} cm^{-2}, similar to the one extracted from V_{TH}.

With time, the potential slowly decays to 0 V and therefore the charge accumulation density fades away. This can be observed in the images in Figure 7.29. Upon scanning (the arrows indicate the slow scan direction), the potential slowly decreases until reaching 0 at V_{GS}=0. It is noteworthy that the channel is not homogeneously charged, but
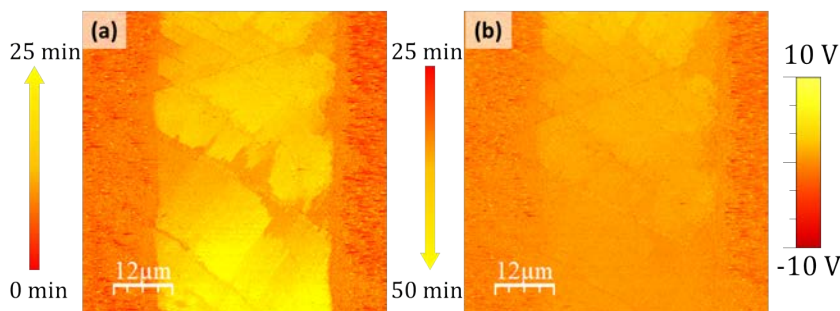
Fig. 7.29: CPD images taken right after setting V_{GS}=0 after applying V_{GS}=-40V in a 4:1 C8-BTBT:PS ratio OFET with Au/TCNQ contacts with grounded electrodes. The arrows indicate the slow scan direction.

some areas show differences up to 10V. Notice that the less-charged

areas (the darkest areas in Figure 7.29 (a)) can be identified as the electrically connected domains with the electrode in Figure 7.22 (a). This fact might indicate that, as these areas are electrically connected to the drain, the discharge is more favourable than for the rest of the film showing a much lower CPD value. However, another possible explanation can be that these particular zones correspond to areas in which the crystalline quality of the film is higher, presenting less defects that could act as trap centres for the charges.

In order to have a more realistic correlation with the hysteresis curves, a similar experiment is performed with V_{SD} =-5V bias applied. Figure 7.30 shows consecutive images of the channel a 4:1 ratio C8-BTBT:PS OFET with Au/TCNQ for V_{SD} =-5V. In (a), the OFET is working in the linear regime, with an applied V_{SG} of -40V, as observed in Figure 7.22 (i) as well. In (b), this voltage is turned off (yellow dotted line) and, as in the previous experiment, a positive CPD over 10 V is measured in the centre of the channel, as a result of the accumulated charges that no longer screen the applied V_{GS}. The hole charge accumulation layer is over $1.2 \times 10^{12} \text{cm}^{-2}$ and therefore higher than the one obtained for $V_{SD} = 0$ V.

Upon screening, the voltage fades away until the state presented in Figure 7.22 (a), with V_{GS}=0V and V_{SD} =-5V is fully recovered (Figure 7.30 (e)). Moreover, if V_{SD} is set to 0 (Figure 7.30 (f)), the CPD in the channel has the same value as the electrodes, indicating that the charges are no longer accumulated in the layer. The consecutive images allow us to estimate the time decay for the film to discharge the trapped charges and go back to the off state, Figure 7.31 shows the normalized CPD decay upon time for $V_{SD} = 0$ V (black) and in $V_{SD} = $ -5 V (blue). The plot in Figure 7.31 is similar for both, which implies that the electric field between source and drain is not contributing to quickly discharge the trapped holes in the channel, which is consistent with the existence of traps due to structural defects or grain boundaries in the film. The calculated decay time for both discharging processes is of ≈ 770s
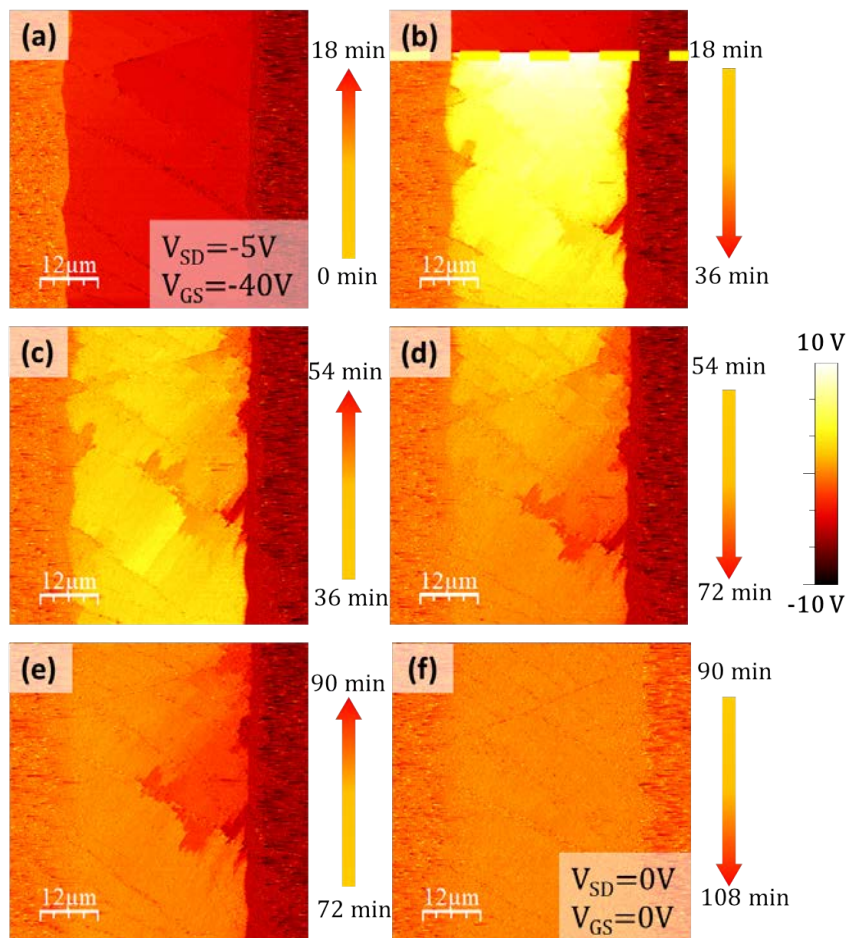
Fig. 7.30: CPD images taken right after setting $V_{GS}=0$, $V_{SD}=$ -5V in a 4:1 C8-BTBT:PS ratio OFET with Au/TCNQ contacts. The coloured arrows indicate the scan direction. As indicated, each image takes 18 minutes to be completed.

Au/MoO$_x$ contacts In the transfer curve in Figure 7.32 (e), for a 4:1 ratio C8-BTBT:PSOFET with Au/MoO$_x$ contacts, a lower BSC hysteresis is found. Figure 7.32 shows the CPD images taken consecutively of a detail in the centre of the channel with a -5V bias applied to the drain electrode. In (a), V_{GS} is set to -40V. In (b) the potential is switched off and during (c) and (d) the area consecutively is scanned. Differently from the OFET with Au/TCNQ contacts, in this case the CPD does not rise up to positive values as a result of a hole accumulation. Instead, it slowly rises up to the value corresponding to the
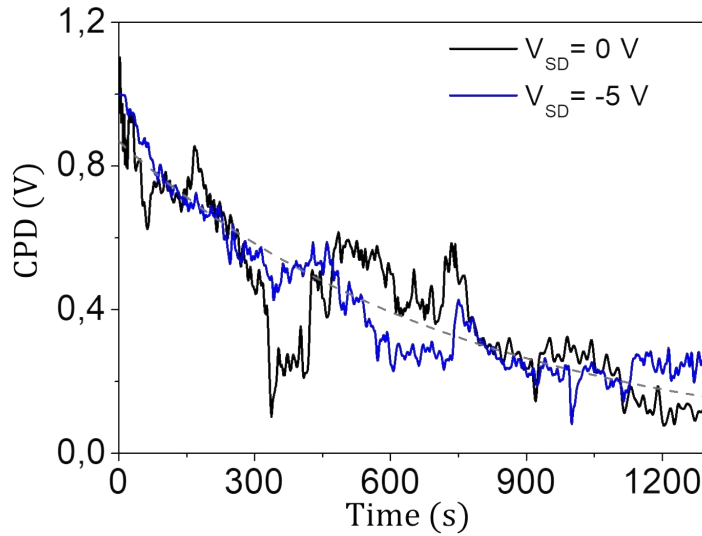
Fig. 7.31: Normalized CPD vs time plots taken right after setting V_{GS}=0 for V_{SD} = 0 V (black) and in V_{SD} = -5 V (blue) in a 4:1 ratio C8-BTBT:PS OFET with Au/TCNQ contacts. The exponential fit ($CPD \propto e^{-t/\tau}$) corresponds to the grey dashed line.

state with V_{GS}=0. This implies that, when V_{GS} is turned off, the accumulation layer is quickly released.

These KPFM experiments reveal that the selection of the contacts is of great importance; while with Au (Figure 7.27) and Au/TCNQ (Figure 7.30) the accumulated holes remain in the channel upon turning off the gate bias, when Au/MoO$_x$ is used, the channel seems to be quickly discharged of holes. One of mechanisms for which the CPD value in the channel would slowly go from negative bias to more positive ones would be the trapping of electrons in the channel, that would be discharged through images (b)-(c) in Figure 7.32 during $\approx$ 43 minutes. As explained above, the trapping of minority carriers would also produce a lower BSC current (Figure 7.17) and therefore would explain the transfer characteristics in Figure 7.32 (e).

As the OFET geometry is the same for all the devices, as well as the film composition and the gate dielectric, we can conclude that the Au/MoO$_x$ electrode favours the fast extraction of the holes that
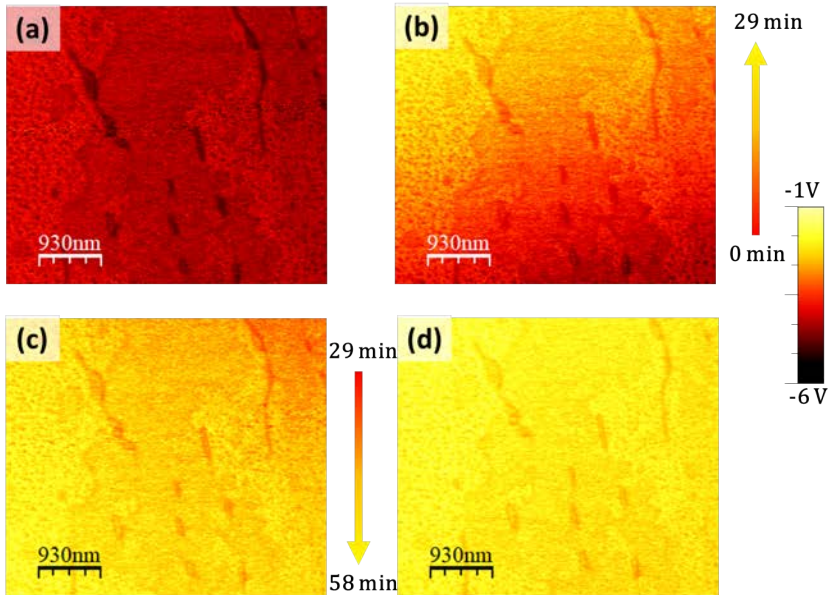
Fig. 7.32: CPD images taken (a) at V_{GS} = -40 and after setting V_{GS} = 0V (b), (c) and (d) in a 4:1 ratio C8-BTBT:PS OFET with Au/MoO$_x$ contacts. The coloured arrows indicate the slow scan direction. (e) Transfer curve of the device. The arrows indicate the bias sweeping direction.

form the accumulation layer. This can be explained by the more favourable energetic barrier at the C8-BTBT:Au/MoO$_x$ interface, that allows a faster extraction of charges. We can also hypothesize that the electron trapping occurs for all the electrodes, but that it is not clearly distinguished for the Au and Au/F4-TCNQ electrodes, as the amount of trapped holes dominates the CPD in the channel.

7.2.5 Minority carriers injection

In the previous section we have studied the role of trapping of the majority carriers, holes, for a p-type OFET. Now we will investigate the dynamic behaviour of carries for a n-type OFET, in which the channel is formed by accumulation of electrons when a positive V$_{GS}$ is applied.

Figure 7.33 shows the topographic (a) and CPD (b) images of a detail in the channel of a OFET in which the organic film is formed by the semiconducting molecule N,N0 - 1H,1H - perfluorobutyl - cyanop-erylenediimide (PDIF-CN$_2$). This molecule forms densely packed molecular crystals that have been reported to show air stability and field-effect mobilities up to 0.71cm^{2}V^{-1}s^{-1} [266, 267]. The contacts consist of Au deposited as described in the previous section in top-electrode configuration. A CPD image in which the same line,
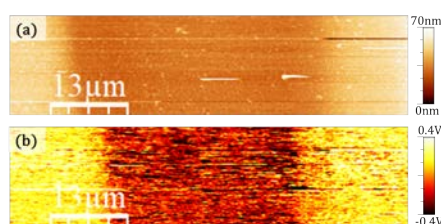
Fig. 7.33: Topographic (a) and CPD (b) images of a 50 μm channel PDIF-CN$_2$ OFET with grounded electrodes.

including both electrodes and the channel, is scanned for different V$_{GS}$ values is shown in Figure 7.34. The topographical profile on top indicates the electrodes edges.

When turning on the device, it must be noted that no significant changes are manifested upon positive gate bias. In this OFET, when the bias gate was turned off, the channel did not show a sudden CPD drop towards negative values, due to the accumulation of majority carriers (electrons in this case). However, for negative voltages below V_{ON}, the CPD suddenly drops towards negative values but rapidly decreases to approximately zero volts in an interval of seconds. This
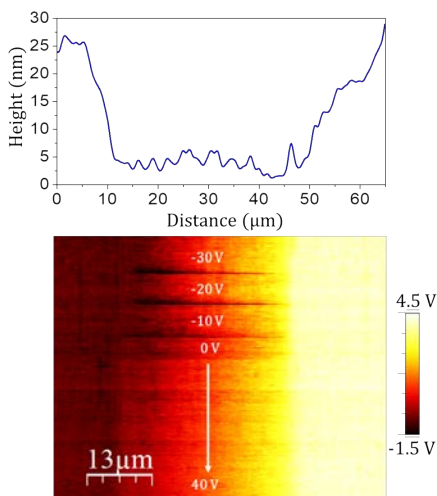
Fig. 7.34: Topographic profile and CPD images of a PDIF-CN$_2$ OFET upon changing gate bias with V_{SD} =-5V.

sudden drops and posterior recovery of the CPD in the channel can only be explained if the negative V_{GS} is during a short time visualized and then screened by holes injected into the channel. In order to explore this phenomena, in Figure 7.35 (a)the time evolution of the CPD measured a spot in the middle of the channel with grounded electrodes is plotted. The discharging from V_{GS} = -20V and V_{GS}=-30V was analysed. V_{TH} for this OFET was estimated to be -15V, so the applied V_{GS} would correspond to the off-state. As in Figure 7.34, although upon bias application the CPD experiences a sudden drop down to the drain voltage, the potential in the channel quickly increases till reaching the CPD values measured when V_{GS}=0. The calculated decay times are 36s when -30V is applied and 14s when -20V are applied to the gate, which is consistent with the larger amount

of holes that must be injected for higher V_{GS} values in order to screen the applied gate. This decay time is much slower than the sweeping speeds in the transfer characteristics, and therefore we can consider the holes to be trapped in the channel.
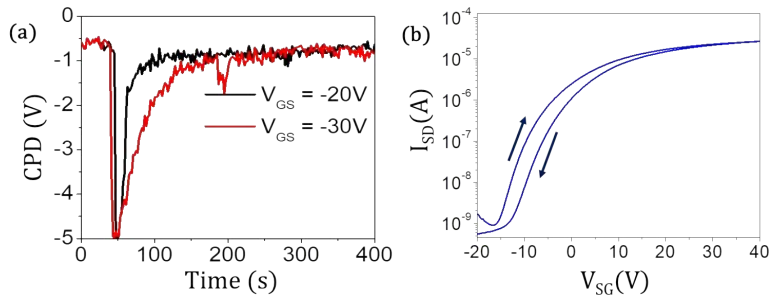
Fig. 7.35: (a) CPD evolution through time upon negative V_{GS} bias for $V_{SD}=0$V and (b) transfer characteristic of the device.

This hole injection upon negative bias below V_{ON} results in a screening of the applied V_{GS}. This process of minority carriers injected in the channel has been reported before in both p-type and n-type transistors [268, 269]. As we explained at the beginning of the section, the trapping of the minority carriers would result in a low BSC hysteresis in the transfer characteristics (Figure 7.17). Thus, the sense of the observed hysteresis in the transfer curve of the studied devices plotted in Figure 7.35 (b) would also correspond to a minority carrier (holes) accumulation within the channel. Although no systematic work was done, it seems plausible that for more negative V_{GS} values more holes must be injected from the electrodes requiring more time to screen the gate.

7.2.6 Conclusions

In this section we have used KPFM to visualize the CPD evolution in working OFETs. Through the different working regimes distinguished in the transfer characteristics, we have understood the potential drop in 4:1 ratio C8-BTBT:PS OFET with Au/TCNQ electrodes, concluding

that the charge transport in these devices is significantly limited by the contact resistance and, with much less impact, by the grain boundaries. The behaviour of the grain boundaries was also studied, extracting the inter domain resistance for different gate bias. Some of the potential drops coincide with topographic features, while some others do not, preventing us of making a correlation between the grain resistance and the structural defects in the film. Comparing the inter-domain resistance with the contact resistance we conclude that the latter is dominant for the device transport and that the low density of grain boundaries does not have a relevant impact in the low channel resistance indicating a very good crystallinity of the film

The charge and discharge dynamics were studied for 4:1 ratio C8-BTBT:PS OFETs with three different electrodes: Au, Au / TCNQ and Au / MoO_x. For the first two, a clear majority charges trapping was observed, giving a plausible explanation for the BSC hysteresis and the V_{TH} value in the device. For the Au/MoO_x, we suggest that the holes quickly leave the channel and that the predominant phenomena is the electron trapping, which also correlates with the hysteresis in these devices. The faster charge extraction for Au/MoO_x electrodes is possibly related to the more favourable energy level configuration at the electrode/film interface. In PDIF-CN_2 this was again observed, as injection of the minority carriers (holes) was visualized in the time evolution of the CPD during the discharge of the channel. The proposed hole trapping hypothesis is supported by the BSC hysteresis in the transfer curve of the device.

The KPFM experiments are sensitive to both the mobile and fixed trapped charges that play a role in V_{TH} and in the hysteresis in the device characteristics, making difficult to distinguish between the trapped charges behind these effects. Thus, it would be of great interest to design systematic KPFM experiments to study the charge dynamics in the OFETs.

Conclusions

8

8.1 Summary

By means of different SPM techniques we have studied different inter-faces and crystalline systems present in organic solar cells (OSCs) and organic field effect transistors (OFETs). The major goal was to corre-late the investigation at the nanoscale with the device performance. In the following, the main conclusions of this thesis will be listed.

As Transverse Shear Microscopy has proven to reveal interesting struc-tural features in organic crystalline films, a systematic study using a submonolayer of PTCDI-C8 as a benchmark was performed in order to gain knowledge about the physical phenomena behind it. The main conclusions of this study were:

- The underlying phenomena of TSM is the stick-slip response to the tip when interacting with a periodic surface potential. Thus, as FFM, TSM has a dissipative origin. Moreover, we have proven that the Prandtl-Tomilson model extended to two dimensions reproduces the experimental FFM and TSM data at a molecular scale.

- TSM was used to characterize ultrathin PTCDI-C8 crystalline films grown by consecutively scanning the same area, revealing that although intra-layer boundaries are created, the new layers assemble in registry with the underlying one, achieving a good 3D crystalline order.

In organic solar cells, we have focused on both the crystalline structure and the interface between the active layer and the electrodes. Concerning the interface between the active layer and the anode, the main conclusions are the following:

- By means of KPFM, contact angle and C-AFM, we have proven that phosphonic acid SAMs increase the ITO workfunction as expected. However, when employed in cells with structure ITO/SAM/PBDTTT-CF:PC$_{71}$BM, strong extraction problems are manifested in s.shaped curves. A C-AFM study of the surface reveals inhomogeneous conductivity, which might lead to a charge accumulation at the interface. This hypothesis was supported by an analysis of the s.shaped J-V characteristics with the Mazhari model, that reveals that the recombination is dramatically increased at higher illumination intensities. Therefore, the employed SAMs are not suitable as HTL in high efficient OSCs.

- In perovskite solar cells with structure FTO / d-TiO$_2$ / CsFAMAPbIBr / HTM/Au, we have explored the causes of the unexpected low V$_{OC}$ when using the diarylamino-substituted tetraarylethene-based molecule (TAE-1) instead of the well known spiro-OMeTAD. The recombination dynamics at the interface were proven to be similar for both devices. Work function measurements by KPFM reveal that the smaller change shift of its HOMO towards the VBM of the perovskite in TAE-1 when casted on the perovskite leads to a less favourable alignment of the energy levels compared to the spiro-OMeTAD, which would explain the lower V$_{OC}$ values experimentally obtained. This result is of relevance in order to guide the molecular design of HTL in perovskite solar cells.

Regarding the role of the active layer morphology in A-D-A oligomers:fullerene OSCs, we have concluded that:

- For oligomer 1, the better photovoltaic properties than oligomer 2 before the solvent vapour annealing (SVA) treatment are explained by the better crystallinity, allowing the π-π organization of the oligomers during drying. Upon SVA, the little improvement in the cells parameters is explained by the absence of major structural changes.

- For oligomer 2, the GIWAXS experiments show a hindered development of the π-π stacking in the as-casted films, which seems to be caused by the steric hindrance due to the inner position of the hexyl side chains, that enable a larger interaction with the solvent molecules. Upon SVA, the π-π crystallization is enhanced. By a combined study with AFM, PL and SIMS, we have proven that the fullerene component is segregated in bigger domains and that the vertical composition changes in a beneficial way, creating an oligomer-poor layer at the cathode and an oligomer-rich layer at the anode. Thus, it can be concluded that the inner positioned hexyl chains in isomer 2 allow the diffusion and rearrangement of the molecules upon SVA in a more favourable nanomorphology. This result can lead to more efficient strategies for the design of A-D-A oligomers for high efficient OSCs.

For the OFETs investigation by FFM and KPFM, the main conclusions are:

- By a FFM analysis we conclude that the vertical structure of C8-BTBT:PS films grown from solution by BAMs consists of a C8-BTBT crystalline layer sandwiched between a bottom and an ultra-thin skin PS layer on the top. The thickness and lateral continuity of the film depends on the blend composition ratio. This stratified structure determines the device properties in the following ways:

– The PS layers play a fundamental role in the stability of the film, impeding the dewetting through time.

– By performing KPFM in operando OFETs it is revealed that the thickness and continuity of the C8-BTBT layer play a fundamental role in the accumulation channel formation.

- The contact resistance is the critical factor in the devices performance, which is improved by doping the contacts with F4-TCNQ. If the contact resistance is excluded, the channel shows excellent hole transport properties, achieving a mobility of $\mu_{CH} \approx 10 \pm 1 \text{cm}^2\text{V}^{-1}\text{s}^{-1}\text{cm}^{-1}$.

- KPFM is a powerful technique that allows us to visualize the channel potential for the different OFET working regimes in a 4:1 ratio C8-BTBT:PS OFET with Au/TCNQ electrodes concluding that the potential drop between different C8-BTBT domains results in a resistance dependant on the gate bias. This dependence is consistent with the hypothesis of an electrostatic barrier for holes.

- The presence of trapped charges can be observed by KPFM when turning off the gate bias, as a positive CPD is measured in the channel. Comparing C8-BTBT:PS devices with A/F4-TCNQ and Au contacts, we observe that these fixed charges are at the origin of V_{TH}. In the Au contacts device, an hysteresis cycle is as well observed in the CPD when the OFET is turned off and on, which correlates with the transfer characteristic hysteresis. The electrodes play a determinant role in the injection of carriers.

- In a PDIF-CN$_2$ OFET (p-type), injection of minority carriers (holes) is observed. For the minority carriers, the calculated time decays increase for higher gate bias and it is of $\approx$14 s for V_{GS}=-20V.

8.2 Outlook

The performed studies on the active layer/electrode interface in organic solar cells reveal that the ITO electrical lateral heterogeneity can cause charge accumulation with a detrimental effect in the device. Thus, it seems that new hole transport layer materials that increase the ITO work function as well as electrically connect the conductive areas are still needed in order to substitute the widely used PEDOT:PSS.

Another perspectives of this thesis is combining the information gained by FFM and TSM about the crystallinity of the organic film in OFETs with the potential maps obtained by KPFM. The correlation between the different azimuthal orientations and the CPD drops could be of fundamental importance to understand the more favourable molecular orientations and therefore help to design new strategies for fabricating more efficient OFETs. Additionally, KPFM has been proven to be a powerful technique for extracting the local contact resistance, that could lead to the design of less resistive electrodes. The local evaluation of the CPD values upon formation of the accumulation channel would provide insight about the charge trapping mechanisms. Moreover, increasing the KPFM feedback speeds in order to get temporal resolution during a transfer characteristic of the device would allow us to distinguish between the different trapping mechanisms that affect both the hysteresis and V_{TH} of the devices.

Bibliography

[1] G. M. Whitesides, B. Grzybowski, "Self-Assembly at All Scales", *Science* **2002**, *295*, 2418–2421.

[2] J. D. Halley, D. A. Winkler, "Consistent concepts of self-organization and self-assembly", *Complexity* **2008**, *14*, 10–17.

[3] F. Schreiber, "Self-assembled monolayers: from 'simple' model systems to biofunctionalized interfaces", *Journal of Physics: Condensed Matter* **2004**, *16*, R881.

[4] D. Witt, R. Klajn, P. Barski, B. A. Grzybowski, "Applications, properties and synthesis of ω-functionalized n-alkanethiols and disulfides-the building blocks of self-assembled monolayers", *Current Organic Chemistry* **2004**, *8*, 1763–1797.

[5] J. C. Love, L. A. Estroff, J. K. Kriebel, R. G. Nuzzo, G. M. Whitesides, "Self-Assembled Monolayers of Thiolates on Metals as a Form of Nanotechnology", *Chemical Reviews* **2005**, *105*, PMID: 15826011, 1103–1170.

[6] L. Duan, J. Qiao, Y. Sun, Y. Qiu, "Strategies to Design Bipolar Small Molecules for OLEDs: Donor-Acceptor Structure and Non-Donor-Acceptor Structure", *Advanced Materials* **2011**, *23*, 1137–1144.

[7] M. Mas-Torrent, C. Rovira, "Novel small molecules for organic field-effect transistors: towards processability and high performance", *Chemical Society Reviews* **2008**, *37*, 827.

[8] G. Horowitz, R. Hajlaoui, H. Bouchriha, R. Bourguiga, M. Hajlaoui, "Concept of 'threshold voltage' in organic field-effect transistors", *Advanced Materials* **1998**, *10*, 923–927.

[9]   K. Lu, J. Yuan, J. Peng, et al., "New solution-processable small molecules as hole-transporting layer in efficient polymer solar cells", *Journal of Materials Chemistry A* **2013**, *1*, 14253.

[10]   G. Witte, C. Wöll, "Growth of aromatic molecules on solid substrates for applications in organic electronics", *Journal of Materials Research* **2011**, *19*, 1889–1916.

[11]   J. Koenigsberger, K. Schilling, "Über Elektrizitätsleitung in festen Elementen und Verbindungen. I. Minima des Widerstandes, Prüfung auf Elektronenleitung, Anwendung der Dissoziationsformeln", *Annalen der Physik* **1910**, *337*, 179–230.

[12]   M. Volmer, "Different Photoelectric Phenomena in Anthracene, their Relation to one another, to Fluorescence and to the Formation of Dianthracene", *Annalen der Physik* **1913**, *40*, 775–96.

[13]   C. K. Chiang, C. R. Fincher, Y. W. Park, et al., "Electrical Conductivity in Doped Polyacetylene", *Phys. Rev. Lett.* **1977**, *39*, 1098–1101.

[14]   C. W. Tang, "Two-layer organic photovoltaic cell", *Applied Physics Letters* **1986**, *48*, 183–185.

[15]   G. Horowitz, D. Fichou, X. Peng, Z. Xu, F. Garnier, "A field-effect transistor based on conjugated alpha-sexithienyl", *Solid State Communications* **1989**, *72*, 381 –384.

[16]   C. A. J. J. H. Burroughes, R. H. Friend, "New semiconductor device physics in polymer diodes and transistors", *Nature* **1988**, *335*, 137–141.

[17]   W. Brütting, "Physics of Organic Semiconductors" in *Physics of Organic Semiconductors*, 2005 WILEY-VCH Verlag GmbH Co. KGaA, **2005**.

[18]   G. Li, R. Zhu, Y. Yang, "Polymer solar cells", *Nature Photonics* **2012**, *6*, 153–161.

[19]   H. Kallmann, M. Pope, "Photovoltaic Effect in Organic Crystals", *The Journal of Chemical Physics* **1959**, *30*, 585–586.

[20]   G. Yu, J. Gao, J. C. Hummelen, F. Wudl, A. J. Heeger, "Polymer Photovoltaic Cells: Enhanced Efficiencies via a Network of Internal Donor-Acceptor Heterojunctions", *Science* **1995**, *270*, 1789–1791.

[21]   N. Marinova, S. Valero, J. L. Delgado, "Organic and perovskite solar cells: Working principles, materials and interfaces", *Journal of Colloid and Interface Science* **2017**, *488*, 373 –389.

[22] C. J. Brabec, M. Heeney, I. McCulloch, J. Nelson, "Influence of blend microstructure on bulk heterojunction organic photovoltaic performance", *Chem. Soc. Rev.* **2011**, *40*, 1185–1199.

[23] A. K. K. Kyaw, D. H. Wang, V. Gupta, et al., "Efficient Solution-Processed Small-Molecule Solar Cells with Inverted Structure", *Advanced Materials* **2013**, *25*, 2397–2402.

[24] F. A. S. Lima, M. J. Beliatis, B. Roth, et al., "Flexible ITO-free organic solar cells applying aqueous solution-processed V2O5 hole transport layer: An outdoor stability study", *APL Materials* **2016**, *4*, 026104.

[25] S. Holliday, R. S. Ashraf, A. Wadsworth, et al., "High-efficiency and air-stable P3HT-based polymer solar cells with a new non-fullerene acceptor", *Nature Communications* **2016**, *7*, 11585.

[26] K. Zhao, O. Wodo, D. Ren, et al., "Vertical Phase Separation in Small Molecule:Polymer Blend Organic Thin Film Transistors Can Be Dynamically Controlled", *Advanced Functional Materials* **2016**, n/a–n/a.

[27] Y. Lin, F. Zhao, Y. Wu, et al., "Mapping Polymer Donors toward High-Efficiency Fullerene Free Organic Solar Cells", *Advanced Materials* **2017**, *29*, 1604155, 1604155–n/a.

[28] J. Min, Y. N. Luponosov, C. Cui, et al., "Evaluation of Electron Donor Materials for Solution-Processed Organic Solar Cells via a Novel Figure of Merit", *Advanced Energy Materials* **2017**, 1700465, 1700465–n/a.

[29] Z. Yin, J. Wei, Q. Zheng, "Interfacial Materials for Organic Solar Cells: Recent Advances and Perspectives", *Advanced Science* **2016**, *3*, 1500362, 1500362–n/a.

[30] R. Steim, F. R. Kogler, C. J. Brabec, "Interface materials for organic solar cells", *Journal of Materials Chemistry* **2010**, *20*, 2499.

[31] S. Braun, W. R. Salaneck, M. Fahlman, "Energy-Level Alignment at Organic/Metal and Organic/Organic Interfaces", *Advanced Materials* **2009**, *21*, 1450–1472.

[32] X. Yu, T. J. Marks, A. Facchetti, "Metal oxides for optoelectronic applications", *Nature Materials* **2016**, *15*, 383–396.

[33] M. He, M. Wang, C. Lin, Z. Lin, "Optimization of molecular organization and nanoscale morphology for high performance low bandgap polymer solar cells.", *Nanoscale* **2014**, *6*, 3984–94.

[34] D. W. Zhao, P. Liu, X. W. Sun, et al., "An inverted organic solar cell with an ultrathin Ca electron-transporting layer and MoO3 hole-transporting layer", *Applied Physics Letters* **2009**, *95*, 153304.

[35] W. R. Lindemann, W. Wang, F. Fungura, et al., "The effect of cesium carbonate on 1-(3-methoxycarbonyl)propyl-1-phenyl[6,6]C61 aggregation in films", *Applied Physics Letters* **2014**, *105*, 191605.

[36] Y. Hong, S. Chen, C. W. T. Leung, et al., "Fluorogenic Zn(II) and Chromogenic Fe(II) Sensors Based on Terpyridine- Substituted Tetra phenylethenes with Aggregation -Induced Emission Characteristics", *ACS Applied Materials & Interfaces* **2011**, *3*, PMID: 21834577, 3411–3418.

[37] J. Liu, M. Durstock, L. Dai, "Graphene oxide derivatives as hole- and electron-extraction layers for high-performance polymer solar cells", *Energy Environ. Sci.* **2014**, *7*, 1297–1306.

[38] D. H. Wang, J. K. Kim, J. H. Seo, et al., "Transferable Graphene Oxide by Stamping Nanotechnology: Electron-Transport Layer for Efficient Bulk-Heterojunction Solar Cells", *Angewandte Chemie International Edition* **2013**, *52*, 2874–2880.

[39] H. C. Liao, C. C. Ho, C. Y. Chang, et al., "Additives for morphology control in high-efficiency organic solar cells", *Materials Today* **2013**, *16*, 326–336.

[40] H.-L. Yip, A. K.-Y. Jen, "Recent advances in solution-processed interfacial materials for efficient and stable polymer solar cells", *Energy Environ. Sci.* **2012**, *5*, 5994–6011.

[41] R. Po, C. Carbonera, A. Bernardi, N. Camaioni, "The role of buffer layers in polymer solar cells", *Energy & Environmental Science* **2011**, *4*, 285.

[42] P. Hotchkiss, S. Jones, S. Paniagua, et al., "The Modification of Indium Tin Oxide with Tuning of Surface Properties, and Potential for Use in Organic Electronic Applications", *Accounts of Chemical Research* **2012**, *45*, 337–346.

[43] A. Sharma, A. Haldi, W. J. Potscavage Jr., et al., "Effects of surface modification of indium tin oxide electrodes on the performance of molecular multilayer organic photovoltaic devices", *Journal of Materials Chemistry* **2009**, *19*, 5298.

[44] E. L. Ratcliff, A. Garcia, S. a. Paniagua, et al., "Investigating the influence of interfacial contact properties on open circuit voltages in organic photovoltaic performance: Work function versus selectivity", *Advanced Energy Materials* **2013**, *3*, 647–656.

[45] X. Bulliard, S.-G. Ihn, S. Yun, et al., "Enhanced Performance in Polymer Solar Cells by Surface Energy Control", *Advanced Functional Materials* **2010**, *20*, 4381–4387.

[46] N. Beaumont, I. Hancox, P. J. Sullivan, R. a. Hatton, T. S. Jones, "Increased efficiency in small molecule organic photovoltaic cells through electrode modification with self-assembled monolayers", **2011**, 1708–1711.

[47] M. Wang, I. G. Hill, "Fluorinated alkyl phosphonic acid SAMs replace PEDOT:PSS in polymer semiconductor devices", *Organic Electronics* **2012**, *13*, 498–505.

[48] C. K. Song, A. C. White, L. Zeng, et al., "Systematic investigation of organic photovoltaic cell charge injection/performance modulation by dipolar organosilane interfacial layers.", *ACS applied materials & interfaces* **2013**, *5*, 9224–40.

[49] M. Song, J.-W. Kang, D.-H. Kim, et al., "Self-assembled monolayer as an interfacial modification material for highly efficient and air-stable inverted organic solar cells", *Applied Physics Letters* **2013**, *102*, 143303.

[50] J. Zaumseil, H. Sirringhaus, "Electron and Ambipolar Transport in Organic Field-Effect Transistors", *Chemical Reviews* **2007**, *107*, PMID: 17378616, 1296–1323.

[51] G. Horowitz, "Organic thin film transistors: From theory to real devices", *Journal of Materials Research* **2004**, *19*, 1946–1962.

[52] D. Gupta, M. Katiyar, D. Gupta, "Mobility estimation incorporating the effects of contact resistance and gate voltage dependent mobility in top contact organic thin film transistors", *Proceedings of ASID* **2006**, 425–428.

[53] K. P. Puntambekar, P. V. Pesavento, C. D. Frisbie, "Surface potential profiling and contact resistance measurements on operating pentacene thin-film transistors by Kelvin probe force microscopy", *Applied Physics Letters* **2003**, *83*, 5539–5541.

[54] L. Bürgi, T. J. Richards, R. H. Friend, H. Sirringhaus, "Close look at charge carrier injection in polymer field-effect transistors", *Journal of Applied Physics* **2003**, *94*, 6129–6137.

[55] L. Bürgi, H. Sirringhaus, R. H. Friend, "Noncontact potentiometry of polymer field-effect transistors", *Applied Physics Letters* **2002**, *80*, 2913–2915.

[56] D. Natali, M. Caironi, "Charge injection in solution-processed organic field-effect transistors: Physics, models and characterization methods", *Advanced Materials* **2012**, *24*, 1357–1387.

[57] C. Liu, Y. Xu, Y. Y. Noh, "Contact engineering in organic field-effect transistors", *Materials Today* **2015**, *18*, 79–96.

[58] C. Kagan, D. Mitzi, C. Dimitrakopoulos, "Organic-inorganic hybrid materials as semiconducting channels in thin-film field-effect transistors", *Science* **1999**, *286*, 945–947.

[59] A. Kojima, K. Teshima, Y. Shirai, T. Miyasaka, "Organometal halide perovskites as visible-light sensitizers for photovoltaic cells", *Journal of the American Chemical Society* **2009**, *131*, 6050–6051.

[60] H. J. Snaith, "Perovskites: the emergence of a new era for low-cost, high-efficiency solar cells", *The Journal of Physical Chemistry Letters* **2013**, *4*, 3623–3630.

[61] D. Liu, T. L. Kelly, "Perovskite solar cells with a planar heterojunction structure prepared using room-temperature solution processing techniques", *Nature photonics* **2014**, *8*, 133.

[62] P. J. Hotchkiss, H. Li, P. B. Paramonov, et al., "Modification of the Surface Properties of Indium Tin Oxide with Benzylphosphonic Acids: A Joint Experimental and Theoretical Study", *Advanced Materials* **2009**, *21*, 4496–4501.

[63] J. L. Wilbur, A. Kumar, H. A. Biebuyck, E. Kim, G. M. Whitesides, "Microcontact printing of self-assembled monolayers: applications in microfabrication", *Nanotechnology* **1996**, *7*, 452.

[64] R. K. Smith, P. A. Lewis, P. S. Weiss, "Patterning self-assembled monolayers", *Progress in Surface Science* **2004**, *75*, 1 –68.

[65] A. Kumar, G. M. Whitesides, "Features of gold having micrometer to centimeter dimensions can be formed through a combination of stamping with an elastomeric stamp and an alkanethiol "ink" followed by chemical etching", *Applied Physics Letters* **1993**, *63*, 2002–2004.

[66] S. E. Koh, K. D. McDonald, D. H. Holt, et al., "Phenylphosphonic acid functionalization of indium tin oxide: surface chemistry and work functions.", *Langmuir : the ACS journal of surfaces and colloids* **2006**, *22*, 6249–6255.

[67] L. E. Scriven, "Physics and Applications of DIP Coating and Spin Coating", *MRS Proceedings* **1988**, *121*.

[68] H. C. Liao, C. C. Ho, C. Y. Chang, et al., "Additives for morphology control in high-efficiency organic solar cells", *Materials Today* **2013**, *16*, 326–336.

[69] V. D. Mihailetchi, L. J. A. Koster, P. W. M. Blom, "Effect of metal electrodes on the performance of polymer:fullerene bulk heterojunction solar cells", *Applied Physics Letters* **2004**, *85*, 970–972.

[70] C. J. Brabec, S. E. Shaheen, C. Winder, N. S. Sariciftci, P. Denk, "Effect of LiF/metal electrodes on the performance of plastic solar cells", *Applied Physics Letters* **2002**, *80*, 1288–1290.

[71] M. Schwoerer, H. Wolf, *Organic Molecular Solids*, Wiley, **2008**.

[72] F. G. Del Pozo, S. Fabiano, R. Pfattner, et al., "Single crystal-like performance in solution-coated thin-film organic field-effect transistors", *Advanced Functional Materials* **2016**, *26*, 2379–2386.

[73] A. S. Dimitrov, K. Nagayama, "Continuous Convective Assembling of Fine Particles into Two-Dimensional Arrays on Solid Surfaces", *Langmuir* **1996**, *12*, 1303–1311.

[74] G. Binnig, C. F. Quate, C. Gerber, "Atomic Force Microscope", *Phys. Rev. Lett.* **1986**, *56*, 930–933.

[75] J. Israelachvili, *Intermolecular and Surface Forces*, Elsevier Science, **2015**.

[76] H.-J. Butt, B. Cappella, M. Kapp, "Force measurements with the atomic force microscope: Technique, interpretation and applications", *Surface Science Reports* **2005**, *59*, 1 –152.

[77] R. W. Carpick, M Salmeron, "Scratching the Surface: Fundamental Investigations of Tribology with Atomic Force Microscopy", *Chem. Rev.* **1997**, *97*, 1163–1194.

[78] A. L. Weisenhorn, P. K. Hansma, T. R. Albrecht, C. F. Quate, "Forces in atomic force microscopy in air and water", *Applied Physics Letters* **1989**, *54*, 2651–2653.

[79]   F. J. Giessibl, "Advances in atomic force microscopy", *Rev. Mod. Phys.* **2003**, *75*, 949–983.

[80]   R. Garcıa, R. Pérez, "Dynamic atomic force microscopy methods", *Surface Science Reports* **2002**, *47*, 197 –301.

[81]   R. Bennewitz, "Friction Force Microscopy" in *Fundamentals of Friction and Wear*, (Eds.: E. Gnecco, E. Meyer), Springer Berlin Heidelberg, Berlin, Heidelberg, **2007**, pp. 1–14.

[82]   D. F. Ogletree, R. W. Carpick, M. Salmeron, "Calibration of frictional forces in atomic force microscopy", *Review of Scientific Instruments* **1996**, *67*, 3298–3306.

[83]   C. D. Frisbie, L. F. Rozsnyai, A. Noy, M. S. Wrighton, C. M. Lieber, "Functional Group Imaging by Chemical Force Microscopy", *Science* **1994**, *265*, 2071–2074.

[84]   R. M. Overney, E. Meyer, J. Frommer, et al., "Friction measurements on phase-separated thin films with a modified atomic force microscope", *Nature* **1992**, *359*, 133 –135.

[85]   R. Carpick, Q. Dai, D. Ogletree, M. Salmeron, "Friction force microscopy investigations of potassium halide surfaces in ultrahigh vacuum: structure, friction and surface modification", *Tribology Letters* **1998**, *5*, 91–102.

[86]   H. Hölscher, A. Schirmeisen, U. D. Schwarz, "Principles of atomic friction: from sticking atoms to superlubric sliding.", *Philosophical transactions Royal Society* **2008**, *366*, 1383–1404.

[87]   S. Morita, S. Fujisawa, Y. Sugawara, "Spatially quantized friction with a lattice periodicity", *Surface Science Reports* **1996**, *23*, 1–41.

[88]   E Gnecco, R Bennewitz, T Gyalog, E Meyer, "Friction experiments on the nanometre scale", *Journal of Physics-Condensed Matter* **2001**, *13*, 619–642.

[89]   J. A. Last, M. D. Ward, "Electrochemical annealing and friction anisotropy of domains in epitaxial molecular films", *Advanced Materials* **1996**, *8*, 730–733.

[90]   K. Puntambekar, J. Dong, G. Haugstad, C. Frisbie, "Structural and Electrostatic Complexity at a Pentacene/Insulator Interface", *Advanced Functional Materials* **2006**, *16*, 879–884.

[91]   S. Kalinin, A. Gruverman, *Scanning Probe Microscopy: Electrical and Electromechanical Phenomena at the Nanoscale*, Springer New York, **2007**.

[92]   Nanotec, Nanotec Electrónica.

[93]   Bruker Corporation, Bruker.

[94]   W. A. Zisman, "A NEW METHOD OF MEASURING CONTACT PO-
        TENTIAL DIFFERENCES IN METALS", *Review of Scientific Instru-
        ments* **1932**, *3*, 367–370.

[95]   L. K.G.D.L. F. M.R.I., "V. Contact electricity of metals", *Philosophical
        Magazine* **1898**, *46*, 82–120.

[96]   T. Glatzel, M. Lux-Steiner, E Strassburg, A Boag, Y Rosenwaks,
        "Principles of Kelvin Probe Force Microscopy" in *Scanning Probe Mi-
        croscopy: Electrical and Electromechanical Phenomena at the Nanoscale*,
        (Eds.: S. Kalinin, A. Gruverman), Springer New York, New York, NY,
        2007, pp. 113–131.

[97]   J. J. Kopanski, "Scanning Capacitance Microscopy for Electrical
        Characterization of Semiconductors and Dielectrics" in *Scanning
        Probe Microscopy: Electrical and Electromechanical Phenomena at the
        Nanoscale*, (Eds.: S. Kalinin, A. Gruverman), Springer New York,
        New York, NY, **2007**, pp. 88–112.

[98]   A Gil, J Colchero, J Gómez-Herrero, A. M. Baró, "Electrostatic force
        gradient signal: resolution enhancement in electrostatic force mi-
        croscopy and improved Kelvin probe microscopy", *Nanotechnology*
        2003, *14*, 332.

[99]   I. Horcas, R. Fernández, J. M. Gómez-Rodríguez, et al., "WSXM: A
        software for scanning probe microscopy and a tool for nanotechnol-
        ogy", *Review of Scientific Instruments* **2007**, *78*, 013705.

[100]   A. Perez-Rodriguez, E. Barrena, A. Fernández, E. Gnecco, C. Ocal,
        "A molecular–scale portrait of domain imaging in organic surfaces",
        Nanoscale **2017**, *9*, 5589–5596.

[101]   M. Paradinas, A. Pérez-Rodríguez, E. Barrena, C. Ocal, "Real Space
        Demonstration of Induced Crystalline 3D Nanostructuration of Or-
        ganic Layers", *The Journal of Physical Chemistry B* **2017**, *0*, PMID:
        28719211, null.

[102]   A. O. F. Jones, B. Chattopadhyay, Y. H. Geerts, R. Resel, "Substrate-
        induced and thin-film phases: Polymorphism of organic materials
        on surfaces", *Advanced Functional Materials* **2016**, *26*, 2233–2255.

[103]   F. Liscio, S. Milita, C. Albonetti, et al., "Structure and morphology
        of PDI8-CN2 for n-type thin-film transistors", *Advanced Functional
        Materials* **2012**, *22*, 943–953.

[104] X. Yang, J. Loos, "Toward high-performance polymer solar cells: The importance of morphology control", *Macromolecules* **2007**, *40*, 1353–1362.

[105] H. Klauk, "Organic thin-film transistors", *Chemical Society reviews* **2010**, *39*, 2643–66.

[106] Y. Don Park, J. A. Lim, H. S. Lee, K. Cho, "Interface engineering in organic transistors", *Materials Today* **2007**, *10*, 46–54.

[107] H. Sirringhaus, T. Sakanoue, J. F. Chang, "Charge-transport physics of high-mobility molecular semiconductors", *Physica Status Solidi (B) Basic Research* **2012**, *249*, 1655–1676.

[108] F. Dinelli, M. Murgia, P. Levy, et al., "Spatially Correlated Charge Transport in Organic Thin Film Transistors", *Physical Review Letters* **2004**, *92*, 116802.

[109] M. Tello, M. Chiesa, C. M. Duffy, H. Sirringhaus, "Charge Trapping in Intergrain Regions of Pentacene Thin Film Transistors", *Advanced Functional Materials* **2008**, *18*, 3907–3913.

[110] M. Aghamohammadi, A. Fernández, M. Schmidt, et al., "Influence of the relative molecular orientation on interfacial charge-transfer Excitons at donor/acceptor Nanoscale heterojunctions", *Journal of Physical Chemistry C* **2014**, *118*, 14833–14839.

[111] Y. Hu, N. Berdunov, C.-a. Di, et al., "Effect of Molecular Asymmetry on the Charge Transport Physics of High Mobility n-Type Molecular Semiconductors Investigated by Scanning Kelvin Probe Microscopy", *ACS Nano* **2014**, *8*, 6778–6787.

[112] Y. Yamagishi, K. Noda, K. Kobayashi, H. Yamada, "Interlayer Resistance and Edge-Specific Charging in Layered Molecular Crystals Revealed by Kelvin-Probe Force Microscopy", *The Journal of Physical Chemistry C* **2015**, *119*, 3006–3011.

[113] J. Rivnay, L. H. Jimison, J. E. Northrup, et al., "Large modulation of carrier transport by grain-boundary molecular packing and microstructure in organic thin films", *Nature Materials* **2009**, *8*, 952–958.

[114] M. Gsänger, J. H. Oh, M. Könemann, et al., "A crystal-engineered hydrogen-bonded octachloroperylene diimide with a twisted core: An n-channel organic semiconductor", *Angewandte Chemie - International Edition* **2010**, *49*, 740–743.

[115] N. A. Minder, S. Lu, S. Fratini, et al., "Tailoring the molecular structure to suppress extrinsic disorder in organic transistors", *Advanced Materials* **2014**, *26*, 1254–1260.

[116] R. Schmidt, J. H. Oh, Y.-s. Sun, et al., "High-Performance Air-Stable n-Channel Organic Thin Film Transistors Based on Halogenated Perylene Bisimide Semiconductors High-Performance Air-Stable n-Channel Organic Thin Film Transistors Based on Halogenated Perylene", *Journal of the American Chemical Society* **2009**, *131*, 6215–6228.

[117] C. W. Struijk, A. B. Sieval, J. E. J. Dakhorst, et al., "Liquid Crystalline Perylene Diimides : Architecture and Charge Carrier Mobilities", *Journal of the American Chemical Society* **2000**, *122*, 11057–11066.

[118] O. Shekhah, N. Roques, V. Mugnaini, et al., "Grafting of Mono-carboxylic Substituted Polychlorotriphenylmethyl Radicals onto a COOH-Functionalized Self-Assembled Monolayer through Copper (II) Metal Ions", *Langmuir* **2008**, *24*, 6640–6648.

[119] M. Aghamohammadi, A. Fernández, M. Schmidt, et al., "Influence of the Relative Molecular Orientation on Interfacial Charge-Transfer Excitons at Donor/Acceptor Nanoscale Heterojunctions", *The Journal of Physical Chemistry C* **2014**, *118*, 14833–14839.

[120] T. N. Krauss, E. Barrena, X. N. Zhang, et al., "Three-dimensional molecular packing of thin organic films of PTCDI-C8 determined by surface X-ray diffraction.", *Langmuir : the ACS journal of surfaces and colloids* **2008**, *24*, 12742–12744.

[121] T. N. Krauss, E. Barrena, G. De OteyzaDimas, et al., "X-ray / Atomic Force Microscopy Study of the Temperature-Dependent Multilayer Structure of PTCDI-C 8 Films on SiO 2", *Journal of Physical Chemistry C* **2009**, *113*, 4502–4506.

[122] V. Kalihari, "Transverse Shear Microscopy: A Novel Microstructural Probe for Organic Semiconductor Thin Films", **2010**.

[123] M. Campione, S. Trabattoni, M. Moret, "Nanoscale mapping of frictional anisotropy", *Tribology Letters* **2012**, *45*, 219–224.

[124] M. Campione, E. Fumagalli, "Friction Anisotropy of the Surface of Organic Crystals and Its Impact on Scanning Force Microscopy", *Phys. Rev. Lett.* **2010**, *105*, 166103.

[125] V. Kalihari, E. B. Tadmor, G. Haugstad, C. D. Frisbie, "Grain orientation mapping of polycrystalline organic semiconductor films by transverse shear microscopy", *Advanced Materials* **2008**, *20*, 4033–4039.

[126] V. Kalihari, D. J. Ellison, G. Haugstad, C. D. Frisbie, "Observation of Unusual Homoepitaxy in Ultrathin Pentacene Films and Correlation with Surface Electrostatic Potential", *Advanced Materials* **2009**, *21*, 3092–3098.

[127] P. Langevin, "Sur la théorie du mouvement brownien", *Comptes Rendus de l'Académie des Sciences* **1908**, *146*, 530–533.

[128] P. Steiner, R. Roth, E. Gnecco, A. Baratoff, E. Meyer, "Angular dependence of static and kinetic friction on alkali halide surfaces", *Physical Review B* **2010**, *82*, 205417.

[129] A. Schirmeisen, L. Jansen, H. Hölscher, H. Fuchs, "Temperature dependence of point contact friction on silicon", *Applied Physics Letters* **2006**, *88*, 123108.

[130] A. Socoliuc, R. Bennewitz, E. Gnecco, E. Meyer, "Transition from stick-slip to continuous sliding in atomic friction: Entering a new regime of ultralow friction", *Physical Review Letters* **2004**, *92*, 134301.

[131] B. F. J. Rubio-sierra, W. M. Heckl, R. W. Stark, "Nanomanipulation by Atomic Force Microscopy", *Advanced Engineering Materials* **2005**, *7*, 193–196.

[132] R. D. Piner, J. Zhu, F. Xu, S. Hong, C. A. Mirkin, ""Dip-Pen" Nanolithography", *Science* **1999**, *283*, 661–663.

[133] O. Shekhah, H. Wang, M. Paradinas, et al., "Controlling interpenetration in metal-organic frameworks by liquid-phase epitaxy", *Nat Mater* **2009**, *8*, PMID: 18522443, 481–484.

[134] S. Xu, G. yu Liu, "Nanometer-Scale Fabrication by Simultaneous Nanoshaving and Molecular Self-Assembly", *Langmuir* **1997**, *13*, 127–129.

[135] E Barrena, C Ocal, M. Salmeron, "Structure and stability of tilted-chain phases of alkanethiols on Au(111)", *Journal of Chemical Physics* **2001**, *114*, 4210–4214.

[136] E. Barrena, E. Palacios-Lidón, C. Munuera, et al., "The Role of Intermolecular and Molecule-Substrate Interactions in the Stability of Alkanethiol Nonsaturated Phases on Au(111)", *Journal of the American Chemical Society* **2004**, *126*, 385–395.

[137]　C. Munuera, J. Puigmartí-Luis, M. Paradinas, et al., "Layer-By-Layer Electropeeling of Organic Conducting Material Imaged In Real Time", *Small* **2008**, *5*, 214–220.

[138]　S. F. Lyuksyutov, R. A. Vaia, P. B. Paramonov, et al., "Electrostatic nanolithography in polymers using atomic force microscopy", *Nature Materials* **2003**, *2*, 468–472.

[139]　H. C. Day, D. R. Allee, "Selective area oxidation of silicon with a scanning force microscope", *Applied Physics Letters* **1993**, *62*, 2691–2693.

[140]　C. Moreno, C. Munuera, S. Valencia, et al., "Reversible Resistive Switching and Multilevel Recording in La0.7Sr0.3MnO3Thin Films for Low Cost Nonvolatile Memories", *Nano Letters* **2010**, *10*, 3828–3835.

[141]　G. Gbabode, M. Dohr, C. Niebel, et al., "X-ray Structural Investigation of Nonsymmetrically and Symmetrically Alkylated [1] Benzothieno [3,2-b] benzothiophene Derivatives in Bulk and Thin Films", *ACS applied materials & interfaces* **2014**, *6*, 13413–13421.

[142]　A. O. F. Jones, Y. H. Geerts, J. Karpinska, et al., "Substrate-Induced Phase of a [1]Benzothieno[3,2-b]benzothiophene Derivative and Phase Evolution by Aging and Solvent Vapor Annealing.", *ACS applied materials & interfaces* **2015**, *7*, 1868–1873.

[143]　M. Saliba, T. Matsui, J.-Y. Seo, et al., "Cesium-containing triple cation perovskite solar cells: improved stability, reproducibility and high efficiency", *Energy Environ. Sci.* **2016**, *9*, 1989–1997.

[144]　H. Wang, E. D. Gomez, Z. Guan, et al., "Tuning Contact Recombination and Open-Circuit Voltage in Polymer Solar Cells via Self-Assembled Monolayer Adsorption at the Organic–Metal Oxide Interface", *The Journal of Physical Chemistry C* **2013**, *117*, 20474–20484.

[145]　T. Stubhan, M. Salinas, A. Ebel, et al., "Increasing the Fill Factor of Inverted P3HT:PCBM Solar Cells Through Surface Modification of Al-Doped ZnO via Phosphonic Acid-Anchored C60 SAMs", *Advanced Energy Materials* **2012**, *2*, 532–535.

[146]　A. Wagenpfahl, D. Rauh, M. Binder, C. Deibel, V. Dyakonov, "S-shaped current-voltage characteristics of organic solar devices", **2010**, 9.

[147] R. Saive, C. Mueller, J. Schinke, R. Lovrincic, W. Kowalsky, "Under-standing S-shaped current-voltage characteristics of organic solar cells: Direct measurement of potential distributions by scanning Kelvin probe", *Applied Physics Letters* **2013**, *103*, 243303.

[148] J. Wang, X. Ren, S. Shi, C. Leung, P. K. Chan, "Charge accumulation induced S-shape J–V curves in bilayer heterojunction organic solar cells", *Organic Electronics* **2011**, *12*, 880–885.

[149] A. Kumar, S. Sista, Y. Yang, "Dipole induced anomalous S-shape I-V curves in polymer solar cells", *Journal of Applied Physics* **2009**, *105*, 094512.

[150] B. Y. Finck, B. J. Schwartz, "Understanding the origin of the S-curve in conjugated polymer/fullerene photovoltaics from drift-diffusion simulations", *Applied Physics Letters* **2013**, *103*, 053306.

[151] W. Tress, K. Leo, M. Riede, "Influence of hole-transport layers and donor materials on open-circuit voltage and shape of I-V curves of organic solar cells", *Advanced Functional Materials* **2011**, *21*, 2140–2149.

[152] B. Zacher, N. R. Armstrong, "Modeling the effects of molecular length scale electrode heterogeneity in organic solar cells", *The Journal of Physical Chemistry C* **2011**, *115*, 25496–25507.

[153] B. Chen, X. Qiao, C. M. Liu, et al., "Effects of bulk and interfacial charge accumulation on fill factor in organic solar cells", *Applied Physics Letters* **2013**, *102*, 5–9.

[154] S. Paniagua, P. Hotchkiss, "Phosphonic Acid Modification of Indium Tin Oxide Electrodes: Combined XPS/UPS/Contact Angle Studies†", *The Journal of Physical Chemistry C* **2008**, 7809–7817.

[155] H.-Y. Chen, J. Hou, S. Zhang, et al., "Polymer solar cells with en-hanced open-circuit voltage and efficiency", *Nature Photonics* **2009**, *3*, 649–653.

[156] Y. Liang, Y. Wu, D. Feng, et al., "Development of New Semicon-ducting Polymers for High Performance Solar Cells", *Journal of the American Chemical Society* **2009**, *131*, 56–57.

[157] B. C. Thompson, J. M. J. Fréchet, "Polymer-fullerene composite solar cells", *Angewandte Chemie - International Edition* **2008**, *47*, 58–77.

[158] H. Derouiche, S. Saidi, A. B. Mohamed, "The Effect of Energy Levels of the Electron Acceptor Materials on Organic Photovoltaic Cells", *Smart Grid and Renewable Energy* **2011**, *2*, 278.

[159] M. M. Wienk, J. M. Kroon, W. J. H. Verhees, et al., "Efficient Methano[70]fullerene/MDMO-PPV Bulk Heterojunction Photovoltaic Cells", *Angewandte Chemie International Edition* **2003**, *42*, 3371–3375.

[160] R. Jin, K. Wang, "Rational Design of Diketopyrrolopyrrole-Based Small Moleculesas Donating Materials for Organic Solar Cells", *International Journal of Molecular Sciences* **2015**, *16*, 20326–20343.

[161] K. M. Knesting, P. J. Hotchkiss, B. a. Macleod, S. R. Marder, D. S. Ginger, "Spatially modulating interfacial properties of transparent conductive oxides: patterning work function with phosphonic Acid self-assembled monolayers.", *Advanced materials (Deerfield Beach Fla.)* **2012**, *24*, 642–6.

[162] R Schlaf, H Murata, Z. Kafafi, "Work function measurements on indium tin oxide films", *Journal of Electron Spectroscopy and Related Phenomena* **2001**, *120*, 149–154.

[163] U. Koldemir, J. L. Braid, A. Morgenstern, et al., "Molecular Design for Tuning Work Functions of Transparent Conducting Electrodes", *The Journal of Physical Chemistry Letters* **2015**, 1948–7185.

[164] I. D. Baikie, A. Grain, J. Sutherland, J. Law, "Near ambient pressure photoemission spectroscopy of metal and semiconductor surfaces", *physica status solidi (c)* **2015**, *12*, 259–262.

[165] L. J. A. Koster, V. D. Mihailetchi, H. Xie, P. W. M. Blom, "Origin of the light intensity dependence of the short-circuit current of polymer/fullerene solar cells", *Applied Physics Letters* **2005**, *87*, 1–3.

[166] H.-N. Lin, S.-H. Chen, G.-Y. Perng, S.-A. Chen, "Nanoscale surface electrical properties of indium–tin–oxide films for organic light emitting diodes investigated by conducting atomic force microscopy", *Journal of Applied Physics* **2001**, *89*, 3976.

[167] S. A. Rutledge, A. S. Helmy, "Carrier mobility enhancement in poly(3,4-ethylenedioxythiophene)-poly(styrenesulfonate) having undergone rapid thermal annealing", *Journal of Applied Physics* **2013**, *114*, 133708.

[168] B. Mazhari, "An improved solar cell circuit model for organic solar cells", *Solar Energy Materials and Solar Cells* **2006**, *90*, 1021–1033.

[169] B. Romero, G. del Pozo, B. Arredondo, et al., "S-Shaped I – V Characteristics of Organic Solar Cells: Solving Mazhari's Lumped-Parameter Equivalent Circuit Model", *IEEE Transactions on Electron Devices* **2017**, *64*, 4622–4627.

[170]   M. Brumbach, P. A. Veneman, F. S. Marrikar, et al., "Surface composition and electrical and electrochemical properties of freshly deposited and acid-etched indium tin oxide electrodes.", *Langmuir : the ACS journal of surfaces and colloids* **2007**, *23*, 11089–99.

[171]   M. Brumbach, P. A. Veneman, F. S. Matrikar, et al., "Surface composition and electrical and electrochemical properties of freshly deposited and acid-etched indium tin oxide electrodes", *Langmuir* **2007**, *23*, 11089–11099.

[172]   G. A. MacDonald, P. A. Veneman, D. Placencia, N. R. Armstrong, "Electrical Property Heterogeneity at Transparent Conductive Oxide/Organic Semiconductor Interfaces: Mapping Contact Ohmicity Using Conducting-Tip Atomic Force Microscopy", *ACS Nano* **2012**, *6*, 9623–9636.

[173]   C. Ionescu-Zanetti, a. Mechler, S. Carter, R. Lal, "Semiconductive Polymer Blends: Correlating Structure with Transport Properties at the Nanoscale", *Advanced Materials* **2004**, *16*, 385–389.

[174]   D. Bi, W. Tress, M. I. Dar, et al., "Efficient luminescent solar cells based on tailored mixed-cation perovskites", *Science advances* **2016**, *2*, e1501170.

[175]   J. Shi, X. Xu, D. Li, Q. Meng, "Interfaces in perovskite solar cells", *Small* **2015**, *11*, 2472–2486.

[176]   M. A. Green, A. Ho-Baillie, H. J. Snaith, "The emergence of perovskite solar cells", *Nature Photonics* **2014**, *8*.

[177]   J. Jiménez-López, W. Cambarau, L. Cabau, E. Palomares, "Charge Injection, Carriers Recombination and HOMO Energy Level Relationship in Perovskite Solar Cells", *Scientific reports* **2017**, *7*, 6101.

[178]   A. Abate, M. Planells, D. J. Hollman, et al., "Hole-transport materials with greatly-differing redox potentials give efficient TiO 2–[CH 3 NH 3][PbX 3] perovskite solar cells", *Physical Chemistry Chemical Physics* **2015**, *17*, 2335–2338.

[179]   L. E. Polander, P. Pahner, M. Schwarze, et al., "Hole-transport material variation in fully vacuum deposited perovskite solar cells", *APL Materials* **2014**, *2*, 081503.

[180]   Y. Chen, T. Chen, L. Dai, "Layer-by-Layer Growth of CH3NH3PbI3-xClx for Highly Efficient Planar Heterojunction Perovskite Solar Cells", *Advanced Materials* **2015**, *27*, 1053–1059.

[181] L. Cabau, I. Garcia-Benito, A. Molina-Ontoria, et al., "Diarylamino-substituted tetraarylethene (TAE) as an efficient and robust hole transport material for 11% methyl ammonium lead iodide perovskite solar cells", *Chemical Communications* **2015**, *51*, 13980–13982.

[182] I. D. Baikie, A. C. Grain, J. Sutherland, J. Law, "Ambient pressure photoemission spectroscopy of metal surfaces", *Applied Surface Science* **2014**, *323*, 45–53.

[183] Y. Huang, E. J. Kramer, A. J. Heeger, G. C. Bazan, "Bulk Heterojunction Solar Cells: Morphology and Performance Relationships", *Chemical Reviews* **2014**, *114*, PMID: 24869423, 7006–7043.

[184] H. Hoppe, N. S. Sariciftci, "Morphology of polymer/fullerene bulk heterojunction solar cells", *Journal of Materials Chemistry* **2006**, *16*, 45.

[185] J Peet, J. Y. Kim, N. E. Coates, et al., "Efficiency enhancement in low-bandgap polymer solar cells by processing with alkane dithiols", *Nature Materials* **2007**, *6*, 497.

[186] K. R. Graham, P. M. Wieruszewski, R. Stalder, et al., "Improved Performance of Molecular Bulk-Heterojunction Photovoltaic Cells through Predictable Selection of Solvent Additives", *Advanced Functional Materials* **2012**, *22*, 4801–4813.

[187] E. Verploegen, R. Mondal, C. J. Bettinger, et al., "Effects of Thermal Annealing Upon the Morphology of Polymer–Fullerene Blends", *Advanced Functional Materials* **2010**, *20*, 3519–3529.

[188] B. Kan, M. Li, Q. Zhang, et al., "A Series of Simple Oligomer-like Small Molecules Based on Oligothiophenes for Solution-Processed Solar Cells with High Efficiency", *Journal of the American Chemical Society* **2015**, *137*, PMID: 25736989, 3886–3893.

[189] B. Gholamkhass, P. Servati, "Solvent–vapor induced morphology reconstruction for efficient PCDTBT based polymer solar cells", *Organic Electronics* **2013**, *14*, 2278–2283.

[190] H. Tang, G. Lu, L. Li, et al., "Precise construction of PCBM aggregates for polymer solar cells via multi-step controlled solvent vapor annealing", *Journal of Materials Chemistry* **2010**, *20*, 683–688.

[191] C. D. Wessendorf, G. L. Schulz, A. Mishra, et al., "Efficiency Improvement of Solution-Processed Dithienopyrrole-Based A-D-A Oligothiophene Bulk-Heterojunction Solar Cells by Solvent Vapor Annealing", *Advanced Energy Materials* **2014**, *4*.

[192]   C. D. Wessendorf, A. Perez-Rodriguez, J. Hanisch, et al., "Understanding the effect of solvent vapor annealing on solution-processed A–D–A oligothiophene bulk-heterojunction solar cells: the role of alkyl side chains", *J. Mater. Chem. A* **2016**, *4*, 2571–2580.

[193]   S.-H. Liao, H.-J. Jhuo, P.-N. Yeh, et al., "Single junction inverted polymer solar cell reaching power conversion efficiency 10.31% by employing dual-doped zinc oxide nano-film as cathode interlayer", *Scientific reports* **2014**, *4*, 6813.

[194]   X. Xiao, G. Wei, S. Wang, et al., "Small-Molecule Photovoltaics Based on Functionalized Squaraine Donor Blends", *Advanced Materials* **2012**, *24*, 1956–1960.

[195]   H. Bürckstümmer, E. V. Tulyakova, M. Deppisch, et al., "Efficient Solution-Processed Bulk Heterojunction Solar Cells by Antiparallel Supramolecular Arrangement of Dipolar Donor–Acceptor Dyes", *Angewandte Chemie* **2011**, *123*, 11832–11836.

[196]   B. Yin, L. Yang, Y. Liu, et al., "Solution-processed bulk heterojunction organic solar cells based on an oligothiophene derivative", *Applied Physics Letters* **2010**, *97*, 139.

[197]   G. Long, X. Wan, B. Kan, et al., "Investigation of quinquethiophene derivatives with different end groups for high open circuit voltage solar cells", *Advanced Energy Materials* **2013**, *3*, 639–646.

[198]   Y. Liu, X. Wan, F. Wang, et al., "High-Performance Solar Cells using a Solution-Processed Small Molecule Containing Benzodithiophene Unit", *Advanced Materials* **2011**, *23*, 5387–5391.

[199]   Y. Liu, Y. M. Yang, C.-C. Chen, et al., "Solution-Processed Small Molecules Using Different Electron Linkers for High-Performance Solar Cells", *Advanced Materials* **2013**, *25*, 4657–4662.

[200]   B. Walker, C. Kim, T.-Q. Nguyen, "Small molecule solution-processed bulk heterojunction solar cells", *Chemistry of Materials* **2010**, *23*, 470–482.

[201]   T. S. Van Der Poll, J. A. Love, T.-Q. Nguyen, G. C. Bazan, "Non-Basic High-Performance Molecules for Solution-Processed Organic Solar Cells", *Advanced Materials* **2012**, *24*, 3646–3649.

[202]   M. Weidelener, C. D. Wessendorf, J. Hanisch, et al., "Dithienopyrrole-based oligothiophenes for solution-processed organic solar cells", *Chemical Communications* **2013**, *49*, 10865–10867.

[203]   G. Wei, S. Wang, K. Sun, M. E. Thompson, S. R. Forrest, "Solvent-Annealed crystalline squaraine: PC70BM (1: 6) solar Cells", *Advanced Energy Materials* **2011**, *1*, 184–187.

[204]   M. R. Hammond, R. J. Kline, A. A. Herzing, et al., "Molecular order in high-efficiency polymer/fullerene bulk heterojunction solar cells", *Acs Nano* **2011**, *5*, 8248–8257.

[205]   X. Yang, J. K. van Duren, M. T. Rispens, et al., "Crystalline Organization of a Methanofullerene as Used for Plastic Solar-Cell Applications", *Advanced Materials* **2004**, *16*, 802–806.

[206]   M. He, M. Wang, C. Lin, Z. Lin, "Optimization of molecular organization and nanoscale morphology for high performance low bandgap polymer solar cells", *Nanoscale* **2014**, *6*, 3984–3994.

[207]   N. D. Treat, M. L. Chabinyc, "Phase separation in bulk heterojunctions of semiconducting polymers and fullerenes for photovoltaics", *Annual review of physical chemistry* **2014**, *65*, 59–81.

[208]   A. J. Heeger, "25th anniversary article: bulk heterojunction solar cells: understanding the mechanism of operation", *Advanced Materials* **2014**, *26*, 10–28.

[209]   S Sadewasser, T. Glatzel, M Rusu, A Jäger-Waldau, M. C. Lux-Steiner, "High-resolution work function imaging of single grains of semiconductor surfaces", *Applied Physics Letters* **2002**, *80*, 2979–2981.

[210]   C.-S. Jiang, H. Moutinho, D. Friedman, J. Geisz, M. Al-Jassim, "Measurement of built-in electrical potential in III–V solar cells by scanning Kelvin probe microscopy", *Journal of applied physics* **2003**, *93*, 10035–10040.

[211]   V. Palermo, G. Ridolfi, A. M. Talarico, et al., "A Kelvin Probe Force Microscopy Study of the Photogeneration of Surface Charges in All-Thiophene Photovoltaic Blends", *Advanced Functional Materials* **2007**, *17*, 472–478.

[212]   M. Chiesa, L. Bürgi, J.-S. Kim, et al., "Correlation between surface photovoltage and blend morphology in polyfluorene-based photodiodes", *Nano letters* **2005**, *5*, 559–563.

[213]   H. Hoppe, T. Glatzel, M. Niggemann, et al., "Kelvin probe force microscopy study on conjugated polymer/fullerene bulk heterojunction organic solar cells", *Nano Letters* **2005**, *5*, 269–274.

[214] K. Maturová, M. Kemerink, M. M. Wienk, D. S. Charrier, R. A. Janssen, "Scanning kelvin probe microscopy on bulk heterojunction polymer blends", *Advanced Functional Materials* **2009**, *19*, 1379–1386.

[215] M Campoy-Quiles, T Ferenczi, T Agostinelli, et al., "Morphology evolution via self-organization and lateral and vertical diffusion in polymer: fullerene solar cell blends", *Nature Materials* **2008**, *7*, 158–164.

[216] Z. Xu, L.-M. Chen, G. Yang, et al., "Vertical phase separation in Poly (3-hexylthiophene): fullerene derivative blends and its advantage for inverted structure solar cells", *Advanced Functional Materials* **2009**, *19*, 1227–1234.

[217] A. Pérez-Rodríguez, I. Temiño, C. Ocal, M. Mas-Torrent, E. Barrena, "Decoding the vertical phase separation and its impact on C8-BTBT/PS Transistors properties", *ACS Appl. Mater. Interfaces* **2018**, *10*, 7296–7303.

[218] I. Temiño, F. G. Del Pozo, M. Ajayakumar, et al., "A Rapid, Low-Cost, and Scalable Technique for Printing State-of-the-Art Organic Field-Effect Transistors", *Advanced Materials Technologies* **2016**, *1*.

[219] G. Horowitz et al., "Organic field-effect transistors", *Advanced materials* **1998**, *10*, 365–377.

[220] Y. Diao, L. Shaw, Z. Bao, S. C. B. Mannsfeld, "Morphology control strategies for solution-processed organic semiconductor thin films", *Energy Environ. Sci.* **2014**, *7*, 2145–2159.

[221] A. A. Virkar, S. Mannsfeld, Z. Bao, N. Stingelin, "Organic semiconductor growth and morphology considerations for organic thin-film transistors.", *Advanced materials (Deerfield Beach Fla.)* **2010**, *22*, 3857–75.

[222] W. H. Lee, J. A. Lim, D. Kwak, et al., "Semiconductor-dielectric blends: A facile all solution route to flexible all-organic transistors", *Advanced Materials* **2009**, *21*, 4243–4248.

[223] A. F. Paterson, N. D. Treat, W. Zhang, et al., "Small Molecule/Polymer Blend Organic Transistors with Hole Mobility Exceeding 13 cm V[1] s [1]", *Advanced Materials* **2016**, 1–8.

[224] M. J. Ford, M. Wang, S. N. Patel, et al., "High Mobility Organic Field-Effect Transistors from Majority Insulator Blends", *Chemistry of Materials* **2016**, *28*, 1256–1260.

[225] D. He, Y. Zhang, Q. Wu, et al., "Two-dimensional quasi-freestanding molecular crystals for high-performance organic field-effect transistors", *Nature Communications* **2014**, *5*, 5162.

[226] M. R. Niazi, R. Li, E. Q. Li, et al., "Solution-printed organic semiconductor blends exhibiting transport properties on par with single crystals", *Nature Communications* **2015**, *6*, 8598.

[227] Y. Yuan, G. Giri, A. L. Ayzner, et al., "Ultra-high mobility transparent organic thin film transistors grown by an off-centre spin-coating method.", *Nature communications* **2014**, *5*, 3005.

[228] P. Bobbert, A. Sharma, S. Mathijssen, M. Kemerink, D. De Leeuw, "Operational stability of organic field-effect transistors", *Advanced Materials* **2012**, *24*, 1146–1158.

[229] T. Ohe, M. Kuribayashi, R. Yasuda, et al., "Solution-processed organic thin-film transistors with vertical nanophase separation", *Applied Physics Letters* **2008**, *93*, 1–4.

[230] N. Shin, J. Kang, L. J. Richter, et al., "Vertically segregated structure and properties of small molecule-polymer blend semiconductors for organic thin-film transistors", *Advanced Functional Materials* **2013**, *23*, 366–376.

[231] G. Schweicher, V. Lemaur, C. Niebel, et al., "Bulky End-Capped [1] Benzothieno [3, 2-b] benzothiophenes: Reaching High-Mobility Organic Semiconductors by Fine Tuning of the Crystalline Solid-State Order", *Advanced Materials* **2015**, *27*, 3066–3072.

[232] H. Ebata, T. Izawa, E. Miyazaki, et al., "Highly Soluble [1] Benzothieno [3,2- b] benzothiophene (BTBT) Derivatives for High-Performance, Solution-Processed Organic Field-Effect Transistors", *Journal of the American Chemical Society* **2007**, *129*, 15732–15733.

[233] A. Y. Amin, A. Khassanov, K. Reuter, T. Meyer-Friedrichsen, M. Halik, "Low-Voltage Organic Field Effect Transistors with a 2-Tridecyl [1] benzothieno [3,2-b] [1] benzothiophene Semiconductor Layer", *Journal of the American Chemical Society* **2012**, *134*, 16548–16550.

[234] J. Tsutsumi, S. Matsuoka, S. Inoue, et al., "N-type field-effect transistors based on layered crystalline donor–acceptor semiconductors with dialkylated benzothienobenzothiophenes as electron donors", *J. Mater. Chem. C* **2015**, *3*, 1976–1981.

[235] R. W. Carpick, D. Y. Sasaki, A. R. Burns, "Large friction anisotropy of a polydiacetylene monolayer", *Tribology Letters* **1999**, *7*, 79–85.

[236] K. Hisada, C. M. Knobler, "Friction anisotropy and asymmetry related to the molecular tilt azimuth in a monolayer of glycerol ester", *Langmuir* **2000**, *16*, 9390–9395.

[237] M. Paradinas, C. Munuera, C. Silien, M. Buck, C. Ocal, "Heterogeneous nanotribological response of polymorphic self-assembled monolayers arising from domain and phase dependent friction.", *Physical chemistry chemical physics* **2013**, *15*, 1302–1309.

[238] J. S. Choi, J.-s. Kim, I.-S. Byun, et al., "Friction anisotropy driven domain imaging on exfoliated monolayer Graphene", *Science* **2011**, *333*, 607–10.

[239] P. Miranzo, L. López-Mir, B. Román-Manso, et al., "Prominent local transport in silicon carbide composites containing in-situ synthesized three-dimensional graphene networks", *Journal of the European Ceramic Society* **2016**, *36*, 3073–3081.

[240] M. Aghamohammadi, R. R??del, U. Zschieschang, et al., "Threshold-Voltage Shifts in Organic Transistors Due to Self-Assembled Monolayers at the Dielectric: Evidence for Electronic Coupling and Dipolar Effects", *ACS Applied Materials and Interfaces* **2015**, *7*, 22775–22785.

[241] C Munuera, E Barrena, C Ocal, "Scanning force microscopy three-dimensional modes applied to conductivity measurements through linear-chain organic SAMs", *Nanotechnology* **2007**, *18*, 125505.

[242] G. J. Leggett, N. J. Brewer, K. S. L. Chong, "Friction force microscopy: towards quantitative analysis of molecular organisation with nanometre spatial resolution", *Physical Chemistry Chemical Physics* **2005**, *7*, 1107–1120.

[243] S. Georgakopoulos, F. G. del Pozo, M. Mas-Torrent, "Flexible organic transistors based on a solution-sheared PVDF insulator", *J. Mater. Chem. C* **2015**, *3*, 12199–12202.

[244] Y. Mei, D. Fogel, J. Chen, et al., "Interface engineering to enhance charge injection and transport in solution-deposited organic transistors", *Organic Electronics* **2017**, *50*, 100–105.

[245] M. Kano, T. Minari, K. Tsukagoshi, "Improvement of subthreshold current transport by contact interface modification in p -type organic field-effect transistors", *Applied Physics Letters* **2009**, *94*, DOI 10 . 1063/1.3115826.

[246] T. Minari, P. Darmawan, C. Liu, et al., "Highly enhanced charge injection in thienoacene-based organic field-effect transistors with chemically doped contact", *Applied Physics Letters* **2012**, *100*, 59.

[247] M. L. Tietze, L. Burtone, M. Riede, B. Lüssem, K. Leo, "Fermi level shift and doping efficiency in p-doped small molecule organic semiconductors: a photoelectron spectroscopy and theoretical study", *Physical Review B* **2012**, *86*, 035320.

[248] S Georgakopoulos, A Pérez-Rodríguez, A Campos, et al., "Spray-coated contacts from an organic charge transfer complex solution for organic field-effect transistors", *Organic Electronics* **2017**, *48*, 365–370.

[249] M. L. Tietze, L. Burtone, M. Riede, B. Lüssem, K. Leo, "Fermi level shift and doping efficiency in p-doped small molecule organic semiconductors: A photoelectron spectroscopy and theoretical study", *Physical Review B - Condensed Matter and Materials Physics* **2012**, *86*, 1–12.

[250] J.-L. Hou, D. Kasemann, J. Widmer, et al., "Reduced contact resistance in top-contact organic field-effect transistors by interface contact doping", *Applied Physics Letters* **2016**, *108*, 103303.

[251] D. Natali, L. Fumagalli, M. Sampietro, "Modeling of organic thin film transistors: Effect of contact resistances", *Journal of applied physics* **2007**, *101*, 014501.

[252] E. G. Bittle, J. I. Basham, T. N. Jackson, O. D. Jurchescu, D. J. Gundlach, "Mobility overestimation due to gated contacts in organic field-effect transistors", *Nature communications* **2016**, *7*, 10908.

[253] H. Minemawari, T. Yamada, H. Matsui, et al., "Inkjet printing of single-crystal films", *Nature* **2011**, *475*, 364–367.

[254] Y. Hu, N. Berdunov, C.-a. Di, et al., "Effect of molecular asymmetry on the charge transport physics of high mobility n-type molecular semiconductors investigated by scanning Kelvin probe microscopy", *ACS nano* **2014**, *8*, 6778–6787.

[255] L. C. Teague, O. D. Jurchescu, C. A. Richter, et al., "Probing stress effects in single crystal organic transistors by scanning Kelvin probe microscopy", *Applied Physics Letters* **2010**, *96*, 100.

[256] T Hallam, C. Duffy, T Minakata, M Ando, H Sirringhaus, "A scanning Kelvin probe study of charge trapping in zone-cast pentacene thin film transistors", *Nanotechnology* **2008**, *20*, 025203.

[257] E. M. Muller, J. A. Marohn, "Microscopic evidence for spatially inhomogeneous charge trapping in pentacene", *Advanced Materials* **2005**, *17*, 1410–1414.

[258] M. Egginger, S. Bauer, R. Schwödiauer, H. Neugebauer, N. S. Sariciftci, "Current versus gate voltage hysteresis in organic field effect transistors", *Monatshefte für Chemie-Chemical Monthly* **2009**, *140*, 735–750.

[259] S. K. Possanner, K. Zojer, P. Pacher, E. Zojer, F. Schürrer, "Threshold Voltage Shifts in Organic Thin-Film Transistors Due to Self-Assembled Monolayers at the Dielectric Surface", *Advanced Functional Materials* **2009**, *19*, 958–967.

[260] N. Koch, S. Duhm, J. P. Rabe, A. Vollmer, R. L. Johnson, "Optimized hole injection with strong electron acceptors at organic-metal interfaces", *Physical review letters* **2005**, *95*, 237601.

[261] W. Gao, A. Kahn, "Controlled p doping of the hole-transport molecular material N, N-diphenyl-N, N-bis (1-naphthyl)-1, 1-biphenyl-4, 4-diamine with tetrafluorotetracyanoquinodimethane", *Journal of Applied Physics* **2003**, *94*, 359–366.

[262] T. Hallam, M. Lee, N. Zhao, et al., "Local Charge Trapping in Conjugated Polymers Resolved by Scanning Kelvin Probe Microscopy", *Phys. Rev. Lett.* **2009**, *103*, 1–4.

[263] T. W. Kelley, C. D. Frisbie, "Gate voltage dependent resistance of a single organic semiconductor grain boundary", *The Journal of Physical Chemistry B* **2001**, *105*, 4538–4540.

[264] A. B. Chwang, C. D. Frisbie, "Field effect transport measurements on single grains of sexithiophene: role of the contacts", *The Journal of Physical Chemistry B* **2000**, *104*, 12202–12209.

[265] R Scholz, A.-D. Müller, F Müller, et al. in Organic Field-Effect Transistors IV, *Vol. 5940*, International Society for Optics and Photonics, **2005**, p. 59400I.

[266] R. T. Weitz, K. Amsharov, U. Zschieschang, et al., "Organic n-channel transistors based on core-cyanated perylene carboxylic diimide derivatives", *Journal of the American Chemical Society* **2008**, *130*, 4637–4645.

[267] R. Schmidt, J. H. Oh, Y.-s. Sun, et al., "High-Performance Air-Stable n-Channel Organic Thin Film Transistors Based on Halogenated Perylene Bisimide Semiconductors High-Performance Air-Stable n-Channel Organic Thin Film Transistors Based on Halogenated Perylene", *Society* **2009**, 1–17.

[268] C. Siol, C. Melzer, H. von Seggern, "Electron trapping in pentacene based p-and n-type organic field-effect transistors", *Applied Physics Letters* **2008**, *93*, 357.

[269] Y. Hu, V. Pecunia, L. Jiang, et al., "Scanning Kelvin Probe Microscopy Investigation of the Role of Minority Carriers on the Switching Characteristics of Organic Field-Effect Transistors", *Advanced Materials* **2016**, *28*, 4713–4719.

List of Figures

List of Tables

List of Abbreviations

AFM atomic force microscopy

BAMs bar-assisted meniscus

BHJ bulk hetero junction

C-AFM conductive atomic force microscopy

CPD contact potential difference

FF friction force

FFM friction force microscopy

GIWAXs grazing-incidence wide-angle x-ray scattering

HOMO highest occupied molecular orbital

HTL hole transport layer

HTM hole transport material

ICT Integer Charge Transfer Model

KPFM kelvin probe force microscopy

LUMO lowest unoccupied molecular orbital

μCP micro contact printing

OFET organic field-effect transistor

OMBD organic molecular beam deposition

OLED organic light-emitting diode

OPV organic photovoltaic

OSC organic solar cell

PL photoluminiscence

PLL phase-locked loop

SAM self-assembled monolayer

SPM scanning probe microscopy

SVA solvent vapour annealing

TSM transverse shear microscopy

Publications

- **Decoding the Vertical Phase Separation and Its Impact on C8-BTBT/PS Transistor Properties.**
  Pérez-Rodríguez, Ana; Temiño, Inés; Ocal, Carmen; Mas-Torrent, Marta and Barrena, Esther
  ACS Appl. Mater. Interfaces **2018**, *8*, 7296–7303

- **Real Space Demonstration of Induced Crystalline 3D Nanostructuration of Organic Layers.**
  Paradinas, Markos; **Pérez-Rodríguez, Ana**; Barrena, Esther and Ocal, Carmen
  The Journal of Physical Chemistry B **2017**, *122*, 633-639.

- **A molecular-scale portrait of domain imaging in organic surfaces.**
  Pérez-Rodríguez, Ana; Fernández, Antón; Gnecco, Enrico; Barrena, Esther and Ocal, Carmen, and Barrena, Esther
  Nanoscale **2017**, *9*, 5589-5596.

- **In situ Studies of Morphology Formation in Solution-Processed Polymer–Fullerene Blends**
  Barrena, Esther; Buss, Felix; **Pérez-Rodríguez, Ana**; Sanyal, Monamie; Schmidt-Hansberg, Benjamin; F.G. Klein, Michael; Scharger, Philip; Schabel, Wilhelm and Lemmer, Uli
  Elementary Processes in Organic Photovoltaics, Springer, Cham, **2017**, *4*, 1-24.

- **S-Shaped I-V Characteristics of Organic Solar Cells: Solving Mazhari's Lumped-Parameter Equivalent Circuit Model**
  Romero, Beatriz; Del Pozo, Gonzalo; Arredondo, Belén; MArtín-Martín, Diego; Ruiz Gordoa, María P; Pickering, Andrew; **Pérez-Rodríguez, Ana** and Barrena, Esther
  IEEE Transactions on Electron Devices 64 **2017**, *64*, 4622-4627

- **Spray-coated contacts from an organic charge transfer complex solution for organic field-effect transistors.**
  Georgakopoulos, Stamatis; **Pérez-Rodríguez, Ana**; Campos, Antonio; Temiño, Inés; Galindo, Sergi; Barrena, Esther; Ocal, Carmen and Mas-Torrent, Marta
  Organic Electronics **2017**, *48*, 365-370

- **Understanding the effect of solvent vapor annealing on solution-processed A–D–A oligothiophene bulk-heterojunction solar cells: the role of alkyl side chains.**
  Wessendorf, Cordula D; **Pérez-Rodríguez. Ana**, Hanisch. Jonas, Arndt. Andreas P, Ata. Ibrahim, Schulz. Gisela L, Quintilla. Aina, Bäuerl. Peter, Lemmer. Uli, Wochner. Peter, Ahlswede. Erik and Barrena. Esther
  Journal of Materials Chemistry A **2016**, *9*, 2571-2580.

- **Influence of the relative molecular orientation on interfacial charge-transfer excitons at donor/acceptor nanoscale heterojunctions.**
  Aghamohammadi, Mahdieh; Fernandez, Anton; Schmidt, Malte; **Pérez-Rodríguez, Ana**; Goñi, Alejandro Rodolfo; Fraxedas, Jordi; Sauthier, Guillaume; Paradinas, Markos; Ocal, Carmen and Barrena, Esther
  Organic Electronics **2014**, *48*, 365-370